Medizinische Fakultät
der
Universität Duisburg-Essen

Aus der Klinik für Strahlentherapie

Improvements to the dosimetry of $^{106}Ru/^{106}Rh$ ophthalmic plaques: Monte Carlo simulations and radiochromic film measurements

Inaugural-Dissertation
zur
Erlangung des Doktorgrades
der Naturwissenschaften in der Medizin
(Dr. rer. medic.)
durch die Medizinische Fakultät
der Universität Duisburg-Essen

Vorgelegt von
Marcelino Hermida López
aus Fene (Spanien)
2016

Dekan: Herr Univ.-Prof. Dr. med. J. Buer
1. Gutachter: Herr Priv.-Doz. Dr. L. Brualla Barberà
2. Gutachter: Herr Prof. Dr. A. M. Lallena Rojo, Granada
3. Gutachter: Herr Dr. J. Sempau Roma, Barcelona

Tag der mündlichen Prüfung: 20. Dezember 2016

Publications

Publications in scientific journals related to this thesis:

- **Hermida-López, M.** (2013): Calculation of dose distributions for 12 ^{106}Ru/^{106}Rh ophthalmic applicator models with the PENELOPE Monte Carlo code. Med. Phys. 40, 101705–1–13.

- **Hermida-López, M.**, Lüdemann, L., Flühs, A., and Brualla, L. (2014): Technical Note: Influence of the phantom material on the absorbed–dose energy dependence of the EBT3 radiochromic film for photons in the energy range 3 keV–18 MeV. Med. Phys. 41, 112103–1–6.

Presentations in scientific meetings related to this thesis:

- **Hermida-López, M.**, Lüdemann, L., Sauerwein, W., Brualla, L. (2014): Influence of the phantom material on the absorbed-dose energy dependence of the EBT3 radiochromic film for photons in the energy range 10 keV–18 MeV. Oral presentation. Published in Strahlenther. Onkol. Suppl 1, 1–164.

- Cano-Herranz, A., Delgado-Soler, C., Anducas-Santiago, N., and **Hermida-López, M.** (2014): EP-1544: Dose distributions for CCX, CCA and CIA applicators. Plaque Simulator vs. PENELOPE Monte Carlo code. Poster. Published in Radiother. Oncol. 111, S181.

Publications and posters during the thesis preparation, but not related to the thesis:

- Maidana, N.L., Vanin, V.R., García-Alvarez, J.A., **Hermida-López, M.**, Brualla, L. (2016): Experimental HPGe coaxial detector response and efficiency compared to Monte Carlo simulations. Appl. Radiat. Isot. 108 64–74.

- **Hermida-López, M.**, Sempau, J., Sauerwein, W., Brualla, L. (2016): Full Monte Carlo simulation compared to a simple source model for a dual–energy electron linear accelerator. Poster. Published in Strahlenther. Onkol. 192 106–107.

Contents

Chapter 1

Introduction

1.1 Background

Eye cancer is an uncommon disease. Despite its low incidence, ocular tumors can be life–threatening in many cases. Even when the treatment is effective, people living with eye cancer may suffer from severe side effects that deteriorate their quality of life (Nathan et al., 2015). The most frequent ocular tumors are uveal melanoma and retinoblastoma. Depending on the type and extension of the disease several treatment options are available. For small–to–medium melanomas and retinoblastomas, brachytherapy with radioactive ^{106}Ru/^{106}Rh plaques offers good outcomes in terms of local control and disease–free survival (Schueler et al., 2006; Abouzeid et al., 2008; Verschueren et al., 2010; Takiar et al., 2014, 2015; The American Brachytherapy Society – Ophthalmic Oncology Task Force, 2014).

In ophthalmic brachytherapy, like in other radiotherapy modalities, the accuracy of the radiation dose calculation and delivery may greatly influence patient outcomes. (Nath et al., 2016). Today, the most used radioisotopes for ophthalmic brachytherapy are ^{106}Ru/^{106}Rh and ^{125}I. The present work is focused on the dosimetry of the ^{106}Ru/^{106}Rh plaques. Although these plaques have been used for decades, the measurement and calculation of the produced dose distributions remain challenging tasks (ICRU, 2004). This fact may explain inconsistencies found in the literature on calculation and measurement of dose distributions from these plaques.

This thesis aims to improve the current knowledge on the features of the absorbed dose distributions produced by ^{106}Ru/^{106}Rh plaques. First, we will use Monte Carlo simulation of radiation transport, which is considered the *gold standard* method in radiation transport calculations, to estimate accurate absorbed dose to water distributions produced by the plaques. Secondly, we will develop a practical experimental technique to measure in water the planar dose distributions produced by these plaques. For this experimental validation the EBT3 radiochromic film model will be used which, in turn, requires to characterize this new film model by Monte Carlo simulation. Both the simulated and measured dose distributions will be compared with the available literature.

1.2 Objectives

This thesis aims to improve the knowledge on the dosimetry of ^{106}Ru/^{106}Rh ophthalmic plaques. To this purpose, the following objectives are defined:

1. To estimate accurate absorbed dose distributions in water for twelve models of ^{106}Ru/^{106}Rh plaques through Monte Carlo simulations with the PENELOPE code.

2. To study the energy dependence of the EBT3 radiochromic film with different phantom materials through Monte Carlo simulations with the PENELOPE code.

3. To develop a practical experimental method for measuring the absorbed dose distributions in water produced by ^{106}Ru/^{106}Rh plaques using the EBT3 radiochromic film to obtain two–dimensional (2D) dose distributions at several planes of interest.

1.3 Ocular tumors

To better understand ocular tumors and the treatment techniques available a brief description of the eye anatomy follows (Figure 1.1). The eye is approximately spherical in shape and it is enclosed by three layers of tissue (Galloway et al., 2006). The outer layer is the *sclera*, with a thickness of 0.3 to 1.0 mm, and formed by a white fibrous tissue that covers the eye except at the front part where is located the *cornea*, a transparent tissue that allows the light to enter the eye. The middle layer, the *uvea*, is formed by three connected structures: the *iris*, the *ciliary body* and the *choroid*. The iris is located at the anterior part of the uveal tract. It is the component that gives color to the eye. Its two sets of muscles allow varying the size of the *pupil*, the opening in its center that controls the passing of light. The ciliary body is a ring of muscle surrounding the *lens*, that may adjust the refractive properties of the lens. The choroid is composed of a capillary bed that supplies blood to the *retina*, which is the innermost layer, and the only one that contains neurons sensitive to the light. Specialized neurons on the retina named *photoreceptors* transform the light into electrical signals, which are driven through a neuron chain to the *optic disk*, a circular region that connects the retina and the *optic nerve* which ultimately sends the visual information to the brain. When the light enters the eye through the cornea, it traverses the lens and two chambers filled with fluid before arriving to the retina. The *anterior chamber*, between the cornea and the lens, is filled with *aqueous humor*, which is mostly (98%) water. The volume between the lens and the retina contains the *vitreous humor*, a gelatinous substance formed by a network of collagen fibers with large quantities of water in the interspaces (about 98-99% of the volume is water). The eye globe is covered by an external layer of tissue named *conjunctiva* that participates in eye lubrication. The diameter of the eye at birth is about 16–17 mm and at an age of 13 years old gets its final diameter of about 24 mm[1]. As the composition of the structures that account for more than 80% of the volume of the eye (the aqueous and the vitreous humors) is mostly water, it is reasonable to

[1] That diameter corresponds to an emmetropic eye, that is, a normal eye with perfect vision.

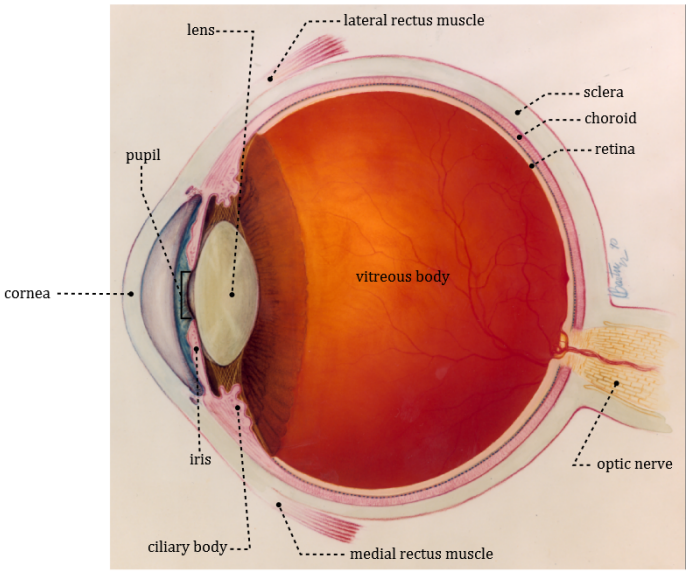

FIGURE 1.1: Anatomy of a normal human eye. Adapted from an image published by the National Eye Institute, National Institutes of Health, under a Creative Commons 4.0 license (`http://creativecommons.org/licenses/by/4.0/`).

model the eye as a water sphere for the purpose of Monte Carlo simulations and dosimetric measurements.

The most frequent malignant intraocular tumors are *uveal melanoma* and *retinoblastoma*, accounting for about 95% of the cases (uveal melanoma 75%, retinoblastoma 20%).

Uveal melanoma is a rare malignancy with a mean incidence of less than one new case per 100 000 inhabitants and year. It may arise from any component of the uvea, although the most common is the choroidal melanoma, with more than 90% of the cases. Most of the choroidal melanomas grow towards the inner part of the eye, producing dome-shaped tumors. Size of tumors is usually indicated by giving the *basal diameter*, that is, the approximate diameter of the tumor base, and the *apical height*, that is, the distance from the base of the tumor to the tumor *apex*, the highest part of the tumor. Choroidal melanomas progress by developing distant metastases being the liver the most common site. From detection of metastases the median survival is 2–12 months with a survival probability of 10%–15% after one year (Nathan et al., 2015). Hence, the treatment of uveal melanoma aims primarily to avoid metastatic spread and to conserve useful vision in the affected eye, if possible. The optimum therapeutic choice depends on the location and size of the melanoma (Damato, 2012). For large tumors (basal diameter greater than 15 mm and apical height above 10 mm) or when other therapies fail, the preferred option is proton therapy or enucleation. The latter was the classic treatment for choroidal melanomas for many years. Plaque brachytherapy with ^{125}I or ^{106}Ru/^{106}Rh is indicated for small– to medium–sized posterior uveal melanomas, that is, with basal diameters less than 15 mm and heights below 10 mm. Another therapeutic option

for medium and large tumors is external beam radiotherapy with photons using stereotactic techniques. Other techniques not involving ionizing radiation are laser photocoagulation and transpupillary thermotherapy, reserved to treat small and shallow tumors located away from critical structures such as the fovea. Surgical alternatives other than enucleation include endoresection and sclerouvectomy. Chemotherapy is only indicated as a palliative treatment for metastatic disease.

Retinoblastoma is the most common intraocular tumor in children, with an incidence of about one case per 15 000 live births. It is a congenital disease affecting the retina and, in rare cases, the pineal gland (trilateral retinoblastoma). Approximately 25% of the retinoblastomas are bilateral. A variety of treatment techniques are available depending on the degree of spread of the disease (Olch, 2013). For small localized lesions, focal therapies such as transpupillary thermotherapy, cryotherapy and laser photocoagulation, alone or in combination with chemotherapy, may be used. For tumors thicker than 4 mm, with limited vitreous seeding, or not responding to focal therapies, ophthalmic brachytherapy with ^{125}I or ^{106}Ru/^{106}Rh is an option. When large vitreous seeding is present, or in case of failure of primary treatments, irradiation of the whole eye globe with external beam radiotherapy, or even enucleation, may be necessary.

1.4 Ophthalmic brachytherapy

Ophthalmic brachytherapy allows to deliver a high radiation dose to intraocular tumors while sparing critical structures within the eye. It is less invasive than surgical resection, and produces less damage to tissues surrounding the tumor than external beam radiotherapy (Damato, 2012). Today, the most used radioisotopes for ophthalmic brachytherapy are ^{125}I and ^{106}Ru/^{106}Rh. The present work is devoted to improve the dosimetry of ^{106}Ru/^{106}Rh plaques, which were first introduced by Lommatzsch in 1964 to treat choroidal and ciliary body melanomas. In a retrospective study Lommatzsch et al. (2000) presented the results of long–term follow–up of patients with small– and medium–sized posterior uveal melanomas, with follow–up times of at least 22 years, the longest period reported in the literature. They concluded that after 15 years the local control rate was of 63.8% and the cumulative survival rate of 66.7%. The study by Damato et al. (2005) on small–to–medium choroidal melanomas reported an excellent local control in 93% to 98% of the patients after 5 years. A more recent study by Verschueren et al. (2010), with 425 patients, found a 5–year actuarial local control of 96% with a 5–year metastases–free survival of 76.5%. About one third of the patients were free of radiation complications after 5 years, and the enucleation rate at 5 years was only of 4.4%. The treatment allowed cosmetic preservation in 96% of the cases, but functional preservation in only one half of the patients.

Although ^{106}Ru/^{106}Rh plaques are popular in Europe, in the United States ^{125}I has been traditionally the radioisotope of choice, based on the results of the Collaborative Ocular Melanoma Study (COMS) (The Collaborative Ocular Melanoma Study Group, 2006; Miras et al.,

2013). The COMS was a 12–year study that demonstrated the relative equivalence of ^{125}I therapy compared with enucleation to avoid metastatic spread for patients with medium–sized choroidal melanoma. An unwanted consequence was to establish ^{125}I as the *de facto* standard for ophthalmic brachytherapy in North America (The American Brachytherapy Society – Ophthalmic Oncology Task Force, 2014). However, in 2014 a research group from the MD Anderson Cancer Center published two papers on the largest cohort of patients treated in the United States with ^{106}Ru/^{106}Rh plaques for uveal melanoma with excellent outcomes. They reported actuarial 5-year rates of local control, progression–free survival and overall survival of 97%, 94% and 92%, respectively (Takiar et al., 2014). In a retrospective study comparing these results with patients treated with ^{125}I, they found that for ^{125}I these values were 83%, 65%, and 80% (Takiar et al., 2015). The patients treated with ^{106}Ru/^{106}Rh also experienced less retinopathy and cataracts. They concluded that these results justify the reintroduction of ^{106}Ru/^{106}Rh plaques into the clinical practice in the United States for uveal melanoma, specially for those with apical heights less than 5 mm.

Two large patient cohort studies exist on ^{106}Ru/^{106}Rh therapy for retinoblastoma. The study by Schueler et al. (2006) from the Universitätsklinikum Essen included 134 patients (140 eyes). They reported 5–year local control and eye preservation rates of 94% and 87%, respectively, with 5–year overall survival rate of 96.4%. The doses given to the tumor apex were in the range of 88 to 138 Gy. In the high–dose region the rate of late effects was relatively high, with 54% of cataract incidence, and up to 20% of retinopathy and optic neuropathy. Abouzeid et al. (2008) studied 39 patients (41 eyes) with lower doses than in the study from Essen, about 55 Gy. They reported fewer late effects but their outcomes were worse, with 1–year local control and eye preservation rates of 73% and 76%, respectively.

1.5 Characteristics of ^{106}Ru/^{106}Rh plaques

At present, ^{106}Ru/^{106}Rh plaques for ophthalmic brachytherapy are produced by only one manufacturer (Eckert & Ziegler BEBIG, GmbH. Berlin, Germany), which supplies together with the plaques a calibration certificate traceable to the NIST (National Institute of Standards and Technology, Gaithersburg, MD, USA) since 2002. The calibrated absolute absorbed dose rate to water is stated at a distance of 2 mm from the surface of the plaque, along its central axis. The certificate also includes depth–dose values measured along the central axis of the plaque. Measurements are conducted with a plastic scintillator, and the relative uncertainty in absorbed dose values is stated to be of 20% ($k = 2$), which includes the 15% uncertainty ($k = 2$) of the NIST measurements.

1.5.1 Description and geometry

Figure 1.2 shows the geometrical description of the available ^{106}Ru/^{106}Rh ophthalmic plaques, with the intended clinical indications. The basic shape of these plaques is a part of a spherical

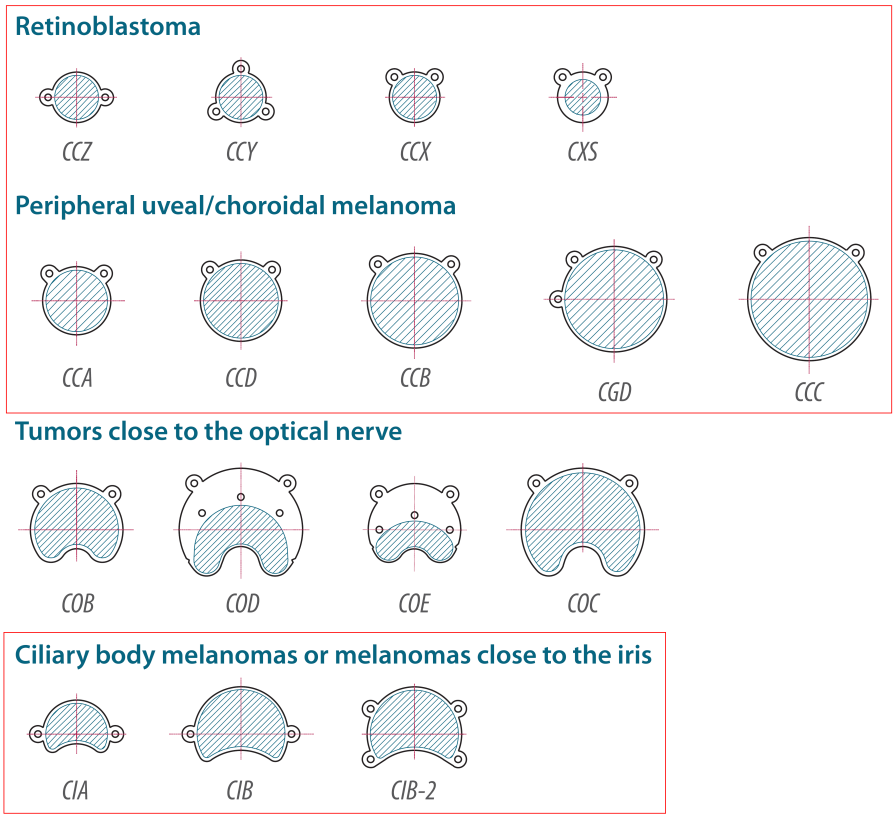

FIGURE 1.2: Geometrical description of the available ^{106}Ru/^{106}Rh opthalmic plaques with the intended clinical indications. The radioactive area is marked hatched. The plaques studied in this thesis are inside red frames. Courtesy of Eckert & Ziegler BEBIG, GmbH. Berlin, Germany.

shell. Depending on the model, the radius of curvature ranges from 12 to 14 mm, and the external diameter of the circle that limits the spherical cap ranges from 10 to 25 mm (ICRU, 2004). The plaques exhibit rounded edges and eyelets at selected locations such that the plaques can be sutured to the sclera. The CIA and CIB/CIB–2 models have a cut–out to treat anterior tumors, affecting the ciliary body or the iris, thus preventing irradiation of the cornea. Other models (COB, COD, COE and COC), not studied in this thesis, have a deeper cut–out to allow treatment of tumors close to the optic nerve.

A thin layer (∼0.1 μm thick) of the radioisotope is electrolytically deposited on the concave surface of a 0.2 mm–thick layer of high–purity silver. This layer is encapsulated between the concave surface of a 0.7 mm–thick layer of silver and the convex surface of a 0.1 mm–thick layer of silver (exit window) (ICRU, 2004; Astrahan, 2003).

1.5.2 Spectrum of ^{106}Ru/^{106}Rh beta decay

Both ^{106}Ru and ^{106}Rh are pure β^- emitting radioisotopes. The beta particles emitted, averaged over many disintegrations, have a continuous energy spectrum (Figure 1.3). The Fermi theory of beta decay leads to relatively simple expressions for the shape of the beta spectrum.

^{106}Ru and ^{106}Rh are in secular equilibrium (ICRU, 2004): the ^{106}Ru parent (half–life of 373.6 d) decays via β^- to ^{106}Rh (Q–value = 39.4 ± 0.2 keV). The ^{106}Rh daughter (half–life of 29.8 s) disintegrates via β^- to ^{106}Pd (Q–value = 3545.6 ± 5.3 keV). Figure 1.4 shows the decay schemes of ^{106}Ru and ^{106}Rh. Although there is a gamma component produced by the transitions to the ground state of ^{106}Pd, and some minor contributions resulting from Auger emission and electron capture processes (Defrenne and Negret, 2008), the main contributor to the therapeutic dose is the beta spectrum emitted by ^{106}Rh.

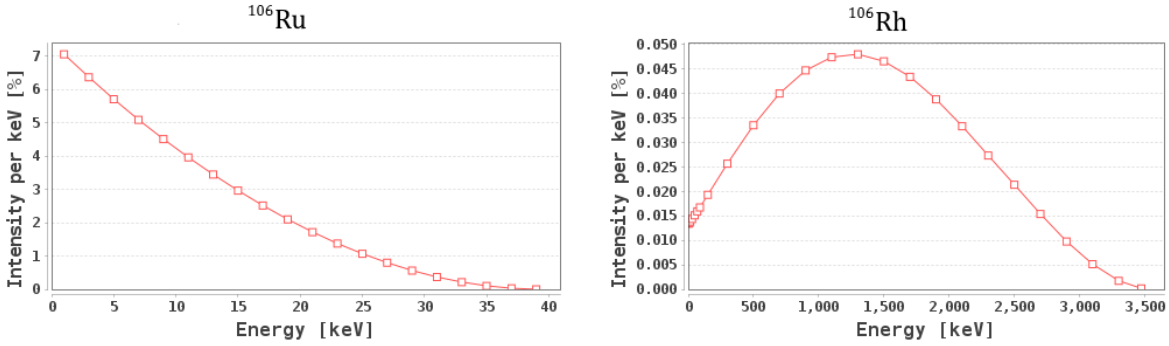

FIGURE 1.3: Beta spectra of ^{106}Ru and ^{106}Rh. Plots taken from the IAEA Live Chart of Nuclides (https://www-nds.iaea.org/). Reproduced with permission.

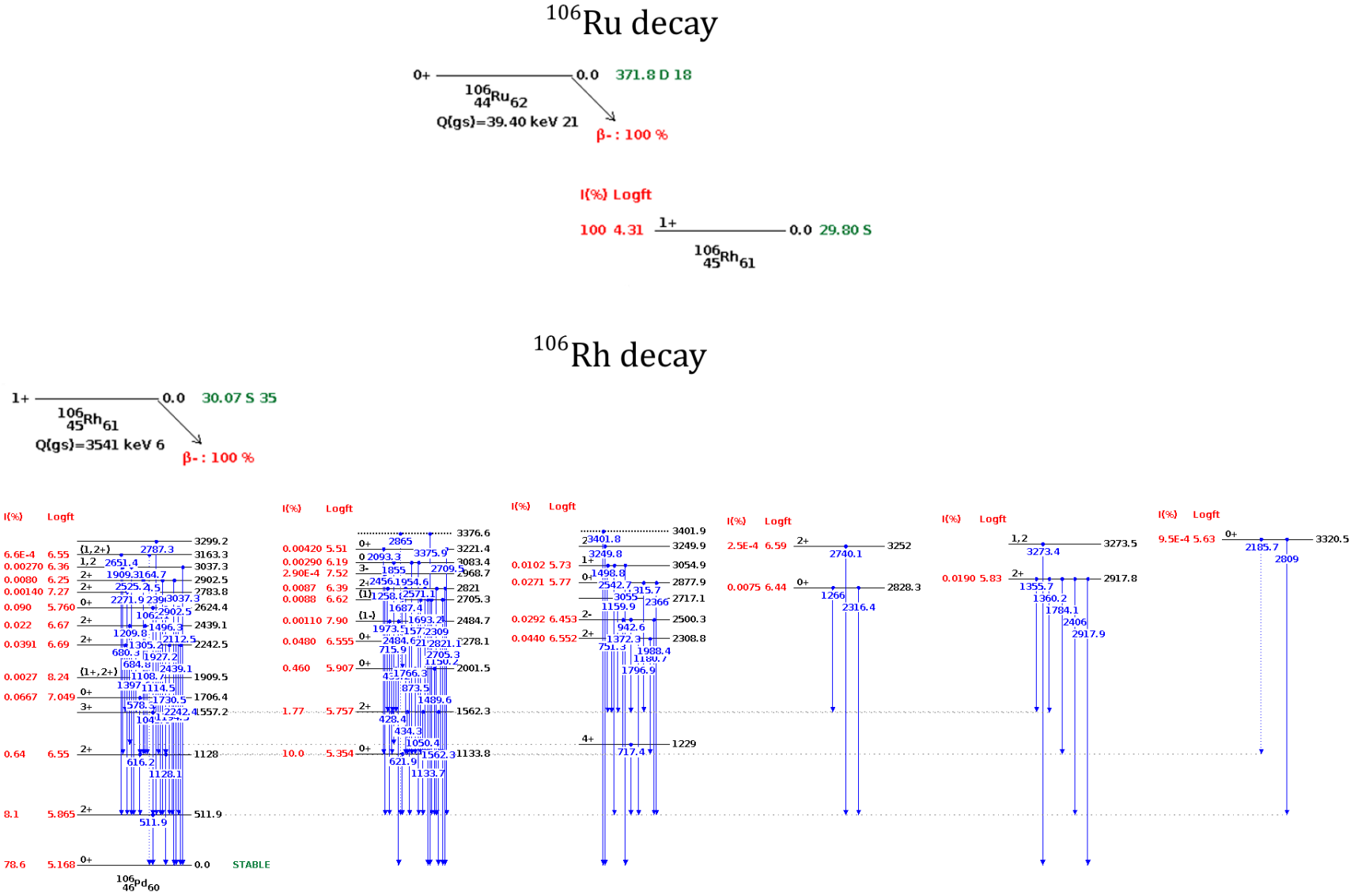

FIGURE 1.4: Decay schemes for ^{106}Ru and ^{106}Rh, pure β^- emitters in secular equilibrium. ^{106}Ru decays to the ground state of ^{106}Rh, that decays with a certain probability to excited states of ^{106}Pd, which in turn deexcite resulting in a complex gamma spectrum. The Q–values for ^{106}Ru and ^{106}Rh decays are 39.4 ± 0.2 keV and 3545.6 ± 5.3 keV, respectively. Plots taken from the IAEA Live Chart of Nuclides (`https://www-nds.iaea.org/`), based on data from Defrenne and Negret (2008). Reproduced with permission.

1.6 Treatment planning with ^{106}Ru/^{106}Rh plaques

In radiotherapy the term *treatment planning* refers to the process in which a radiation treatment technique is selected and customized for a specific patient. In the case of ophthalmic brachytherapy with ^{106}Ru/^{106}Rh plaques the treatment planning process involves determining the location and size of the tumor to be treated, the dose prescription according to the type and characteristics of the tumor, the choice of an adequate plaque to cover the tumor with the prescribed dose, the dosimetric study to obtain the dose distribution inside the eye and the calculation of the treatment time to deliver the prescribed dose. This process is a teamwork among ophthalmologists, radiation oncologists, medical physicists and other staff.

A computerized treatment planning system is recommended to assist in the planning, calculation and dose assessment in ophthalmic brachytherapy (Nag et al., 2003). At present, the state–of–the–art in treatment planning with ^{106}Ru/^{106}Rh plaques is the Plaque Simulator software (Eye Physics, LLC, Los Alamitos, CA, USA) distributed by the manufacturer of the plaques. It is a three–dimensional (3D) treatment simulation system initially developed by Astrahan et al. (1990) for the treatment planning of ocular tumors with ^{125}I seeds. In 2003 Astrahan adapted the software to implement a patch–source model to handle ^{106}Ru/^{106}Rh plaque calculations (Astrahan, 2003). This method consists of dividing the active layer into hundreds of patches approximated as small disks uniformly distributed to cover the active layer of the plaque. The source strength of each patch is adjusted in an iterative process that uses as input the measured activity of the plaque and the depth–dose distribution stated in the calibration certificate of the plaques. From version 6.0.1, released in 2014, the software can use the dose rate measurements at 1 mm from the surface stated in the calibration certificate by the manufacturer, to take into account the detailed radioisotope distribution of particular plaques. The software models the eye as composed entirely of water.

To achieve a therapeutic effect, the plaque must be positioned on the sclera covering the tumor with an adequate safety margin, ideally 2–3 mm. To access the sclera, first the conjunctiva is excised, detaching temporarily ocular muscles if necessary to rotate the eye to visualize the tumor. Transpupillary illumination may be used to localize and mark the tumor base on the sclera. When a placement is decided the plaque is positioned and sutured to the sclera through the plaque eyelets. Then the conjunctiva is repositioned and the eye is rotated again to the normal position. After the treatment is completed, which takes usually between 1 and 10 days, the plaque is surgically removed.

1.7 Measurement and calculation of absorbed dose distributions produced by ^{106}Ru/^{106}Rh plaques

Several detectors have been used to measure the dose distributions of ^{106}Ru/^{106}Rh plaques, including diodes (Soares et al., 2001), diamond detectors (Soares et al., 2001), extrapolation chambers (Davelaar et al., 1992; Soares et al., 2001), small volume ionization chambers (Soares

et al., 2001), polymer gel (Chan et al., 2001), thermoluminescent dosimeters (TLD) (Soares et al., 2001; Kovačević et al., 2005; Barbosa et al., 2015), alanine detectors (Soares et al., 2001), radiochromic films (Taccini et al., 1997; Soares et al., 2001; Kirov et al., 2005; Heilemann et al., 2015), and plastic (Soares et al., 2001; Kaulich et al., 2005; Flühs et al., 2016) and liquid (Kirov et al., 2005) scintillators. A good description of the advantages and disadvantages of these detectors for beta dosimetry is provided in the ICRU Report 72 (ICRU, 2004), which was partially based on a paper by Soares et al. (2001), a key reference on measurement methods for beta ophthalmic plaques. These authors compared dose data measured with different detectors and by different institutions. They concluded that at that time the measurement uncertainty for ^{106}Ru/^{106}Rh ophthalmic plaques was approximately from 10% to 15%. Clearly, the accuracy of ophthalmic plaque dosimetry had to be improved.

Because it is difficult to accurately measure dose distributions from ^{106}Ru/^{106}Rh plaques, it is mandatory to compare the measured data with calculations (ICRU, 2004). The simplest method for calculating the dose distributions of ^{106}Ru/^{106}Rh ophthalmic plaques is based on beta–ray point–source kernel integration (Hokkanen et al., 1997). Such calculations are easy to perform and accurate in a homogeneous medium, but the method fails in the presence of heterogeneities such as those related to different tissues and the plaque itself (ICRU, 2004). To partly overcome the limitations of point–source kernel integration, Astrahan (2003) developed the patch–source model that is currently implemented in the Plaque Simulator software.

The most accurate method for estimating absorbed dose distributions from ^{106}Ru/^{106}Rh plaques is the Monte Carlo simulation of radiation transport. The Monte Carlo method can address complex geometrical setups with arbitrary materials, and the obtained results are often as accurate as, or better than, measured values (ICRU, 2004). A combined point–kernel and Monte Carlo computer model was used by Davelaar et al. (1992) to estimate the depth–dose–to–water distributions for CCA and CCB plaque models. The estimated depth–dose was approximately 15% lower than the manufacturer's quoted value.

Sánchez-Reyes et al. (1998) were the first authors to apply a well established general–purpose Monte Carlo code to estimate dose distributions from ^{106}Ru/^{106}Rh plaques. Unfortunately, their study design suffered from some substantial flaws, invalidating their results, as noted by Brualla et al. (2012).

Cross et al. (2001) presented dose distributions estimated with different Monte Carlo codes for a non–clinical planar plaque and for a CCB plaque, which are the same plaques examined by Soares et al. (2001). Poor consistency was observed among the available simulation results. The authors proposed that differences in the modeling of the plaques, rather than the differences inherent to the Monte Carlo codes, might explain the observed discrepancies. They concluded that further calculations would be necessary to clarify the situation.

Mourtada (2005) performed a comparative dosimetric analysis of ^{106}Ru/^{106}Rh ophthalmic brachytherapy and external beam proton therapy. The relative dose distributions for both treatment modalities were estimated in a model eye using the MCNPX Monte Carlo code for

the CCB plaque, yielding contradictory results: the MCNPX simulation results were consistent with the results obtained by Cross et al. (2001) using MCNP4B and by Taccini et al. (1997) using GEANT3, whereas the differences found by Cross et al. (2001) between MCNP4B and ACCEPT 3.0 were similar to those found by Soares et al. (2001) among MCNPX, ACCEPT 3.0, and film measurement data.

Fuss et al. (2011) simulated the dose distributions produced by a CCX plaque using the LEPTS Monte Carlo code.

Finally, Brualla et al. (2013) employed the general–purpose Monte Carlo code PENELOPE to obtain accurate dose distributions for CCA and CCB plaques in a voxelized eye phantom based on computed tomography scan data. In addition to presenting dose profile data, these authors estimated the doses to contoured anatomical structures inside the eye.

1.8 Radiochromic films

The selected detector to study in this thesis is the radiochromic film, as it is the only available detector capable of measuring 2D dose distributions produced by ^{106}Ru/^{106}Rh plaques in a single measurement. Radiochromic films were introduced in the early 1990s by International Specialty Products (Wayne, NJ, USA)[2] and supposed a major change respect to the radiographic films previously used for radiation dosimetry. These new films are relatively insensitive to visible light and they suffer a color change by polymerization reactions in response to irradiation avoiding the need of a chemical development process. Radiochromic films are nowadays routinely used for radiation dosimetry in external beam radiotherapy and brachytherapy applications (Devic, 2011) such as verification of treatment plans, quality assurance of clinical linear accelerators and radioactive sources, and *in–vivo* dosimetry. Several types of radiochromic films were developed, with important differences in the composition of the active layers (Blackwell et al., 1998), including models aimed for radiotherapy applications, namely, the EBT[3], EBT2 and EBT3. The EBT and EBT2 models are now outdated since the EBT3 model was introduced in 2012.

In principle, the characteristics of radiochromic films make them an almost–ideal detector for beta dosimetry: high spatial resolution, self–developing, near tissue equivalent, a very thin detection layer and relatively low energy dependence (Devic, 2011). However, few publications report data from measurements of ^{106}Ru/^{106}Rh plaques with radiochromic films (Taccini et al., 1997; Soares et al., 2001; Kirov et al., 2005; Heilemann et al., 2015). The first publications found as a major limitation the large variations in the thickness of the active[4] layer present in the early film models (Taccini et al., 1997; Soares et al., 2001). Soares et al. (2001) reported a measurement relative standard uncertainty of 7.5% for measurements at a plane perpendicular to the symmetry axis of the plaques, and using a phantom made of WT1 plastic water material.

[2] Now incorporated to Ashland Specialty Ingredients, Wayne, NJ, USA.
[3] EBT stands for External Beam Therapy.
[4] That is, the layer with the emulsion sensitive to radiation.

The 'second generation' of radiochromic films (MD–55–2 and HD–810 models) were used by Kirov et al. (2005) to measure dose distributions of a CCX plaque in a plastic phantom, stating a relative standard uncertainty of 15%.

The initial problems with thickness variations were partially solved with the EBT2 model, by adding a yellow dye to the active layer which allowed to compensate for non–uniformities in the active layer thickness. The most recent EBT3 model also introduced changes to the active layer composition to improve the energy dependence in a wide energy range. As this is the film model used in this thesis, we considered relevant to confirm the supposed improvement in energy dependence, and to study the influence of different phantom materials in the energy dependence of the EBT3 model. These topics will be addressed in chapter 3.

1.9 The Monte Carlo method for radiation transport

The term *radiation transport* refers to the physical phenomenon consisting in the propagation of radiation (directly or indirectly ionizing) through matter. In this process, radiation with a certain energy propagates in a material medium, interacting with it and transferring energy to the medium and to secondary particles. The quantity that represents the probability of occurrence of a given interaction between radiation and matter is named the *cross section* for the interaction of interest. Although the physical principles that govern the individual interactions between radiation and matter are well known, when a high number of particles or non–trivial geometries are considered, the mathematical complexity of the problem is too high to be solved by analytical methods without introducing approximations or simplifications.

The *Monte Carlo method* is a stochastic technique based on the use of (pseudo–)random numbers, capable of simulating mathematical or physical experiments (Kalos and Whitlock, 2008). A basic application of the Monte Carlo method is numerical integration. The method has been successfully applied to a wide range of disciplines, including physics, engineering, finance, etc. In particular, the method is well suited to the simulation of the interactions of radiation with matter.

The Monte Carlo simulation of radiation transport is a simple process (see e.g. Rodríguez Castillo (2015)): (i) A primary particle is generated by specifying its initial state variables (type of particle, position, flight direction, and kinetic energy). (ii) The particle is moved to a new position along a straight line following the flight direction. The length of flight is obtained by sampling the corresponding path length probability density function characteristic of the particle and the medium. (iii) The particle suffers an interaction, which is randomly selected according to the probabilities given by the cross sections of the possible interactions considered in the simulation. (iv) The interaction is simulated, which results in a change in the state variables of the primary particle and possibly in the generation of secondary particles. At this step, the relevant quantities for the simulation are *tallied* (e.g. the energy deposited in a detector). (v) The process from step (ii) is repeated, until the initial particle is absorbed or escapes

from the geometry simulated (a particle is considered locally absorbed when its kinetic energy falls below a specified energy threshold). Secondary particles are simulated in the same way. The simulation of a primary particle and all their descendants is named a *history* or a *shower*. By simulating a large number of histories, average values of macroscopic observables of interest such as the energy deposition, can be estimated. Owing to the random nature of the Monte Carlo simulation the tallied observables have an inherent statistical uncertainty.

Although the simulation algorithm is conceptually simple, if the number of interactions per unit path length is high, as it is the case for electrons, the simulation could become extremely slow. Different simulation schemes are used to handle this situation. In a *detailed simulation* all the interactions suffered by a particle are simulated one by one. This scheme is adequate to simulate photons, as the number of interactions per unit length is low. Electrons, however, may suffer thousands of interactions, and most of them are elastic, that is, the kinetic energy of the electron is conserved and its direction of movement changes only slightly. In others, the energy loss is only of a few tens of electron–volts. In most cases, it results very inefficient to simulate all these *soft* events one by one[5]. Most of the Monte Carlo codes for the simulation of radiation transport rely on the so–called *condensed transport schemes*, which use multiple–scattering theories that simulate in an approximate way the global effect of a large number of events occurring in a track segment of a given length. Each track is approximately simulated as a series of steps of a specified length much larger than the mean free path length of the real collisions (Fernández-Varea et al., 1993). Depending on how the value of this step length is determined, the condensed transport algorithms are classified in two classes, following the terminology coined by Berger (1963):

- Class I algorithms: a fixed step length is used. This approach fails close to the interface between different materials, as the step length may not be contained in a single medium, which is a necessary condition to apply multiple–scattering theories.
- Class II algorithms: the step length is randomly selected. The interactions are classified as *soft* events if the energy loss and the changes in direction are below predefined cutoffs. The rest of the interactions are classified as *hard* events and are simulated in a detailed way. The choice of the energy and angular cutoff values is usually responsibility of the user, and not a characteristic of the physical processes involved.

The purpose of a simulation is the estimation of the expected values of some quantities of interest. Any quantity of interest Q (e.g., the energy deposited in a detector), is estimated as the arithmetic mean of the tallied values from a large number N of independently simulated histories:

$$\overline{Q} = \frac{1}{N}\sum_{i=1}^{N} q_i, \tag{1.1}$$

where q_i is the tallied contribution of the i–th history to the quantity Q, that is, the contribution of all the particles pertaining to the i–th history. If the number of simulated histories N is

[5] Some exceptions are simulations of low energy electrons, or geometries involving thin foils.

sufficiently large, this mean converges to the expected value $\langle Q \rangle$. The standard statistical uncertainty inherent to the Monte Carlo estimate for the quantity Q is given by:

$$\sigma_Q = \sqrt{\frac{1}{N}\left[\frac{1}{N}\sum_{i=1}^{N} q_i^2 - \overline{Q}^2\right]}. \tag{1.2}$$

At present, there is a variety of general–purpose Monte Carlo codes (software packages) for the simulation of radiation transport, such as EGSnrc (Kawrakow et al., 2009), Geant 4 (Agostinelli et al., 2003), MCNP (Forster et al., 2004) and PENELOPE (Baró et al., 1995; Sempau et al., 1997; Salvat et al., 2009; Salvat, 2015a), which have been successfully applied to a wide range of fields, including medical physics.

The simulations computed for this thesis were performed with PENELOPE[6] (Baró et al., 1995; Sempau et al., 1997; Salvat et al., 2009; Salvat, 2015a), a Monte Carlo code written in Fortran that simulates the coupled transport of electrons, positrons and photons with energies ranging from 50 eV to 1 GeV in materials consisting of homogeneous bodies with arbitrary chemical compositions. For photons, PENELOPE performs detailed simulation. Electrons and positrons are simulated using a mixed class II scheme. Collision events are classified as hard or soft according to the energy loss and the change in the particle direction relative to certain user–defined threshold values. The algorithm is controlled by eight parameters: EABS (for photons, electrons and positrons), C1, C2, WCC, WCR and DMAX. EABS are the absorption energies defined for photons, electrons and positrons. If the energy of a particle becomes smaller than the corresponding absorption energy the particle is assumed to be locally absorbed. The rest of the parameters only apply to the simulation of electrons and positrons. C1 is the average angular deflection due to a hard elastic collision and all previous soft collisions. C2 controls the maximum allowed value for the average fractional energy loss in a step. WCC and WCR are energy cutoffs for hard inelastic collisions and hard Bremsstrahlung emission, respectively. If the user sets C1 = C2 = WCC = 0 and WCR with an arbitrary negative value, PENELOPE performs a detailed simulation for electrons and positrons (Salvat, 2015a). Finally, DSMAX is an upper limit for the step length. The values given to these parameters determine the accuracy and speed of the simulation. The user must set the values of the simulation parameters for each material of the geometry considered in the simulation. PENELOPE models the system geometry with bodies limited by constructive quadric surfaces. The geometry subroutines are enclosed in the geometry package PENGEOM (Almansa et al., 2016).

Since the first version of PENELOPE was released in 1996, many improvements have been added to the physics interaction models, to the tracking algorithm, and to the PENGEOM subroutines (Salvat, 2015b). PENELOPE has found many applications in the medical physics field, including radiation dosimetry (Sempau and Andreo, 2006; Erazo et al., 2014), radiotherapy (Seco and Verhaegen, 2013; Rodríguez et al., 2013), x–ray imaging (Badano and Sempau, 2006), and nuclear medicine (España et al., 2009). Comprehensive experimental benchmarks of the

[6] The acronym PENELOPE initially standed for PENetration and Energy LOss of Positrons and Electrons. Photons were introduced later.

reliability of the PENELOPE interaction models and tracking algorithms are available (Sempau et al., 2003; Faddegon et al., 2008, 2009), both for photons and electrons/positrons. The most recent version of the PENELOPE software package and the associated manual are freely available from the OECD Nuclear Energy Agency Data Bank (`http://www.nea.fr`) and from the Radiation Safety Information Computational Center (`http://www-rsicc.ornl.gov`).

1.10 Thesis outline

The thesis is structured in six chapters, being this introduction the chapter 1. The following chapters present the methods and results developed in the thesis to fulfill the objectives outlined at the beginning of this chapter.

Chapter 2 presents the results of Monte Carlo simulations for twelve ^{106}Ru/^{106}Rh plaque models using the PENELOPE code, which include the plaque models most commonly used in the clinical practice. These results are compared with the available published data, solving inconsistencies found among the published data. The obtained absorbed dose distributions represent the most comprehensive dataset available in the literature on Monte Carlo simulation of ^{106}Ru/^{106}Rh plaques for ophthalmic brachytherapy. For some of these plaques, the simulation results from this research are the first dose data reported. Most of the content of this chapter was published by the author of this thesis in the *Medical Physics* journal (Hermida-López, 2013, 2016). The chapter includes also unpublished data on the influence of the gamma component produced by the transitions to the ground state of ^{106}Pd on the simulation of ^{106}Ru/^{106}Rh plaques, which is neglected in all available published works. The numeric dose data presented may be useful for quality assurance of treatment planing systems, and may constitute the basis of a consensus dataset for ^{106}Ru/^{106}Rh plaques, such as the already existing for other brachytherapy sources.

Chapter 3 analyzes the energy dependence of the EBT3 radiochromic film through Monte Carlo simulations. It represents the first study on the influence of the phantom material on the energy dependence of the EBT3 film. Several solid phantom materials commonly used for film dosimetry are studied and compared to water, which is the reference medium for radiation dosimetry. The results from this chapter are needed to assess a component of the experimental uncertainty of the measurements presented in chapter 4. However, these results have a wider scope, as the EBT3 model is the current *de facto* standard for film dosimetry in radiotherapy and other fields. The contents of this chapter were published by the author of this thesis and coauthors in the *Medical Physics* journal (Hermida-López et al., 2014).

Chapter 4 presents the experimental validation of the simulation results through measurements of absorbed dose distributions of ^{106}Ru/^{106}Rh plaques with the EBT3 radiochromic film. Few publications report measurement data of ^{106}Ru/^{106}Rh plaques with radiochromic film, and all of them use plastic phantoms. In this chapter, two novel experimental setups are developed to measure absorbed dose distributions of ^{106}Ru/^{106}Rh plaques with the EBT3

film in water. These practical setups may ease the quality assurance procedures to the users of ^{106}Ru/^{106}Rh plaques.

In chapter 5 a discussion is presented, where the scope and limitations of the results from the thesis are analyzed. Moreover, it is discussed how the obtained results may influence the clinical practice of ^{106}Ru/^{106}Rh ophthalmic brachytherapy and future research lines are suggested.

Finally, chapter 6 briefly summarizes the thesis conclusions, and the major findings regarding the objectives outlined in chapter 1.

Chapter 2

Monte Carlo simulation of ^{106}Ru/^{106}Rh ophthalmic plaques

2.1 Introduction

Beta–ray emitting ^{106}Ru/^{106}Rh ophthalmic plaques are routinely used to treat ocular tumors, mainly choroidal melanomas and retinoblastoma, with good clinical outcomes (Schueler et al., 2006; Abouzeid et al., 2008; Verschueren et al., 2010; Takiar et al., 2014, 2015; The American Brachytherapy Society – Ophthalmic Oncology Task Force, 2014). Factors that are relevant to the clinical outcome include the tumor dose coverage and the dose to normal tissue inside the eye. Because the beta radiation used for therapeutic applications produces steep dose gradients, an accurate knowledge of the generated absorbed dose distributions is essential for treatment planning and clinical dose assessment (ICRU, 2004). Although ^{106}Ru/^{106}Rh plaques were introduced in 1964, the measurement and calculation of absorbed dose distributions remain challenging tasks today. Difficulties arise because of the small range of the emitted beta particles (only a few millimeters in water), the small volume irradiated, and the aforementioned steep dose gradients. The shape of the plaques (spherical shells) also produces experimental difficulties. The most accurate method to compute dose distributions produced by ^{106}Ru/^{106}Rh plaques is Monte Carlo simulation of radiation transport (ICRU, 2004).

Despite that there are 16 models of ^{106}Ru/^{106}Rh plaques commercially available, the majority of the published studies on Monte Carlo simulation of ^{106}Ru/^{106}Rh plaques have focused on the most commonly used models (CCA and CCB), and for some models, namely the CXS and the CCD, there are no published data. The work presented in this chapter aimed to accurately estimate the absorbed dose–to–water distributions of 12 clinical ^{106}Ru/^{106}Rh plaque models (CCA, CCB, CCC, CCD, CCX / CCY / CCZ, CXS, CGD, CIA and CIB/CIB2) using the Monte Carlo code PENELOPE. The results were compared with published data when available. The work presented in this chapter represents the most comprehensive study to date on Monte Carlo simulation of ^{106}Ru/^{106}Rh plaques. Most of the content was published in the *Medical Physics* journal by the author of this thesis (Hermida-López, 2013, 2016). Additionally, unpublished data on the influence of the ^{106}Pd gamma spectrum on the simulations of ^{106}Ru/^{106}Rh plaques are also presented in this chapter.

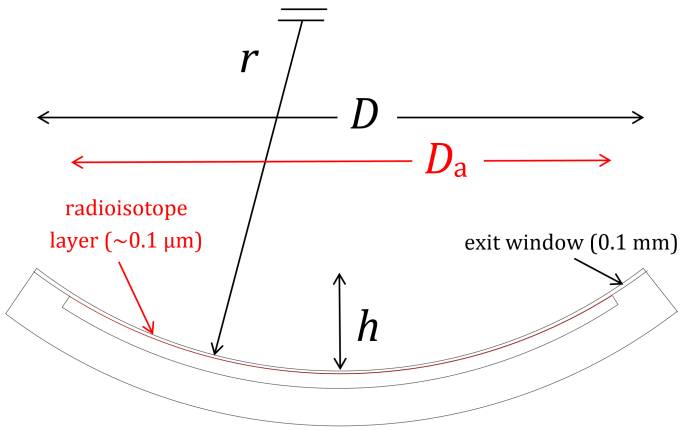

FIGURE 2.1: Cross section of a clinical ^{106}Ru/^{106}Rh plaque (not to scale for clarity), showing the diameter D, the active diameter D_a, the height h, and the radius of curvature r. The total thickness of the plaques is 1 mm.

2.2 Methods

2.2.1 Geometric modeling of the ^{106}Ru/^{106}Rh plaques

The geometric modeling of the plaques was based on data from the ICRU Report 72 (ICRU, 2004) and from the manufacturer's manual for the plaques[7]. Figure 2.1 shows a cross section of a typical ^{106}Ru/^{106}Rh plaque. Table 2.1 shows the geometrical dimensions of the plaques studied in this chapter. The thickness of the radioisotope layer on the plaques is ~0.1 μm (Astrahan, 2003) [in some publications, it is incorrectly stated that the thickness is 0.2 mm (Taccini et al., 1997)]. The radioisotope layer thickness in the simulations was considered negligible and the radioisotope was assumed to be homogeneously distributed over the active area. This is an approximation, as surface dose rate inhomogeneities of up to 20% respect to the value at the central axis have been described (Eichmann et al., 2009). The plaques were simulated as being immersed in a 6 cm–radius water sphere, concentric with the plaque.

In addition to the clinical ^{106}Ru/^{106}Rh plaques, a planar non–clinical plaque (CCB 570 model) (Soares et al., 2001; Cross et al., 2001) was also simulated. This plaque consists of a disk with an active diameter of 20.5 mm. The active layer is mounted on a silver backing with a 0.9 mm thickness and is covered by a silver exit window with a 0.1 mm thickness. A total diameter of 21 mm was assumed. The planar design of this plaque allows measuring the produced dose distribution easily, as a detector can be positioned very close to the surface of the plaque, as opposed to the concave clinical plaques. The obtained results from the simulations in this work were compared with published data (Soares et al., 2001; Cross et al., 2001). As variations in thickness of the exit window of up to 6 μm have been reported (Eichmann et al., 2009), additional simulations were run modifying the thickness of the exit window of the planar plaque in ± 10 μm to study how these variations may affect the results.

[7] Eckert & Ziegler BEBIG GmbH, User's manual Ru–106 eye plaques (Rev. 10), (2011).

TABLE 2.1: Geometrical dimensions of the clinical ^{106}Ru/^{106}Rh plaques simulated in this chapter, as taken from the ICRU 72 Report (ICRU, 2004). The plaques CCX, CCY and CCZ only differ in the number and position of the eyelets. It happens the same for the CIB and CIB–2 models.

Model	Diameter D (mm)	Height h (mm)	Active diameter D_a (mm)	Radius of curvature r (mm)
CCA	15.3	3.3	13.0	12.0
CCB	20.2	5.4	17.8	12.0
CCC	24.8	8.0	22.5	13.0
CCD	17.9	4.3	15.5	12.0
CCX–Y–Z	11.6	2.3	9.5	12.0
CXS	11.6	2.3	7.7	12.0
CGD	22.3	6.1	19.9	13.0
CIA	15.3	3.3	13.0	12.0
CIB/CIB–2	20.2	5.4	17.8	12.0

2.2.2 Simulation conditions

Simulations in this chapter were performed using version 2008.1 of PENELOPE (Baró et al., 1995; Salvat et al., 2009)[8], except the simulations from subsection 2.3.11, which were run with version 2014. The ^{106}Rh beta spectrum used in the simulations was taken from the ICRU Report 72 (ICRU, 2004) (Figure 2.2). The ^{106}Ru beta spectrum ($E_{max} = 39$ keV) and the gamma spectrum from the ^{106}Pd excited states (see Figure 1.4) were not considered, as previous works have done, to compare with the results in the literature. The range of 39 keV electrons in silver is less than 0.01 mm; therefore, these particles cannot traverse the exit window of these plaques, with a thickness of 0.1 mm. Meanwhile, gamma radiation has a minor effect on the dose distributions obtained at depths of clinical interest (0–8 mm); it is assumed in the literature that its effect is only appreciable at greater depths. The validity of this approximation was assessed, as no previous publication reported detailed values on the influence of the ^{106}Pd gamma photons on the depth–dose distribution of these plaques. The beta spectra from the ICRU Report 72 were calculated using empirical expressions which included all the components with contributions greater than 0.3%. The uncertainties of beta spectra calculated with this method are estimated to be of a few percent. More details on the calculation models can be found in the ICRU Report 56 (ICRU, 1997).

The materials (water for the phantom and silver for the plaque) were chosen from the PENELOPE material library. The mass density was 1.00 g cm^{-3} for water and 10.50 g cm^{-3} for silver. The following values for the PENELOPE simulation parameters were chosen for both water and silver: EABS(e^-) = EABS(e^+) = 70 keV, EABS(γ)= 10 keV, C1 = C2 = 0.1, WCC = 30 keV, and WCR = 4 keV. It was verified for some test cases that the dose distributions obtained with these parameters were compatible with those obtained using a detailed simulation, within statistical uncertainties below 0.6% ($k = 3$).

[8] Version 2008.1 corrects some minor bugs respect to version 2008.

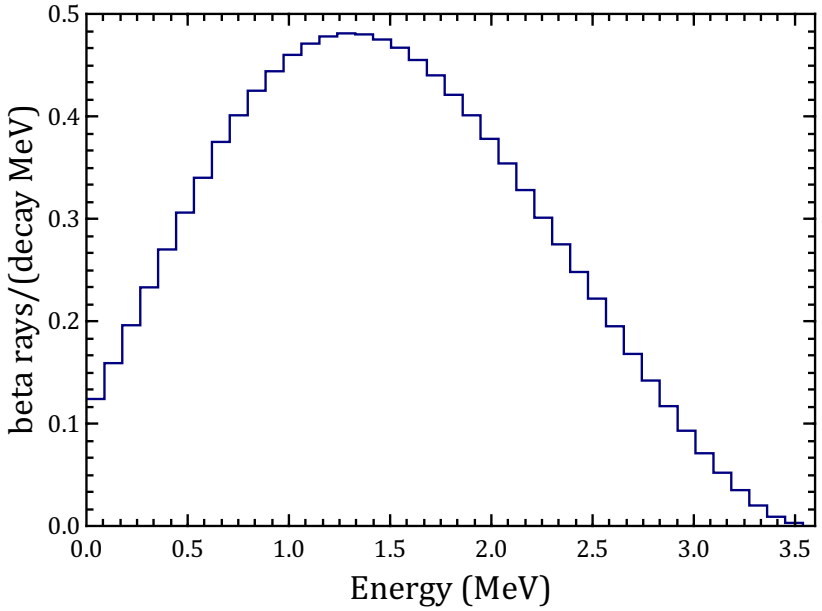

FIGURE 2.2: ^{106}Rh beta spectrum used as source for the simulations of this chapter, taken from the ICRU Report 72 (ICRU, 2004).

Cylindrical symmetry was not considered in the simulations. Although this choice may not appear to be optimal for the symmetric plaque models due to an unnecessary increase in computation time, this approach was preferred to take advantage of the predefined PENELOPE routines, thus reducing the programming effort and the amount of time that was necessary to set up the simulations.

For each run, 2×10^8 histories were simulated, which resulted in a statistical uncertainty of approximately 1–2% ($k = 3$) for most of the estimated dose values. The absorbed dose was scored in a grid composed of $63 \times 63 \times 63$ bins of $0.5 \times 0.5 \times 0.5$ mm^3 in a Cartesian coordinate system whose origin was at the intersection of the central axis of the plaque with its inner surface. The grid ranged from -15.75 mm to $+15.75$ mm in each direction.

For each plaque the following data are presented:

- Depth absorbed dose distributions in 0.5 mm steps from the inner surface of the plaque to a depth of 10.0 mm. Doses at 0 depth of the depth–dose curves were extrapolated from a fit using the doses in the depth range of 0.5–6.0 mm.
- Lateral absorbed dose distributions at six depths of clinical interest (1, 2, 3, 4, 6 and 8 mm, in 0.5 mm steps) and outward from the central axis of the plaques. The maximum lateral distances of the lateral dose profiles were chosen in such a manner that the whole profiles are inside the water phantom for the different depths.

The bins crossing the interface between the plaque and the water phantom are subject to a *partial–volume effect*, as part of their volume contains silver and other part contains water.

As the mass density and the atomic number are much higher for silver than that for water, the energy deposited in those bins, although it is correctly tallied, is not representative of the actual energy deposited at the surface of the plaque. Hence, the relative depth dose values for zero depth were extrapolated from a fit using doses in the depth range of 0.5–6.0 mm. The length of the lateral dose profiles was adjusted for each depth to include bins containing water only, avoiding bins crossing the surface of the plaque.

Monte Carlo simulations provide inherently absolute dose results (in eV/g per history). If we know the activity of the plaque (in MBq), we could obtain the dose rate per unit of activity (mGy h^{-1} MBq^{-1}) for a specific plaque. However, we chose to give the Monte Carlo results of this chapter in relative values for the following reasons: (i) to ease the comparisons with published results (measurements and simulations), the vast majority of which are given as relative dose distributions; and (ii) to give dose distributions typical of a plaque model, rather than those of a specific plaque.

Relative doses are presented in tabulated form to simplify future comparisons and to avoid the additional uncertainties involved in reading values directly from graphs (ICRU, 2004). The uncertainty bars of the graphs represent the statistical uncertainty of the doses estimated, with a *coverage factor*[9] of $k = 3$. Unless otherwise indicated, the doses and statistical uncertainties in this chapter are normalized to the doses at a depth of 1 mm along the central axis. The results were compared with published data as well as with the data provided in the calibration certificates of the available plaques, and with reference data from the manufacturer.

2.3 Results and discussion

A summary of the relative depth–dose data is presented in Table 2.2. The lateral relative dose profiles at several depths of clinical interest are shown in Tables 2.3 and 2.4 for symmetric and asymmetric plaques, respectively.

[9] The coverage factor is the numerical factor that multiplies the combined standard uncertainty to obtain an expanded uncertainty.

TABLE 2.2: Relative absorbed dose data in depth estimated with PENELOPE for the plaques simulated in this work. Absorbed dose and uncertainty values ($k = 3$) are normalized to a percentage of 100% at 1 mm depth. Doses at 0 depth were extrapolated from a fit using values in the depth range of 0.5–6.0 mm.

Plaque	Planar CCB 570	CCA	CCB	CCC	CCD	CCX–Y–Z	CXS	CGD	CIA	CIB/CIB2
Depth (mm)										
0.0	134.9	126.8	124.8	123.8	124.6	131.7	136.9	123.6	141.7	141.8
0.5	117.5	113.4	112.4	111.9	112.3	115.8	118.5	111.8	120.8	120.9
1.0	100.0	100.0	100.0	100.0	100.0	100.0	100.0	100.0	100.0	100.0
1.5	84.8	87.7	88.3	88.3	87.7	84.8	82.8	88.9	83.0	84.5
2.0	71.4	75.5	77.9	77.6	77.1	71.4	67.0	77.9	69.4	71.6
2.5	59.4	64.5	68.2	68.7	66.9	58.5	53.7	68.3	58.1	61.6
3.0	50.0	55.0	59.3	59.0	57.5	48.0	42.3	58.8	48.6	52.4
3.5	41.5	45.9	51.6	51.5	48.9	38.6	33.1	51.3	40.1	44.5
4.0	34.1	38.2	43.9	44.7	41.7	30.8	25.7	44.0	33.0	37.7
4.5	27.9	31.5	37.5	38.2	34.9	24.4	20.0	36.9	27.2	32.2
5.0	22.6	25.8	31.5	32.4	28.8	19.1	15.3	31.4	21.9	26.9
5.5	17.8	20.5	26.4	27.3	23.8	15.0	11.8	26.7	17.7	22.5
6.0	14.3	16.5	21.7	23.0	19.5	11.6	9.0	22.2	14.3	18.3
6.5	11.2	13.0	17.9	19.4	15.7	8.9	6.8	18.3	11.1	15.0
7.0	8.8	10.3	14.5	15.9	12.6	6.8	5.0	15.1	8.8	12.1
7.5	6.7	8.0	11.8	13.3	9.9	5.2	3.8	12.0	6.8	9.7
8.0	5.0	6.1	9.2	10.7	7.8	3.9	2.9	9.5	5.2	7.6
8.5	3.8	4.8	7.2	8.7	5.9	2.9	2.2	7.6	4.0	6.1
9.0	2.9	3.6	5.6	6.8	4.5	2.2	1.6	6.0	3.0	4.7
9.5	2.1	2.6	4.3	5.4	3.4	1.5	1.1	4.7	2.2	3.5
10.0	1.5	1.9	3.2	4.2	2.5	1.1	0.8	3.5	1.6	2.7
Relative average uncertainty (%) ($k = 3$)	0.5	0.3	0.5	0.6	0.4	0.2	0.2	0.6	0.3	0.4

TABLE 2.3: Lateral relative absorbed dose profiles at several depths of clinical interest for the symmetric plaques CCB–570 (planar), CCA, CCB, CCC, CCD, CCX/Y/Z, CXS, and CGD. Data are normalized at 1 mm depth at the central axis. The maximum statistical uncertainty ($k = 3$) is less than 2% for all depths and plaques. The lateral distance values are repeated for each plaque to improve legibility.

Plaque	Depth (mm)	Lateral distance from the central axis (mm)											
Planar CCB 570		0.0	1.5	2.5	3.5	4.5	5.5	6.5	7.5	8.5	9.5	10.5	11.5
	1.0	100.0	100.0	99.3	99.3	99.3	97.5	96.5	93.2	86.2	70.8	38.2	14.7
	2.0	71.4	71.0	70.7	70.4	69.8	69.2	66.4	63.1	56.7	44.2	28.9	15.8
	4.0	34.1	33.7	33.7	33.4	32.5	31.9	29.7	27.3	23.4	18.9	14.1	9.4
	6.0	14.3	14.2	14.0	13.9	13.4	13.2	12.1	10.8	9.6	7.7	5.9	4.2
	8.0	5.0	5.0	4.9	4.9	4.9	4.5	4.2	3.7	3.2	2.7	2.0	1.5
CCA		0.0	1.5	2.5	3.5	4.5	5.5	6.5	7.5	8.5	9.5	10.5	11.5
	1.0	100.0	102.1	105.1	109.6	122.6							
	2.0	75.5	76.9	78.7	81.3	84.1	83.7						
	3.0	55.0	55.4	55.8	55.8	54.3	46.6	27.2					
	4.0	38.2	38.5	38.3	36.9	34.0	27.6	18.2	9.2	4.0	1.7	0.8	0.3
	6.0	16.5	16.4	51.7	14.6	12.9	10.6	7.7	5.0	2.9	1.6	0.8	0.4
	8.0	6.1	6.0	5.7	5.3	4.5	3.8	2.8	2.1	1.3	0.8	0.5	0.2
CCB		0.0	1.5	2.5	3.5	4.5	5.5	6.5	7.5	8.5	9.5	10.5	11.5
	1.0	100.0	102.4	106.0	111.9								
	2.0	77.9	79.9	83.4	88.4	95.2	105.6						
	3.0	59.3	60.5	63.4	68.2	73.6	80.9	90.8					
	4.0	43.9	44.8	47.0	50.6	54.3	58.9	64.8	70.1				
	6.0	21.7	22.3	23.6	24.5	25.7	26.8	26.5	23.3	16.9	9.4	3.3	0.9
	8.0	9.2	9.6	9.6	10.3	10.4	10.4	9.7	8.5	6.4	4.3	2.5	1.3
CCC		0.0	1.5	2.5	3.5	4.5	5.5	6.5	7.5	8.5	9.5	10.5	11.5
	1.0	100.0	102.3	105.4	111.2	120.1							
	2.0	77.6	79.7	83.9	88.3	96.1	105.5	118.2					
	3.0	59.0	61.8	64.6	69.7	75.6	85.1	94.8	108.7				
	4.0	44.7	46.4	48.2	52.8	58.9	66.3	76.0	78.7	102.5			
	6.0	22.9	24.5	26.0	29.0	32.3	37.9	43.9	51.9	61.2	71.9	87.5	
	8.0	10.7	11.3	12.1	13.8	16.0	18.8	21.6	23.9	26.7	26.4	20.9	11.6
CCD		0.0	1.5	2.5	3.5	4.5	5.5	6.5	7.5	8.5	9.5	10.5	11.5
	1.0	100.0	101.6	105.1	110.3	123.4							
	2.0	77.1	78.5	81.4	85.8	92.1	99.7						
	3.0	57.5	58.4	60.1	63.7	67.4	70.7	73.3					
	4.0	41.7	42.2	43.6	45.0	46.4	46.3	41.7	28.3	11.5			
	6.0	19.5	19.4	19.6	19.8	19.1	17.6	14.8	11.0	6.7	3.6		
	8.0	7.7	7.7	7.7	7.6	7.2	6.4	5.2	4.1	2.9	1.8	1.1	
CCX/Y/Z		0.0	1.5	2.5	3.5	4.5	5.5	6.5	7.5	8.5	9.5	10.5	11.5
	1.0	100.0	100.7	101.5	101.7								
	2.0	71.4	70.3	68.0	60.4	40.2	15.2						
	3.0	48.0	46.5	42.8	35.9	24.9	13.4	6.2					
	4.0	30.8	29.6	26.6	22.0	15.9	9.9	5.4	2.8	1.4	0.7	0.3	0.1
	6.0	11.6	10.9	9.9	8.3	6.4	4.5	2.9	1.7	1.0	0.5	0.3	0.1
	8.0	3.9	3.8	3.3	2.8	2.2	1.7	1.2	0.8	0.4	0.3	0.1	0.1
CXS		0.0	1.5	2.5	3.5	4.5	5.5	6.5	7.5	8.5	9.5	10.5	11.5
	1.0	100.0	99.2	95.2	71.8								
	2.0	67.0	64.0	55.8	38.7	18.2	7.4						
	3.0	42.3	39.2	33.1	23.9	14.1	7.2	3.4					
	4.0	25.7	23.6	20.0	15.0	9.8	5.7	3.1	1.6	0.8	0.4	0.2	0.1
	6.0	9.0	8.3	7.1	5.6	4.1	2.8	1.7	1.0	0.5	0.3	0.1	0.1
	8.0	2.9	2.7	2.4	2.0	1.5	1.1	0.7	0.5	0.3	0.1	0.1	0.0
CGD		0.0	1.5	2.5	3.5	4.5	5.5	6.5	7.5	8.5	9.5	10.5	11.5
	1.0	100.0	101.8	105.8	111.1	120.3							
	2.0	77.8	79.5	83.2	87.8	95.0	103.9	115.4					
	3.0	58.7	60.8	63.8	67.9	73.8	81.8	92.3	103.8				
	4.0	44.1	44.8	47.2	50.8	55.8	62.6	70.1	79.0	91.7			
	6.0	22.2	22.7	23.8	25.8	28.5	30.9	33.6	35.0	32.9	21.0	11.3	
	8.0	9.5	10.0	10.5	11.4	12.1	12.9	13.6	13.1	11.5	8.8	5.6	2.9

TABLE 2.4: Lateral relative absorbed dose profiles at several depths of clinical interest for the asymmetric plaques CIA and CIB/CIB–2. Data are normalized at 1 mm depth along the central axis. The maximum statistical uncertainty ($k = 3$) is less than 2% at all depths and for all plaques. Axes convention is sketched on Figure 2.12.

Plaque	Depth (mm)	Lateral distance from the central axis (mm)																		
CIA X axis		−9.5	−8.5	−7.5	−6.5	−5.5	−4.5	−3.5	−2.5	−1.5	0.0	1.5	2.5	3.5	4.5	5.5	6.5	7.5	8.5	9.5
	1.0						151.8	134.2	126.5	118.8	100.0	45.0	19.8	9.6	5.0	2.7	1.5	0.8	0.4	0.2
	2.0					104.0	103.1	98.5	92.8	86.3	69.4	40.2	23.1	12.5	6.8	3.7	2.0	1.0	0.5	0.3
	3.0			12.1	33.9	57.5	66.1	67.3	64.7	60.1	48.6	31.4	20.5	12.4	7.2	4.0	2.2	1.2	0.6	0.3
	4.0		4.8	11.3	22.2	33.8	41.0	43.6	43.1	40.4	33.0	22.9	16.2	10.5	6.4	3.8	2.1	1.2	0.6	0.3
	6.0	1.9	3.6	6.0	9.3	12.6	15.4	16.8	17.1	16.7	14.3	10.5	7.9	5.7	3.8	2.4	1.4	0.8	0.4	0.2
	8.0	1.0	1.6	2.5	3.4	4.5	5.3	5.9	6.1	6.1	5.2	4.0	3.1	2.4	1.6	1.0	0.7	0.4	0.2	0.1
CIA Y axis		0.0	1.5	2.5	3.5	4.5	5.5	6.5	7.5	8.5	9.5									
	1.0	100.0	105.2	114.0	125.6	147.0														
	2.0	69.4	72.8	79.2	87.2	95.5	99.4													
	3.0	48.6	50.3	53.4	57.0	58.7	52.8	30.8	10.6											
	4.0	33.0	33.8	35.0	35.7	34.9	29.3	19.6	9.7	4.2										
	6.0	14.3	14.2	14.0	13.5	12.4	10.4	7.7	5.0	3.0	1.6									
	8.0	5.2	5.2	4.9	4.7	4.2	3.6	2.8	2.0	1.3	.08									
CIB/CIB-2 X axis		−8.5	−7.5	−6.5	−5.5	−4.5	−3.5	−2.5	−1.5	0.0	1.5	2.5	3.5	4.5	5.5	6.5	7.5	8.5	9.5	
	1.0					164.7	145.6	135.4	125.0	100.0	41.2	19.0	9.6	5.2	2.7	1.5	0.9	0.4	0.2	
	2.0				139.1	125.2	115.1	104.4	94.1	71.6	39.5	22.6	12.3	6.8	3.6	2.0	1.0	0.5	0.3	
	3.0			121.0	107.3	96.9	86.6	77.9	68.7	52.4	32.8	20.7	12.6	7.4	4.0	2.2	1.1	0.6	0.3	
	4.0		93.0	86.2	78.3	70.7	63.7	56.7	49.8	37.7	24.9	17.3	10.9	6.5	3.9	2.1	1.1	0.5	0.3	
	6.0	22.8	30.8	34.8	34.8	33.2	30.7	27.3	23.9	18.3	12.9	9.3	6.5	4.1	2.5	1.5	0.8	0.5	0.2	
	8.0	8.6	11.1	12.6	13.5	13.2	12.5	11.3	9.7	7.5	5.4	3.9	2.8	1.9	1.3	0.7	0.4	0.2	0.1	
CIB/CIB-2 Y axis		0.0	1.5	2.5	3.5	4.5	5.5	6.5	7.5	8.5	9.5	10.5	11.5							
	1.0	100.0	107.1	118.3	132.1	155.0														
	2.0	71.6	76.5	84.3	95.9	109.2	126.7													
	3.0	52.4	55.5	60.7	68.5	78.7	91.1	108.3												
	4.0	37.7	39.8	43.3	48.0	55.1	62.6	72.6	83.4											
	6.0	18.3	19.1	20.2	22.1	24.3	26.0	26.6	24.5	17.8	9.5	3.1	0.9							
	8.0	7.5	8.1	8.3	9.0	9.3	9.6	9.2	8.0	6.3	4.1	2.4	1.2							

2.3.1 Planar plaque

The non–clinical planar plaque model CCB 570 was first used by Soares et al. (2001) and Cross et al. (2001). Soares et al. (2001) compiled dose data measured using different detectors, different materials and by different investigators to find a 'best fit' for all data that were available at the time. No further experimental data for this plaque have been published since then. The dataset included measurements conducted in water and plastic materials with extrapolation chamber, radiochromic film, TLD 0.3 mm, TLD 1 mm, plastic scintillator, alanine detector and diamond detector. Cross et al. (2001) performed simulations using the EGS4 (Kawrakow et al., 2009) and ACCEPT 3.0 (Halbleib et al., 1992) codes and compared their results with the available published data. Because the published calculations and measurements had been conducted with different materials, they converted all dose distributions to dose–to–water distributions using appropriate scaling factors. Those factors were obtained empirically as a function of the effective atomic number of the medium, and of the relative stopping power of the medium with respect to water (ICRU, 2004). This data processing procedure may have added some uncertainty to the final results.

The depth–dose data from this work are more consistent with the published measurements than the estimations using the EGS4 and ACCEPT 3.0 codes (Table 2.5). Although the PENELOPE results exhibit the smallest difference at all depths, the differences for all codes are below the measurement uncertainty, reported to be less than 10% (Cross et al., 2001). The statistical uncertainties for the PENELOPE results were below 1% ($k = 3$). The uncertainties of the results obtained with EGS4 and ACCEPT 3.0 were not reported, even though they are suggested to be much lower than the measurement uncertainty (Cross et al., 2001).

TABLE 2.5: Differences in relative depth–doses estimated for the planar plaque with respect to measurements among the estimations performed with the Monte Carlo codes EGS4, ACCEPT 3.0, and PENELOPE.

Depth (mm)	EGS [Cross et al. (2001)]	ACCEPT 3.0 [Cross et al. (2001)]	PENELOPE [this work]
2.0	−3.7%	−3.3%	−1.3%
3.0	−4.5%	−2.7%	−1.5%
4.0	−3.3%	−2.6%	−1.2%
5.0	−3.4%	−2.0%	−0.8%
7.0	−1.5%	−0.5%	−0.2%
10.0	−0.8%	−0.6%	−0.4%

Lateral dose profiles at several depths of clinical interest were also estimated and compared with the values provided by Cross et al. (2001) in Table I of their paper (see Figure 2.3). The differences at the origin are a consequence of the differences in depth–doses shown in Table 2.5. There are also some differences (of approximately 0.5 mm) in the distance of the dose fall–off; this effect is specially remarkable at shallow depths: at a 1 mm depth, a 50% dose value appears at approximately 10.5 mm in the Cross' profile, whereas in this work, a

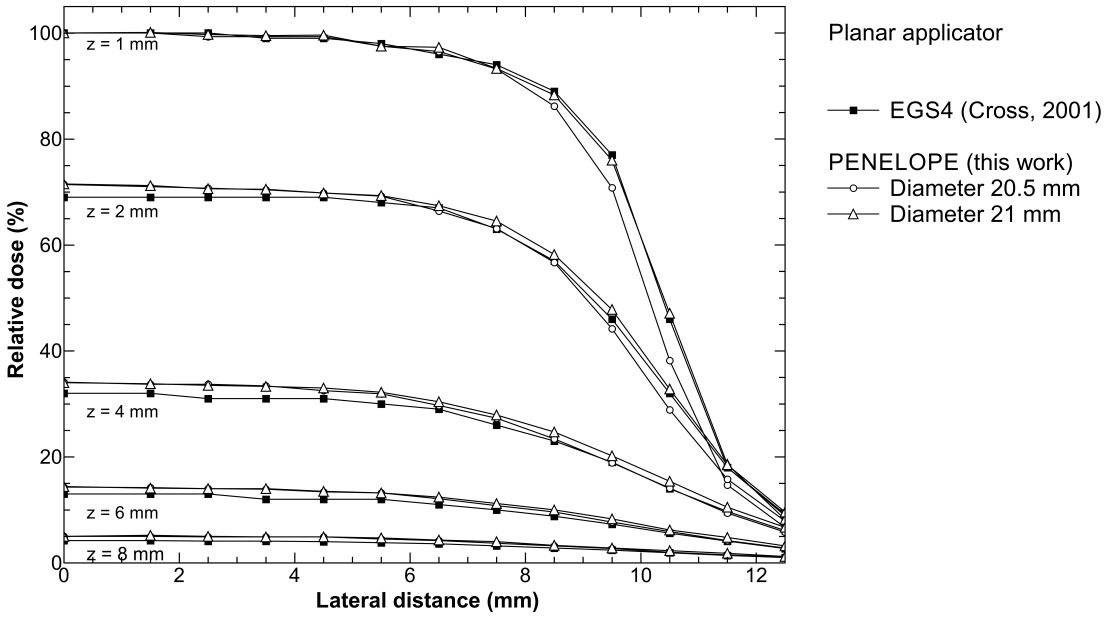

FIGURE 2.3: Lateral profiles estimated in this work for a planar plaque, compared with the profiles estimated by Cross et al. (2001). Profiles are normalized on the central axis and at a depth of 1.0 mm. A better agreement is obtained in the lateral dose fall–off distance when a diameter of 21.0 mm is used in the simulation.

50% dose value appears at approximately 10.0 mm from the central axis. Although Cross et al. (2001) stated in the main text of their paper that the planar plaque had an active diameter of 20.5 mm, their Table I indicates an active diameter of 21 mm. To check if this difference in active diameter could explain the discrepancy in the lateral profiles, a simulation was performed assuming an active diameter of 21 mm, for which the dose fall–off distances were found to be more consistent (see Figure 2.3). However, this 0.5 mm change in active diameter did not appreciably affect the depth–dose distribution. The values tabulated in this work for the planar plaque are provided assuming an active diameter of 20.5 mm.

Variations in the thickness of the exit window of ± 10 μm respect to the nominal value do not affect the result of the simulations. The differences in the depth–dose curve respect to that obtained using the nominal value of 100 μm are within the attained relative standard statistical uncertainty (0.3%).

The results obtained for the planar plaque validate the Monte Carlo simulation performed with PENELOPE as a reliable method to estimate the absorbed dose distributions produced by ^{106}Ru/^{106}Rh ophthalmic plaques.

2.3.2 CCX/CCY/CCZ plaques

CCX/CCY/CCZ plaque models are designed for the treatment of retinoblastoma. Because the only difference among these plaques is in the number and the position of the eyelets, the

dose distribution is identical for all three models. Few data either experimental or simulated on CCX plaques are available in the literature.

Kirov et al. (2005) used the 3D scintillation dosimetry method to measure the 3D dose distributions for two CCX plaques. The method relies on the observation of scintillation light from an irradiated liquid scintillator volume, which acts simultaneously as a phantom material and as a dose detector. Planar images are acquired at multiple angles to obtain the light emission density in each voxel of the volume following tomographic reconstruction. The dose values are approximately proportional to these density values. The 3D dose measurements were compared against radiochromic film and diode measurements. A drawback of this method is that the volume between the inner surface of the plaque and the distal edge of the plaque cannot be measured because the plaque blocks the scintillation light. Unfortunately, this 'blocked' volume is of most clinical interest because it is the closest volume to the plaque. The stated uncertainty was ∼25%, which is larger than the uncertainty reported using other methods (Soares et al., 2001).

Fuss et al. (2011) simulated dose distributions for the CCX plaque using the LEPTS Monte Carlo code. After comparing their results with published data for CCA (Sánchez-Reyes et al., 1998) and CCB (Taccini et al., 1997; Cross et al., 2001) plaques, they concluded that the previous works might have underestimated the dose in the low–dose region. However, the depth–dose distributions estimated in this work indicate that Fuss et al. (2011) actually overestimated the dose in the low–dose region by approximately 10–15% (see Figure 2.4), which most likely occurred because of the marked differences in the beta spectrum used in their simulation (experimentally determined) and the physical models implemented in their code.

The results presented in this thesis are in excellent agreement with the data provided in the calibration certificates for three CCX plaques and with the depth–dose reference data from the manufacturer. They are also compatible, within the experimental uncertainty, with the depth dose measurements performed by Kirov et al. (2005).

Figure 2.5 shows a comparison of the PENELOPE lateral dose profile estimated at a 5.5 mm depth with the experimental data measured at a 5.4 mm depth by Kirov et al. (2005). The simulation results agree with the measurements within the experimental uncertainty (25% for the 3D scintillator and 15% for the radiochromic film). The statistical uncertainty of the simulated profile is below 0.3% ($k = 3$). The asymmetry in the experimental data may occur because of a inhomogeneous distribution of the radioisotope in the measured plaque.

2.3.3 CXS plaque

The CXS and CCX plaques have an identical shape. The difference between them lies in their active diameter, which is 9.5 mm for the CCX and 7.7 mm for the CXS plaque, as the latter model is designed to treat retinoblastomas of small diameters and heights. Because there are no published data for the CXS plaque, the estimated depth–dose distribution was only compared with the manufacturer's data, which were obtained with a plastic scintillator. The difference in the relative doses was less than 1.3% [the statistical uncertainty was less than

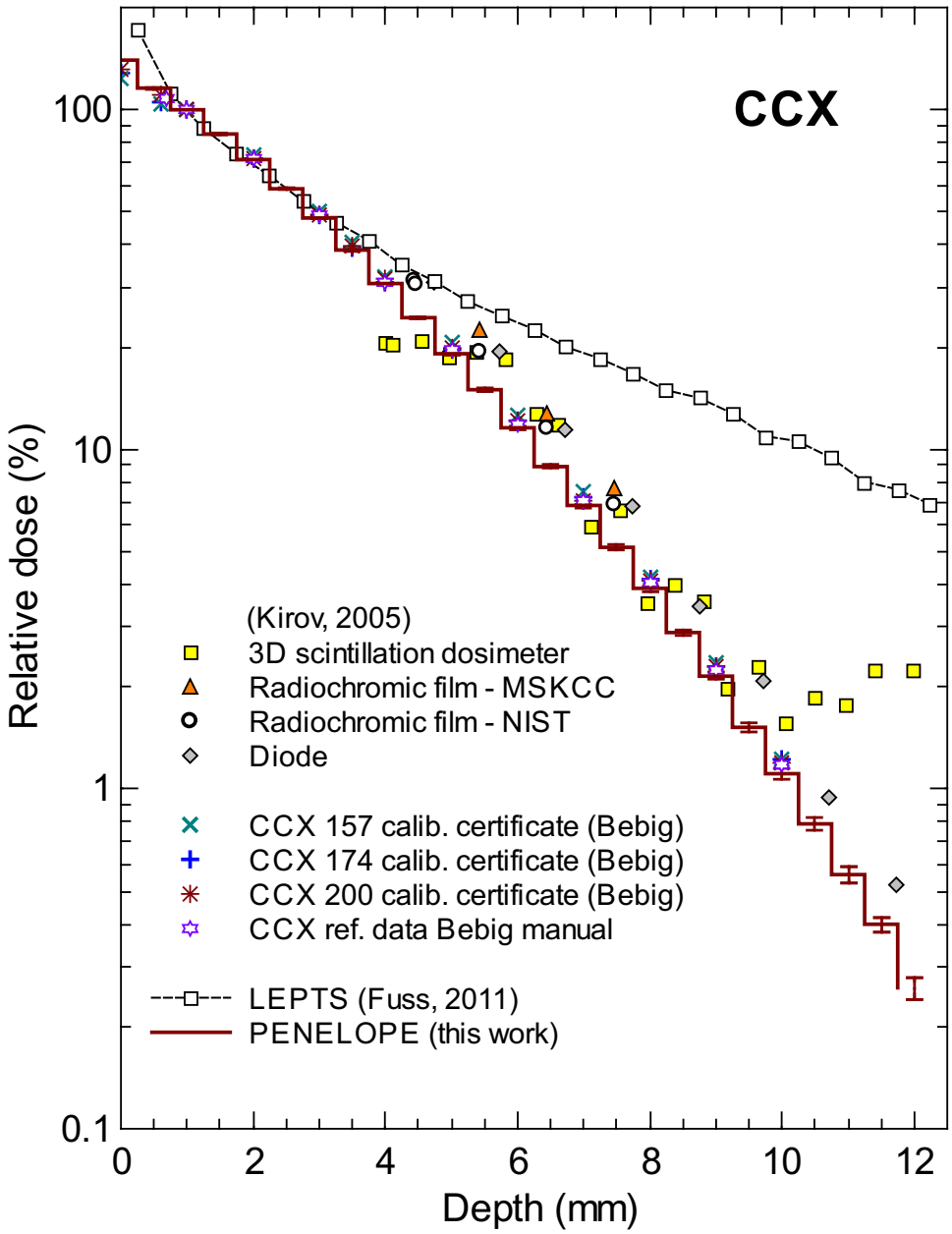

FIGURE 2.4: CCX depth–dose distribution estimated in this work compared with (a) the experimental results reported by Kirov et al. (2005); (b) the data from the calibration certificates for three CCX plaques; (c) the reference depth–dose data from the BEBIG user's manual; and (d) the simulation results by Fuss et al. (2011) using the code LEPTS. The results from PENELOPE simulations show good agreement with the measurements performed by the manufacturer. Previous measurements appear to overestimate these depth–dose values. The LEPTS simulation strongly overestimates the depth–dose distribution for depths greater than 3 mm. Uncertainty bars of PENELOPE data represent the statistical uncertainty with $k = 3$.

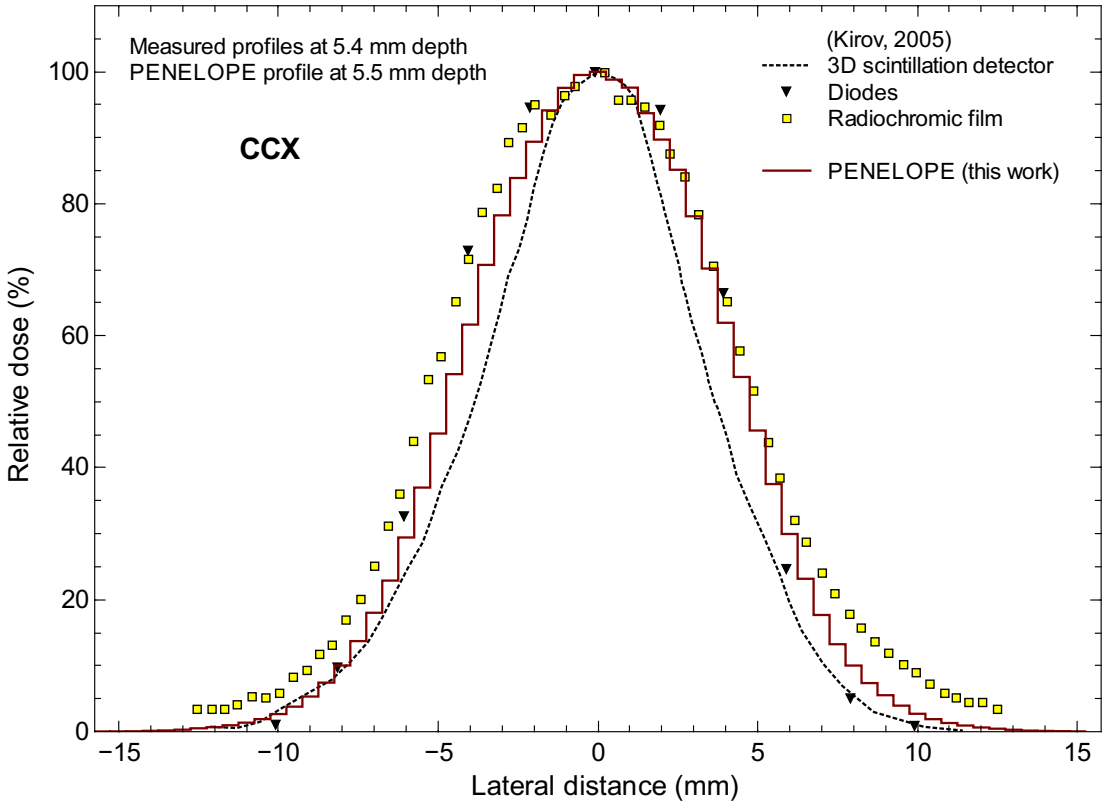

FIGURE 2.5: Comparison of the CCX lateral profile estimated in this work with the experimental results provided by Kirov et al. (2005). Dose distributions were normalized at the central axis. Statistical uncertainty for simulated profiles is below 0.3% ($k = 3$). The stated uncertainties for the measurements by Kirov *et al.* are about 25% for the 3D scintillator, and 15% for the radiochromic film. Uncertainty bars are not shown for clarity.

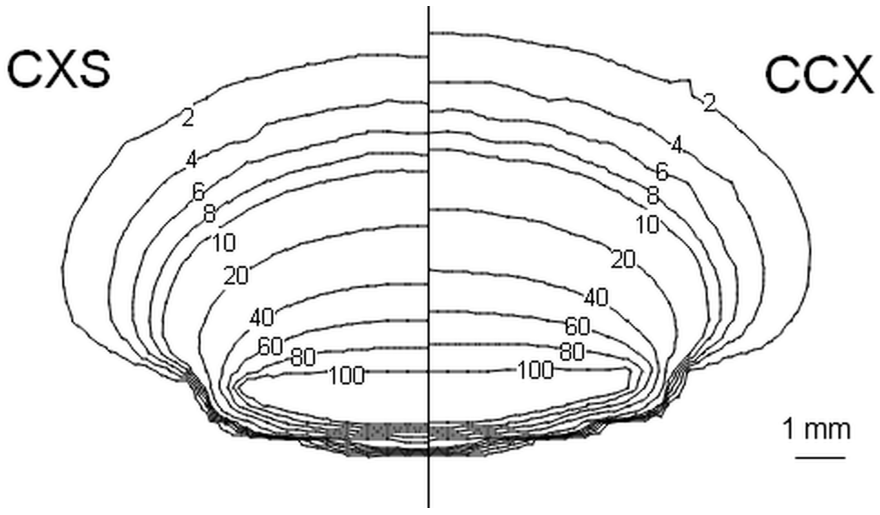

FIGURE 2.6: Relative isodose contours for the CXS plaque against the CCX plaque at a plane containing the symmetry axis. The isodose lines for both plaque models are normalized at a depth of 1 mm.

0.5% ($k = 3$)]. Figure 2.6 shows a comparison of the simulated dose distributions produced by CXS and CCX plaques at a plane containing the symmetry axis of the plaque, where the effect of the greater active diameter of the CCX model on the isodose lines is shown.

2.3.4 CCC plaque

Only one paper provides results for the CCC plaque: Kovačević et al. (2005) measured the CCC depth–dose distribution with $1 \times 1 \times 1$ mm^3 TLD in a Plexiglas phantom and reported a combined uncertainty of 6% ($k = 1$). They studied two plaques produced with a difference of one year, designated as 'old' and 'new'. Figure 2.7 shows a comparison of the present work's estimations with data from Kovačević et al. (2005) and with the reference data from the manufacturer. The results estimated with PENELOPE simulations agree within 3% with the reference data from the manufacturer and with the data from the calibration certificate of the 'new' plaque of Kovačević et al. (2005), whereas the difference reaches 10% with respect to the TLD data.

2.3.5 CCD plaque

No published data are available for the CCD plaque. Hence, the results of this work could only be compared with the depth–dose reference data obtained from the plaque's manual. An excellent agreement was observed (within 0.3%) for the data between depths of 0.5 mm and 10.0 mm. The statistical uncertainty of the simulation was better than 0.9% ($k = 3$).

2.3.6 CGD plaque

Only two references contain dose data for the CGD plaque. One is the work of Kaulich et al. (2004), who analyzed the quality assurance procedures followed by the manufacturer in producing the plaques. One criticism to the measurement system employed by the manufacturer prior to 2001 was the large volume of the used scintillator (8 mm^3). However, in 2001 BEBIG began to use a much smaller scintillator, of 0.4 mm^3, with a calibration traceable to the NIST. As part of their analysis, Kaulich et al. (2004) determined depth–dose curves using a scintillator detector with a volume of 0.8 mm^3 and compared their measurements with the depth–dose data provided in the calibration certificate for a CGD plaque measured with the manufacturer's improved measurement system. The second reference is the work by Barbosa et al. (2015), who designed a spherical phantom made of solid water with the dimensions of the eye to measure the dose distributions with TLD at several depths. They reported standard uncertainties of about 1.5% for the measured doses.

Depth–dose distributions simulated in this chapter are statistically compatible with the reference data from the 2011 user's manual for the plaque (Figure 2.8). However, the difference in the relative dose compared to the findings of Kaulich et al. (2004) is up to 3.5%. The measurements conducted by the manufacturer prior to 2001 show a relative dose that is up

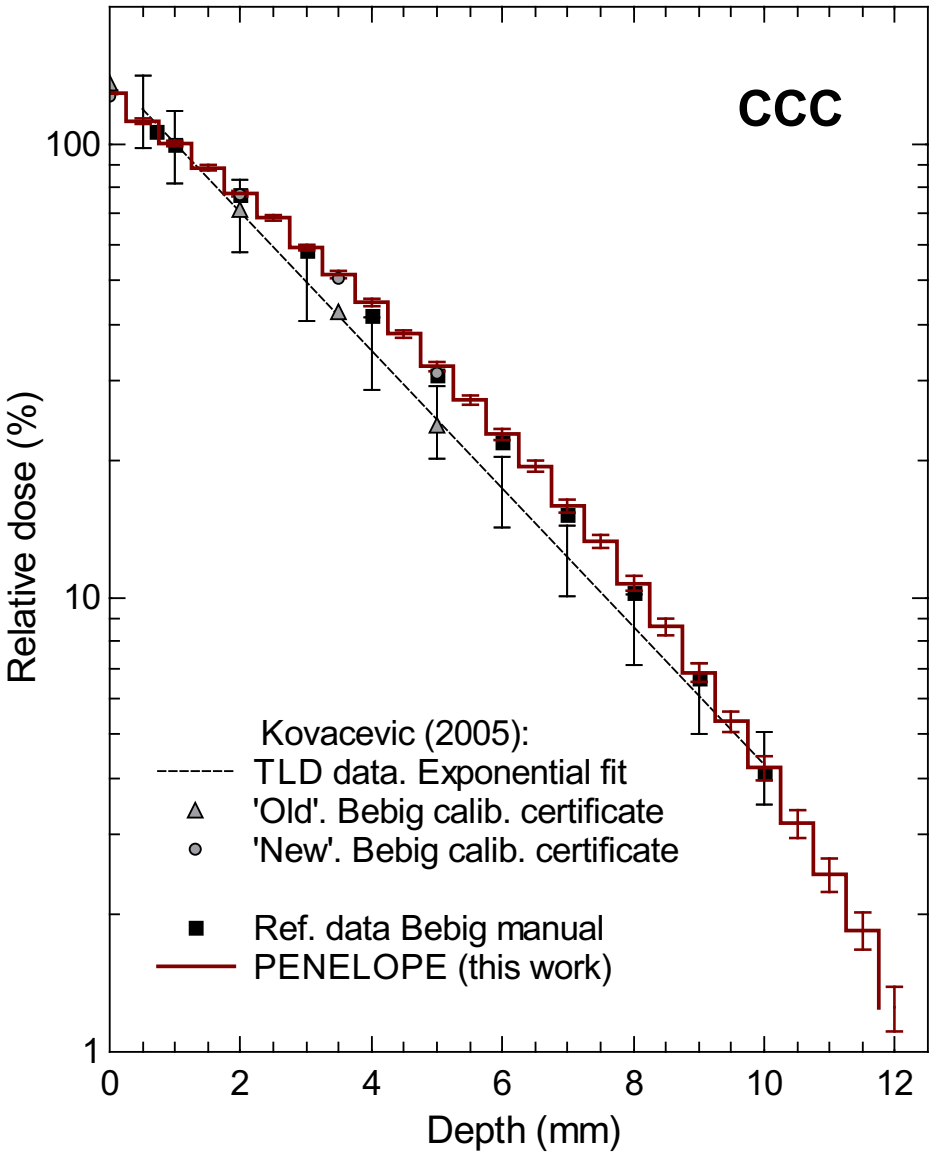

FIGURE 2.7: CCC depth–dose distribution estimated in this work compared with results by Kovačević et al. (2005): (a) TLD measurements; (b) data provided in the calibration certificates for two CCC plaques with production dates separated by one year and designated as 'old' and 'new'; and (c) the reference data from the manufacturer. The statistical uncertainty of the PENELOPE simulation results is less than 1.4% ($k = 3$).

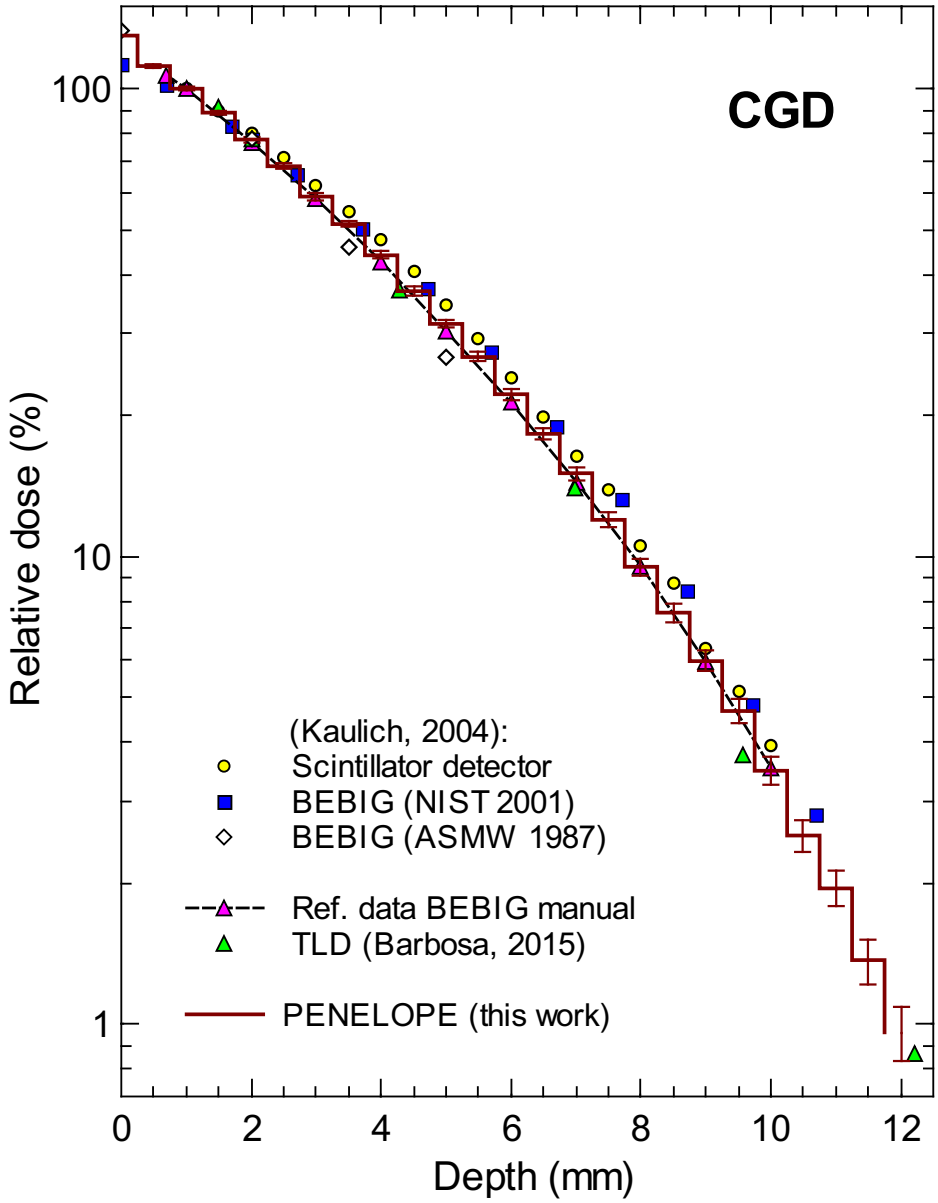

FIGURE 2.8: CGD depth–dose curve estimated in this work compared with published data. From the work by Kaulich et al. (2004): (a) measurements performed using a scintillator of 0.8 mm^3; (b) data from the calibration certificate (ASMW 1987) measured with a scintillator of 8 mm^3; and (c) data from the calibration certificate measured with a scintillator of 0.4 mm^3 (NIST 2001). From the work by Barbosa et al. (2015), TLD measurements. Reference data from BEBIG manual is also included. The statistical uncertainty of the PENELOPE simulation results is less than 1.2% ($k = 3$).

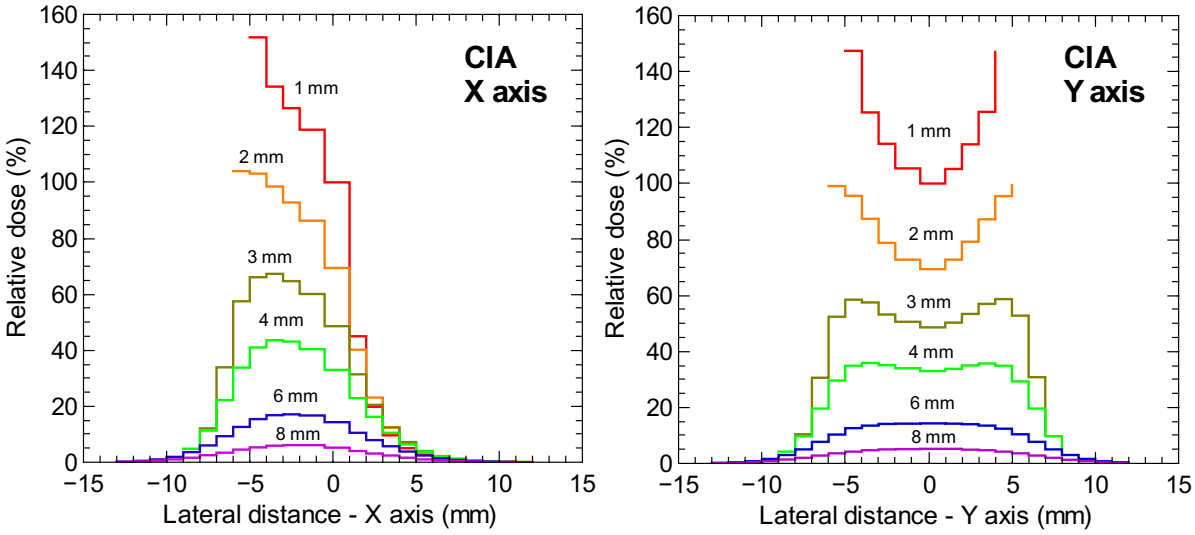

FIGURE 2.9: Lateral dose distributions estimated with PENELOPE at depths of 1, 2, 3, 4, 6 and 8 mm along the X and Y axes for the asymmetric CIA plaque. The axes convention is the same as the one shown on Figure 2.12 for the CIB/CIB–2 plaques. Dose profiles are normalized at the central axis of the plaque, at a depth of 1 mm. The statistical uncertainty of the PENELOPE simulation results is less than 0.8% ($k = 3$). Uncertainty bars are not shown for clarity.

to 6% lower than the PENELOPE estimations and up to 9% lower than the measurements conducted using small–volume scintillators. These observations might be explained by a dose–averaging effect due to the large volume of the scintillator used by the manufacturer prior to 2001. Similar differences were observed with the measurements by Barbosa et al. (2015). The maximum difference between their measurements and the simulations from this chapter is about 4% at a depth of 4.3 mm.

2.3.7 CIA plaque

The CIA plaque is designed to treat ciliary body melanomas or melanomas close to the iris. Because of this purpose, the plaque has an asymmetric shape with a cut–out section, which increases the difficulty of measuring or calculating the dose distribution. This difficulty may explain the lack of published data for this plaque. The relative depth–dose distribution estimated in this work was compatible within 1% (with a statistical uncertainty less than 0.7% ($k = 3$)) with the reference data provided by the manufacturer. Figure 2.9 shows the asymmetric lateral dose distributions obtained at several depths along the X and Y axes. The axes convention is the same as the one shown on Figure 2.12 for the CIB/CIB–2 plaques.

2.3.8 CIB/CIB–2 plaques

Similar to the CIA model, the CIB/CIB–2 plaques are designed to treat ciliary body melanomas or melanomas close to the iris. However, the CIB/CIB–2 plaques have a larger diameter and height than the CIA model. The only difference between the CIB and CIB–2 plaques is the number and location of the eyelets. Hence, the dose distribution is identical for the two models. The relative depth–dose distribution estimated with PENELOPE was compatible within the statistical uncertainty with the reference data provided by the manufacturer. The mean difference in the relative dose was 0.4% and the maximum difference was 3% at a depth of 2.0 mm. The attained maximum relative statistical uncertainty was less than 1.0% ($k = 3$). Figure 2.10 shows dose and statistical uncertainty maps for planes at several depths of interest for the CIB plaque. The statistical uncertainties are similar to those obtained for the other plaques. Figure 2.11 shows dose maps on planes parallel to the central axis, along the X axis. For axes convention, see Figure 2.12.

In the only available study providing dose data on CIB plaques, Taccini et al. (1997) measured the dose distributions for a number of plaque models using radiochromic film. For the CIB plaque they reported isodose contours at a plane perpendicular to the central axis at a depth of 4.5 mm. Depth–dose data were not reported. A large discrepancy exists between the planar dose distributions estimated in this work and those presented by Taccini et al. (1997) (Figure 2.12). The shapes of the isodose lines are completely different and do not appear to correspond to the shape of the CIB plaque. As Taccini et al. (1997) also examined a COB plaque, which has a deeper cut–out than the CIB model, it is likely that the dose distribution attributed to the CIB plaque actually corresponded to the COB plaque.

2.3.9 CCA plaque

The CCA plaque, together with the CCB, is one of the most commonly used plaques. It is designed to treat mainly choroidal melanomas. Several references are available, including Monte Carlo simulations (Davelaar et al., 1992; Sánchez-Reyes et al., 1998; Brualla et al., 2012, 2013, 2014; Barbosa et al., 2014) and measurements conducted with polymer gel (Chan et al., 2001) and radiochromic film (Taccini et al., 1997; Heilemann et al., 2015). The depth–dose curve estimated in this work was compared with the results from the previous references, with the calibration certificates for three CCA plaques, and with the reference data provided by the manufacturer. As shown in Figure 2.13 the results from the simulations carried out in this work are compatible within the statistical uncertainty with the data from the calibration certificates and with the reference data provided by the manufacturer. However, large discrepancies ($\sim$15%) were observed compared to the early simulations conducted by Davelaar et al. (1992), which might be due to the approximations applied by the authors in their physical models to reduce simulation time. Large differences were also noted compared to the PENELOPE simulation by Sánchez-Reyes et al. (1998). Unfortunately, their study suffered from important flaws (Brualla et al., 2012).

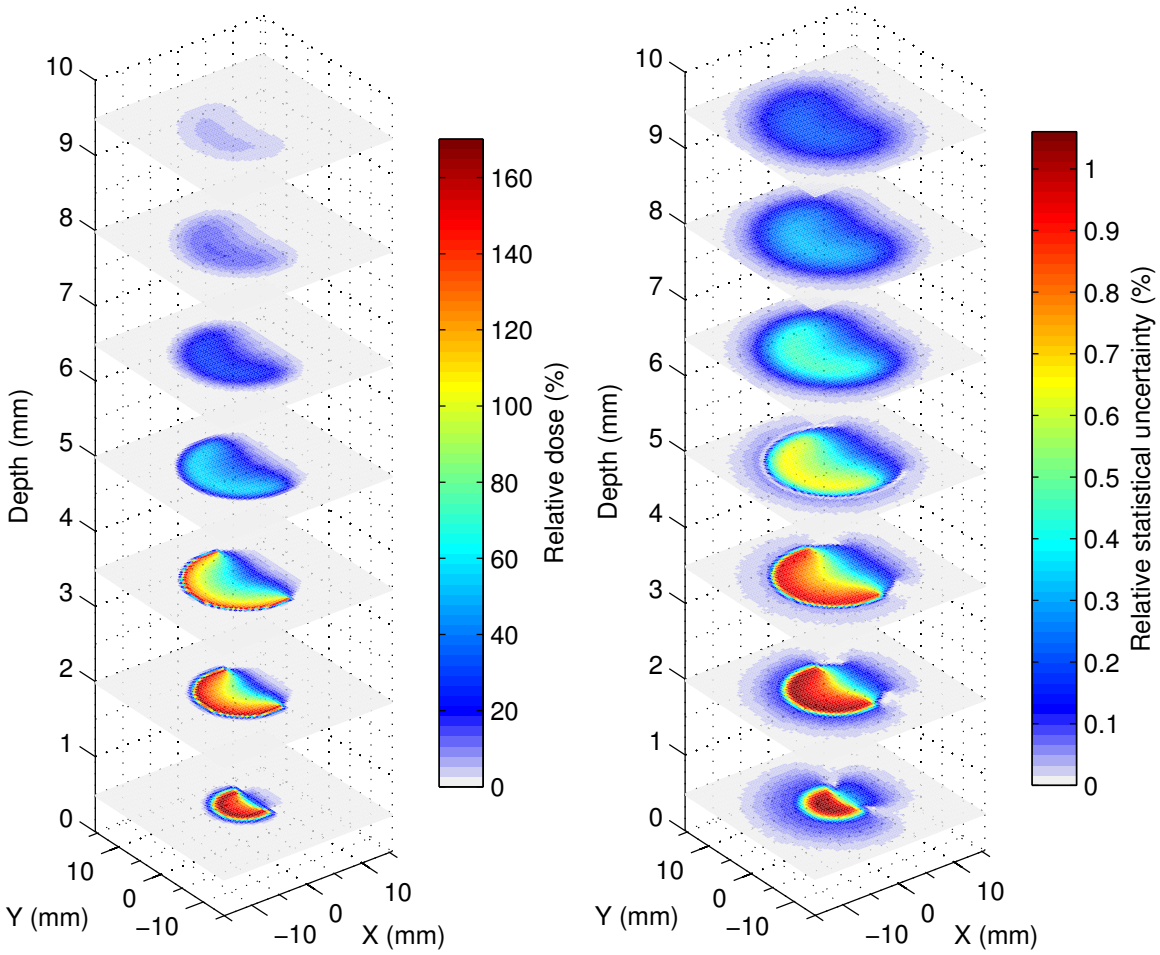

FIGURE 2.10: Dose and statistical uncertainty maps for the CIB/CIB–2 plaque models at planes perpendicular to the central axis. Both, dose values and statistical uncertainty values ($k = 3$) are normalized to the dose value (100%) of the bin centered at (X, Y, Z)=(0, 0, 1) mm.

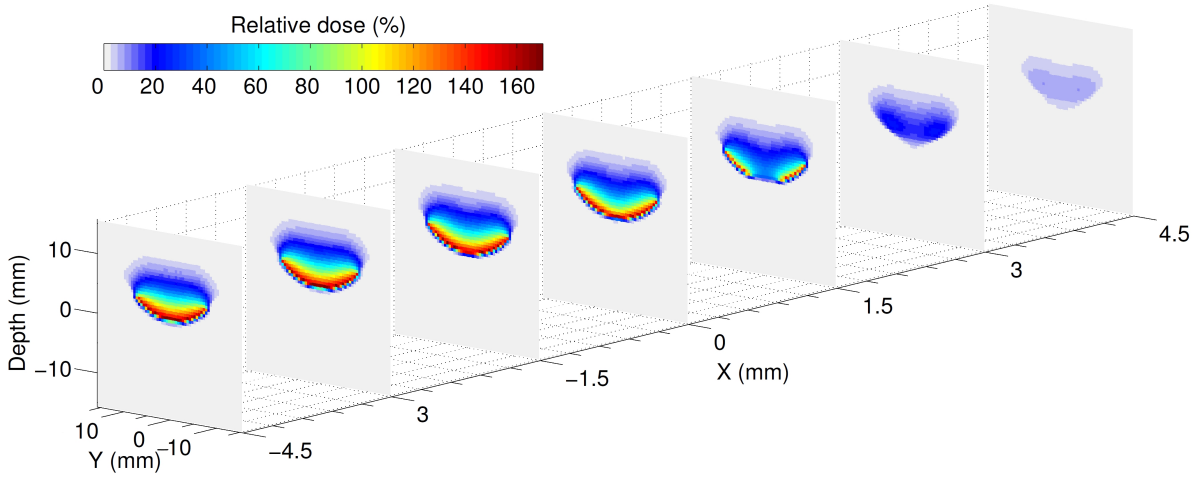

FIGURE 2.11: Dose maps for the CIB/CIB–2 plaque models at planes parallel to the central axis. Doses are normalized to the dose value (100%) of the bin centered at (X, Y, Z) = (0, 0, 1) mm. For axes conventions see Figure 2.12(c). It is apparent the asymmetry of the dose distribution along the X axis due to the notched geometry of the plaque.

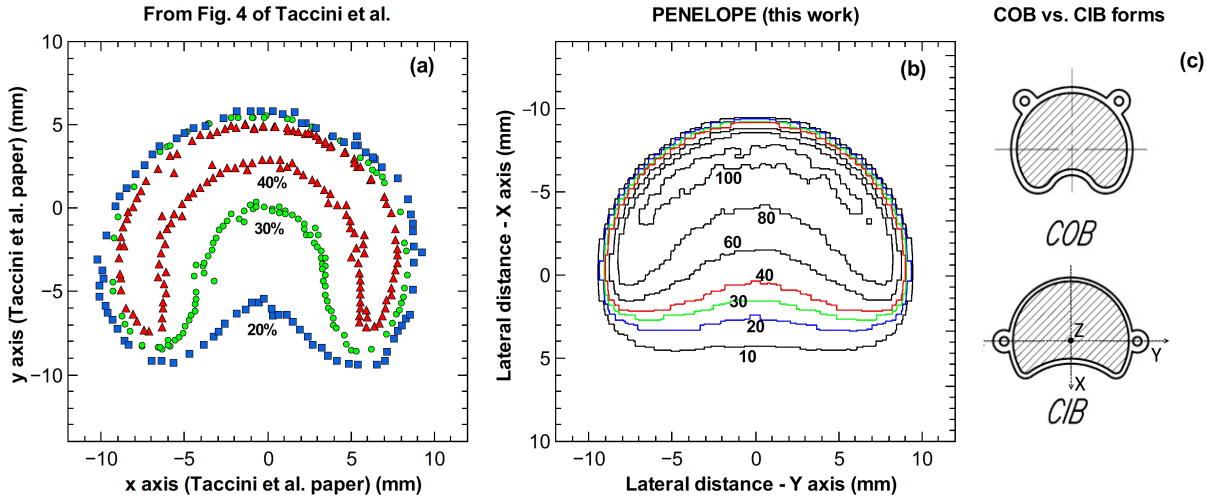

FIGURE 2.12: Isodose lines for a CIB plaque in a horizontal plane at a 4.5 mm depth, as (a) reported by Taccini et al. (1997), measured using radiochromic film, and (b) estimated in this work using PENELOPE. Both dose distributions are normalized to 100% at a point in the central axis at a 2 mm depth. In (c), the geometrical forms of the COB and CIB plaques are shown. It is likely that the dose distribution attributed by Taccini et al. (1997) to the CIB plaque actually corresponds to the COB plaque. The axes convention shown for the CIB plaque was used also for the CIB–2 and CIA plaques.

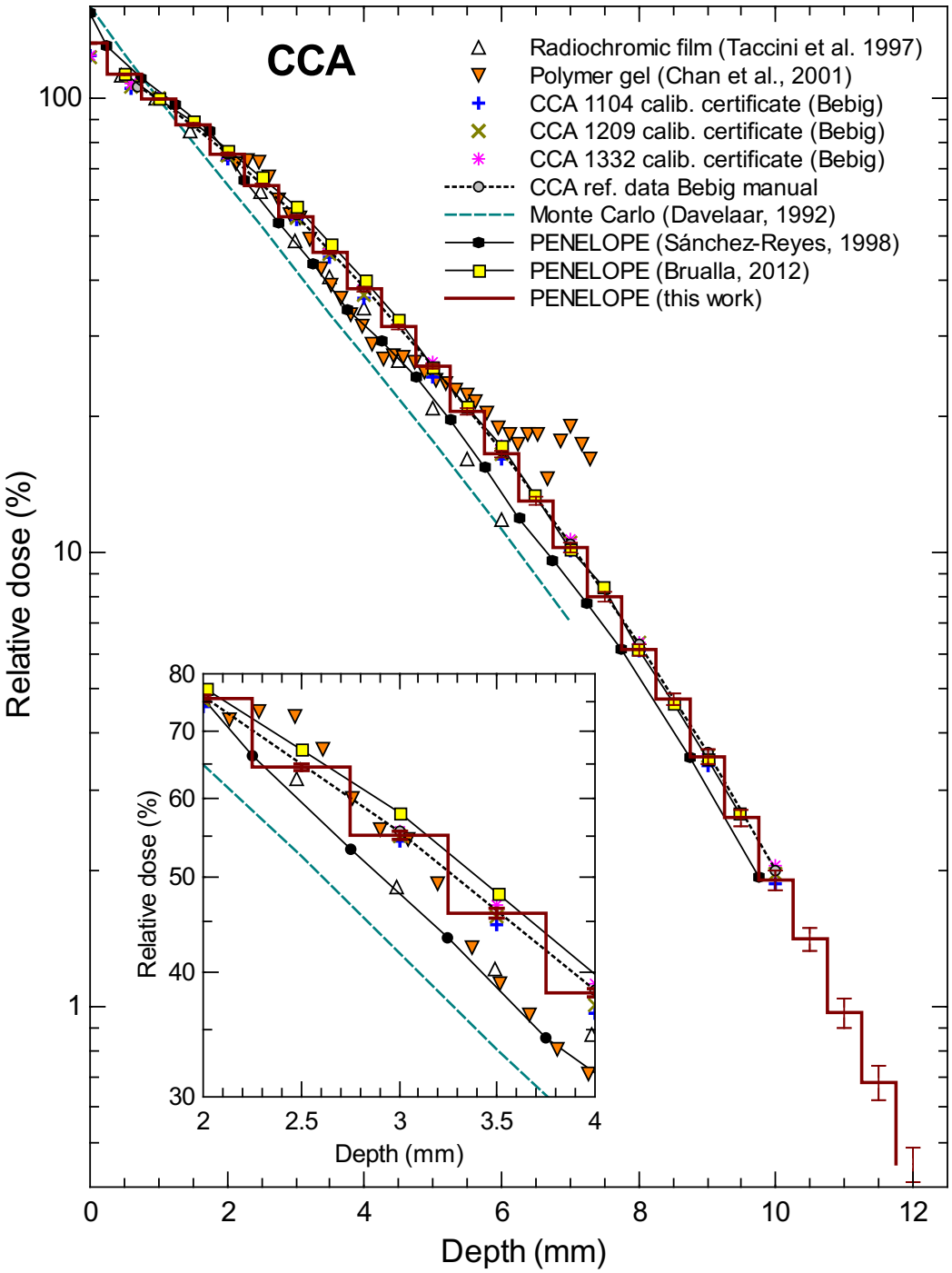

FIGURE 2.13: Depth–dose curve estimated in this work for the CCA plaque compared with (a) measurements performed using radiochromic film (Taccini et al., 1997); (b) measurements using polymer gel (Chan et al., 2001); (c) data from the calibration certificates for three CCA plaques; (d) reference data from the manufacturer; (e) Monte Carlo simulations by Davelaar et al. (1992); and (f) PENELOPE simulations conducted by Sánchez-Reyes et al. (1998) and Brualla et al. (2013). The statistical uncertainty of the PENELOPE simulation results in this work is less than 0.8% ($k = 3$).

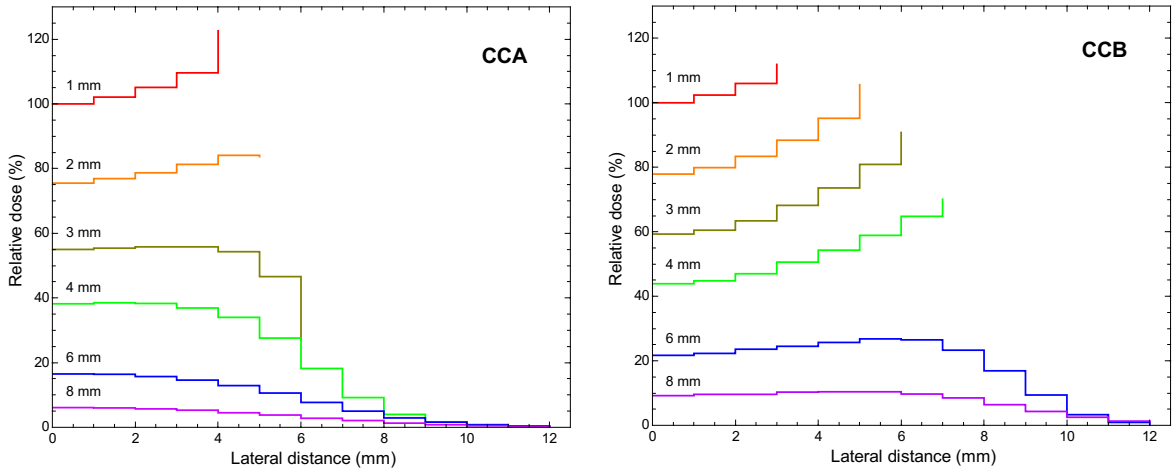

FIGURE 2.14: Lateral dose distributions estimated using PENELOPE at 1, 2, 3, 4, 6 and 8 mm depths for CCA (LEFT) and CCB (RIGHT) plaques. Dose profiles are normalized at the central axis of each plaque, at a depth of 1 mm. The statistical uncertainty ($k = 3$) is less than 0.8% for the CCA and less than 1.1% for the CCB plaque. Uncertainty bars are now shown for clarity.

The agreement with the simulations performed by Brualla et al. (2012, 2013) using PENELOPE is notably better, although a difference that is greater than the statistical uncertainty (less than 1% in both cases) persists. For example, at a depth of 3 mm, the relative dose observed by Brualla et al. (2013) is 58% and 55% in this work. This discrepancy may occur because Brualla et al. (2013) set the diameter of the active area as 14.7 mm, whereas according to the ICRU Report 72 (ICRU, 2004), the active diameter for CCA plaques is 13.0 mm, which is the value used in this work. To test this hypothesis, an additional simulation was performed using an identical plaque geometry but with the active diameter set to 14.7 mm. This change reduced the difference compared to Brualla et al. (2013, 2014) from 1.8% to 0.6% in the depth range of 1–4 mm, but it increased the difference for greater depths from 0.3% to -1.2%. This result suggests that another factor contributes to the differences between the depth–dose distribution estimated in this work and the results of Brualla et al. (2013). This factor may be the different choices regarding the ^{106}Rh beta spectrum. The spectrum used by Brualla and coworkers was obtained by random sampling from the beta decay spectrum corresponding to the disintegrations with the highest yields. To that purpose, they adapted the Fortran code EFFY2 (García-Toraño and Grau-Malonda, 1985) which calculates the beta spectra applying the Fermi theory of beta decay. The differences between the spectrum from the ICRU Report 72 used in this chapter and the spectrum obtained using EFFY2 were evaluated by comparing the depth–dose curves obtained for the CCA plaque using both spectra as source for the simulations, with the same geometry and simulation parameters. The mean difference in the range 1–12 mm of depth was 0.5%, with a maximum difference of 1.5% at a depth of 2.5 mm.

Figure 2.14 (LEFT) shows the CCA lateral dose distributions at several depths simulated in this work.

Considering the improved agreement between the depth–dose distribution estimated in this work and the available published experimental results, respect to previously published works, the results presented here appear to represent the most reliable dataset for CCA plaques.

2.3.10 CCB plaque

For the CCB model there is an important lack of agreement among the published experimental results. They agree only within 10%, so it is difficult to favor one result over the others (Soares et al., 2001; Cross et al., 2001). Even larger differences are observed among the published Monte Carlo simulation studies. Cross et al. (2001) presented the dose distributions computed using different Monte Carlo codes (ACCEPT 3.0, EGS4, MCNP4B, GEANT3 and the code from Davelaar et al. (1992)) for a CCB plaque, for which measurements were also conducted by Soares et al. (2001). Unfortunately, a poor agreement was found among the available simulations, and only the results of ACCEPT 3.0 agreed with the experimental values.

Figure 2.15 (LEFT) shows the relative depth–dose distribution obtained in this work compared to the published measurements. The results from this work agree with the experimental values measured using scintillator detectors (Kaulich et al., 2005) and with the manufacturer's reference data for the CCB plaque model. In Figure 2.15 (RIGHT), the simulation results of this work are compared with other Monte Carlo simulations provided in the literature. The presented results are statistically compatible with those of Brualla et al. (2013), which were also obtained using the PENELOPE code. Although Sánchez-Reyes et al. (1998) also used PENELOPE, their results are flawed (Brualla et al., 2012) and should be discarded. Figure 2.14 (RIGHT) shows the lateral dose distributions, tallied from the symmetry axis outwards, at several depths.

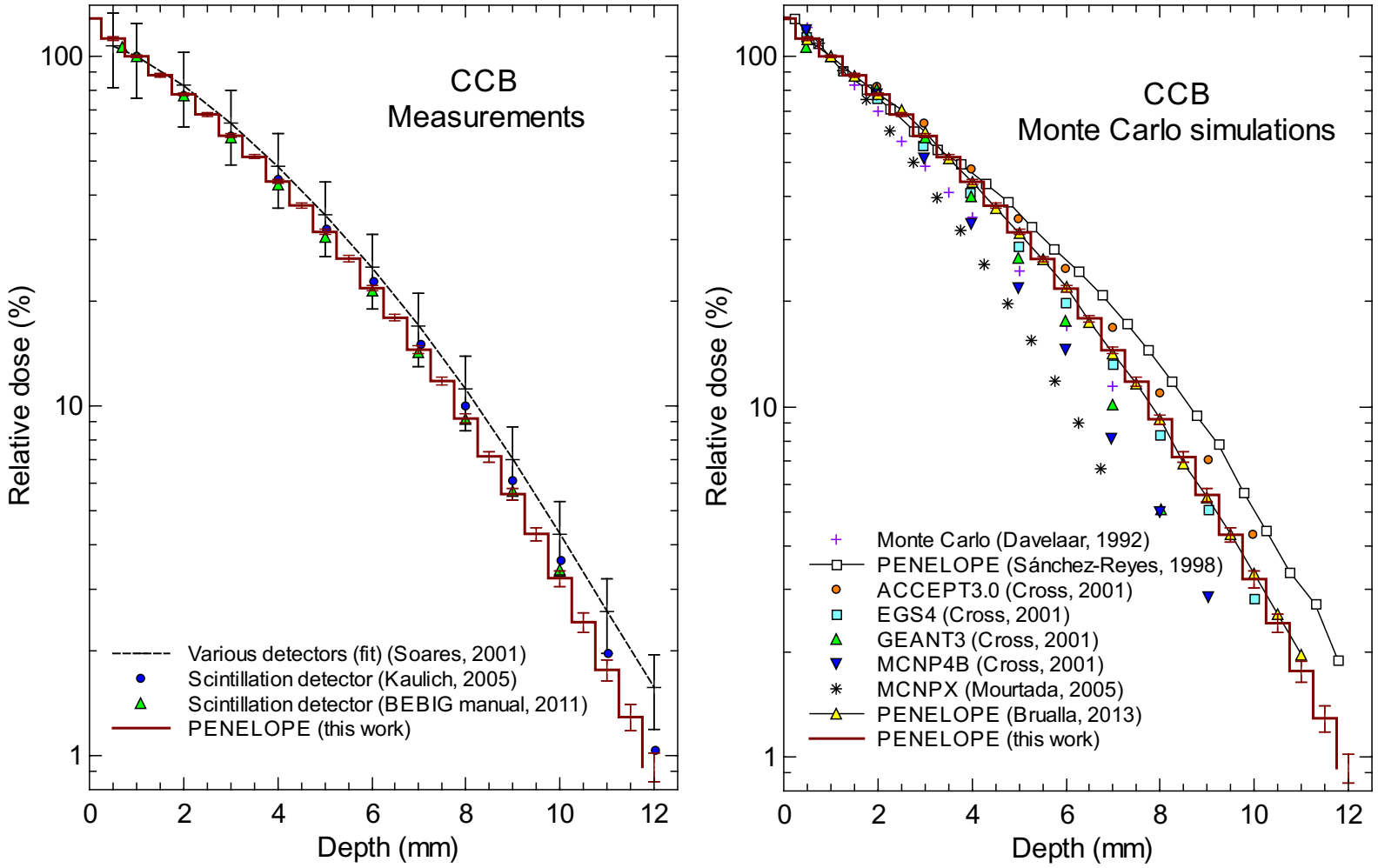

FIGURE 2.15: (LEFT) Relative depth–dose distribution obtained in this work compared with the published experimental data for the CCB plaque. There is good agreement with the experimental values measured using scintillator detectors (Kaulich et al., 2005) and with the manufacturer's reference data. (RIGHT) Comparison with other simulation results provided in the literature. The present results are in excellent agreement with those of Brualla et al. (2013) (within the statistical uncertainty), which were also estimated using the PENELOPE code. Uncertainty bars of PENELOPE data from this work represent the statistical uncertainty with $k = 3$.

2.3.11 Influence of the ^{106}Pd gamma spectrum

Both ^{106}Ru and ^{106}Rh are pure beta emitters, that is, only beta particles are emitted when ^{106}Ru and ^{106}Rh nuclei decay. ^{106}Ru decays to the ground state of ^{106}Rh. ^{106}Rh nuclei decay with a certain probability to excited states of ^{106}Pd, which in turn deexcite emitting gamma rays of discrete energy values (Defrenne and Negret, 2008). This gamma spectrum has been neglected in all published studies on Monte Carlo simulation of ^{106}Ru/^{106}Rh plaques, as it was considered that its influence on the dose distributions was negligible. The previous simulations in this chapter were performed also under this assumption to allow a comparison with previous publications. This assumption, however, is an approximation that may bias the simulation results and it was not justified quantitatively in any publication. Hence, a simulation study is presented in this section to assess the influence of gamma rays from the ^{106}Pd deexcitation on the simulation of ^{106}Ru/^{106}Rh plaques.

The gamma energies were taken from Defrenne and Negret (2008). The gamma components considered were those with energies above 10 keV and emission probabilities per disintegration above 0.1% (Table 2.6). Apart from minor rounding differences, those are the same energy values reported in the ICRU Report 72 (ICRU, 2004).

TABLE 2.6: Energy values and emission probabilities per disintegration of the gamma components from the ^{106}Pd transitions to the ground state included in the simulations (those with $E_\gamma > 10$ keV and emission probability above 0.1%). Taken from Defrenne and Negret (2008).

E_γ (keV)	511.86	616.22	621.93	873.49	1050.41	1128.07	1562.25
Emission probability per disintegration (%)	20.0	0.75	9.93	0.439	1.56	0.404	0.163

To be consistent with the previous simulations of the chapter, the simulations from this section were run with the same simulation parameters. Hence, to obtain low statistical uncertainties at distances far from the plaque, an extremely long simulation time would result (about 4–5 months using a single computing core). To overcome this unpractical computing time a different approach was designed. The simulations from this section were run with version 2014 of PENELOPE (Salvat, 2015a). To ensure that the change of version did not introduce a bias in the results, the previous simulations for the plaques studied in this section were rerun with PENELOPE 2014, confirming that the results were unaltered. PENELOPE 2014 includes a software tool, named `penmain-sum`, to combine the results of independent runs of the same simulation problem allowing to use multiple computing cores simultaneously. Thus, the efficiency of the simulation increases linearly with the available number of cores. Forty cores were used to run each simulation in this section, reducing the simulation time to about 3 or 4 days per plaque, instead of about 4–5 months using a single core. Each independent run produces a file with the partial results of the simulation with accumulated statistics (*dump file*). The tool `penmain-sum` combines all dump files to get the final results of the simulation.

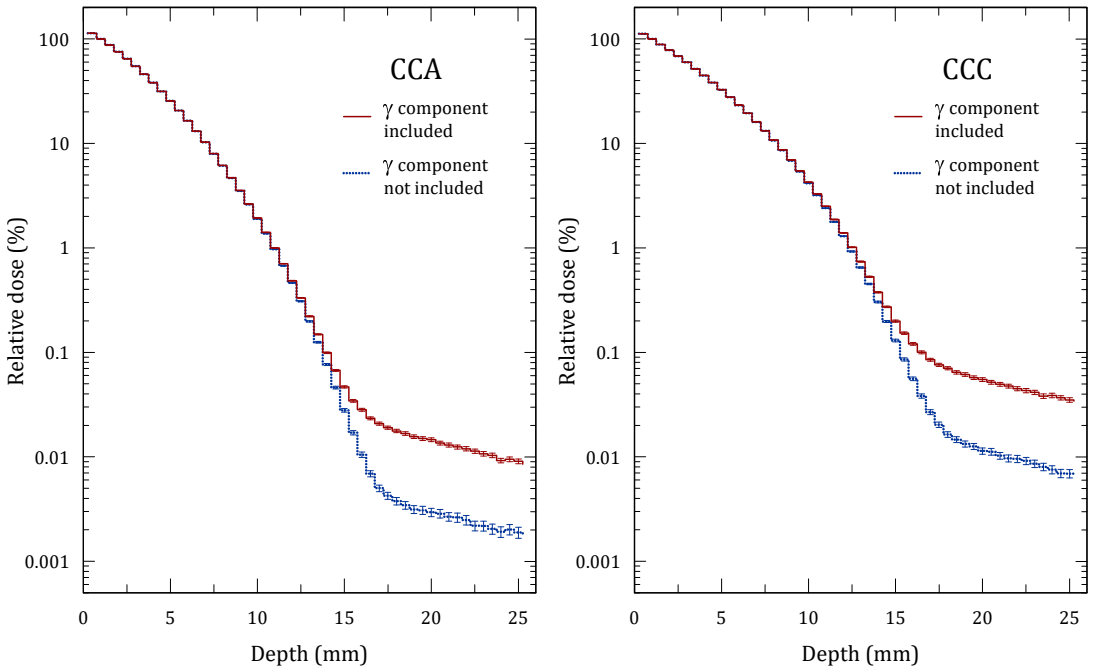

FIGURE 2.16: Percentage depth–dose curves for the plaques CCA and CCC, showing the effect of including in the simulations the gamma components produced by the transitions to the ground state of ^{106}Pd. Uncertainty bars represent the statistical uncertainty with $k = 3$.

The process of manually generating the simulation files needed for multiple independent runs is tedious, error–prone, and takes some time. To manage this situation efficiently, a software tool was developed in this thesis consisting of a set of scripts written in MATLAB (The MathWorks, Inc., Natick, MA, USA) which automate the process. Briefly, the scripts take care of (i) creating the files needed for an arbitrary number of independent runs of the same simulation problem; (ii) launching a number of independent simulation runs simultaneously; and (iii) preparing the dump files to be combined with `penmain-sum` to obtain the final results of the simulation. This software tool was named MUSIMAN (MUltiple SImulations MANagement). The MATLAB source files and additional files of the MUSIMAN package are available at the GitHub repository: `https://github.com/marcelinohermida/MUSIMAN`.

Figure 2.16 shows the percentage depth–dose curves for the plaques CCA and CCC, showing the effect of including in the simulations the gamma components of ^{106}Pd. The contribution of ^{106}Pd gamma rays on the depth–dose curve is negligible at depths of clinical interest, as it was assumed in the literature. The dose at distances about 24 mm from the surface of the plaque is nearly 5 times greater when the gamma contribution is taken into account. At those distances from the plaque, the dose is about 0.01%–0.1% of the dose at a depth of 1 mm. Thus, those differences are not relevant for the clinical practice. However, for simulations involving large distances from the plaques, such as for radiation shielding assessment and estimation of dose received by personnel, this gamma contribution must be considered.

2.3.12 Uncertainty analysis

The result of a calculation or a measurement is only meaningful if a quantitative statement of its uncertainty is given. It is recommended to represent each component of the uncertainty by an estimated standard deviation, named *standard uncertainty*. According to the method used, the estimation of the uncertainty is classified as type A or type B (Bureau International des Poids et Mesures, 2008):

- Type A evaluations of standard uncertainty: those which are evaluated by statistical analysis of a series of repeated observations in the same conditions. For brevity, we will refer to these uncertainties as type A uncertainties.
- Type B evaluations of standard uncertainty: those which are evaluated by other means rather than statistical methods, evaluating all the information available, such as knowledge on the performance of the equipment involved, specifications from the manufacturer, uncertainty values taken from available publications, etc. For brevity, we will refer to these uncertainties as type B uncertainties.

The *combined standard uncertainty* of a result is assumed to represent the estimated standard deviation of the result. It is obtained by combining the standard uncertainties from type A and type B evaluations using the law of propagation of the uncertainty, that is, computing the square root of the sum of the squares of each uncertainty contribution.

The results of Monte Carlo simulations are affected by both statistical (type A) and non–statistical (type B) sources of uncertainty. The statistical uncertainty[10] depends on the number (N) of simulated histories as $1/\sqrt{N}$. The number of histories in the simulations from this chapter was large enough to ensure that the maximum value for the standard statistical uncertainty of the estimated dose distributions was below 0.7%, and typically about 0.3%.

The two main sources of non–statistical uncertainty are:

- The approximation that the radioisotope is homogeneously distributed on the active surface, although the actual distribution can vary greatly among plaques of the same model. As an example, Eichmann et al. (2009) reported hot spots in the surface dose rate of a CCB plaque of up to 18% respect to the dose at the center of the plaque. The purpose of this thesis is providing data representative of each plaque model. Hence, to consider the real radioisotope distribution of specific plaques goes beyond the objectives set.
- The modeling of the transport of radiation in PENELOPE, which includes uncertainties due to the differential cross section data and to approximations in the transport and material algorithms. The influence of those uncertainties in the tallied quantities have never been systematically assessed. The physical models and interaction data included in PENELOPE are the most accurate available up to date (Salvat, 2015b).

[10] The term *statistical uncertainty*, although not formally defined by the Bureau International des Poids et Mesures (2008), is of common use in the field of Monte Carlo simulation of radiation transport, and therefore is also used throughout this thesis.

Other sources of non–statistical uncertainty, whose contribution has been evaluated in the thesis, include:

- The assumption that the silver exit window has a nominal thickness (100 μm), although thickness variations of approximately 6 μm have been reported (Eichmann et al., 2009). Simulations varying the exit window thickness in ±10 μm gave results compatible with those obtained using the nominal thickness, within a standard statistical uncertainty of 0.3%.

- The modeling of the active layer as a mathematical surface. The thickness of the active layer is only ∼0.1 μm. The previous item showed that variations up to ±10 μm in the exit window thickness did not affect the simulation results. Thus, to assume an active layer of zero thickness will not affect the results either.

- The lack of gamma contributions from ^{106}Pd in the spectrum used as source for the simulations. The results from section 2.3.11 confirmed that the effect of the gamma components is negligible at depths of clinical interest, as it was assumed in the literature. However, for other purposes such as shielding design or radiation protection of the staff, the ^{106}Pd gamma contributions should be included in the simulations.

These latter sources of uncertainty contribute to the overall uncertainty less than the attained statistical uncertainty of the simulations.

An indication of the overall uncertainty can be obtained by comparing the Monte Carlo estimations with experimental results (ICRU, 2004). The depth–dose data estimated in this work agree with most experimental data within 3% for all plaques. This value is consistent with the ICRU Report 72 (ICRU, 2004) estimate of an overall standard uncertainty of approximately 3–4% for the Monte Carlo dose estimations for beta–ray sources.

Chapter 3

Absorbed–dose energy dependence of the EBT3 radiochromic film

3.1 Introduction

The EBT3 radiochromic film model is the most recent model produced by Ashland for radiotherapy applications. It is widely used for quality assurance in external beam radiotherapy and brachytherapy. One frequently stated advantage of radiochromic films is an energy dependence lower than that of the conventional radiographic films but the published results are somewhat conflicting for photon energies below about 100 keV (Chiu-Tsao et al., 2005; Butson et al., 2006; Rink et al., 2007; Sutherland and Rogers, 2010; Butson et al., 2010; Villarreal-Barajas and Khan, 2014; Bekerat et al., 2014). The changes in the formulation of the active layers may partially explain the discrepancy in the results of the energy dependence shown in previous publications. At least three formulations for the active layer of the EBT3 film are described in the literature, corresponding to different lots delivered under the same commercial denomination (Bekerat et al., 2014).

This chapter analyzes the energy dependence of the EBT3 radiochromic film with the latest formulation through Monte Carlo simulations. The influence of the phantom material in which the film is immersed during the irradiation is studied for a wide range of photon energies. This topic has not been assessed in the literature. Several solid phantom materials commonly used for film dosimetry are compared to water, the reference medium for radiation dosimetry. These results will be used to assess a component of the experimental uncertainty of the measurements presented in chapter 4. Moreover, the results have a wider scope, as the EBT3 model is the current *de facto* standard for film dosimetry in radiotherapy and other fields. The contents of this chapter were published by the author of this thesis and coauthors in the *Medical Physics* journal (Hermida-López et al., 2014).

The general term *beam quality* refers to the energy distribution of a radiation beam, and it is related to the penetrability of the beam in a material medium. In the case of monoenergetic beams, the beam quality is established by the beam energy. For polyenergetic beams, the beam quality relates to an index such as the beam mean energy, or the $TPR_{20,10}$ (IAEA, 2001). In what follows, to be consistent with previous publications (Sutherland and Rogers, 2010;

Bekerat et al., 2014), we adopt the notation and terminology introduced by Rogers (2009) to describe the characteristics of radiation dosimeters.

The energy dependence of a detector with the beam quality Q can be divided into two components (Rogers, 2009): (1) the intrinsic energy dependence $k_{\mathrm{bq}}(\mathrm{Q})$ with the beam quality Q, which relates the dose absorbed in the sensitive component of the detector, $D_{\mathrm{det}}(\mathrm{Q})$, with the detector reading $M_{\mathrm{det}}(\mathrm{Q})$:

$$D_{\mathrm{det}}(\mathrm{Q}) = k_{\mathrm{bq}}(\mathrm{Q})\, M_{\mathrm{det}}(\mathrm{Q}), \tag{3.1}$$

and (2) the absorbed–dose energy dependence $f(\mathrm{Q})$, which relates the dose absorbed in the medium in the absence of the detector, $D_{\mathrm{med}}(\mathrm{Q})$, with the dose absorbed in the sensitive material of the detector $D_{\mathrm{det}}(\mathrm{Q})$:

$$D_{\mathrm{med}}(\mathrm{Q}) = f(\mathrm{Q})\, D_{\mathrm{det}}(\mathrm{Q}). \tag{3.2}$$

Another quantity of interest is the so–called absorbed–dose sensitivity, $S_{\mathrm{AD,med}}(\mathrm{Q})$, defined as the detector reading per unit of absorbed–dose to the medium estimated at the position of the detector and in its absence, and as a function of the beam quality Q. For a radiochromic film we can, for the purpose of this work, approximate the detector reading at beam quality Q as the net optical density of the film, $M_{\mathrm{det}}(\mathrm{Q}) \equiv \Delta\mathrm{OD}_{\mathrm{det}}(\mathrm{Q})$. The net optical density is defined as the optical density change of irradiated films due only to radiation; corrections are made for background optical density with a non–irradiated control piece of film. Then the absorbed–dose sensitivity of a radiochromic film (or, less formally, the overall energy response), which is a measurable quantity, can be expressed as follows:

$$S_{\mathrm{AD,med}}(\mathrm{Q}) = \frac{\Delta\mathrm{OD}_{\mathrm{det}}(\mathrm{Q})}{D_{\mathrm{med}}(\mathrm{Q})} = \frac{1}{f(\mathrm{Q})\, k_{\mathrm{bq}}(\mathrm{Q})}. \tag{3.3}$$

The absorbed–dose energy dependence $f(\mathrm{Q})$ can be calculated through a Monte Carlo simulation of radiation transport as, by definition, it only depends on the absorbed dose distribution in the medium and in the active layers of the film. To this purpose, an accurate description of the geometry and material composition of the film layers is needed. The intrinsic energy dependence $k_{\mathrm{bq}}(\mathrm{Q})$ is affected by chemical reactions on the film active layer and by the film post–irradiation handling (scanner used, time delay between irradiation and scanning, temperature of film storage, etc.), which are not modeled within the Monte Carlo simulation of radiation transport. Notwithstanding, it can be be evaluated using equation (3.3) by measuring the energy response of the film, $S_{\mathrm{AD,med}}(\mathrm{Q})$, and then using Monte Carlo simulations to calculate the absorbed-dose energy dependence $f(\mathrm{Q})$.

Although water is the reference medium for radiation therapy dosimetry, for film dosimetry it is more practical to use a solid phantom in some experimental situations, such as in the calibration of films with a clinical electron linear accelerator. Since the composition of solid phantoms differs from that of water, the energy response of the film may also differ.

The definition of the absorbed-dose energy dependence $f(\mathrm{Q})$ considers the absorbed dose to the medium and the absorbed dose to the active element of the detector. If, instead of considering the dose to the medium, we consider the quantity dose-to-water in the medium, which is the common practice in radiation dosimetry, we could define a new quantity as the 'absorbed-dose-to-water energy dependence'. Let us denote this quantity as:

$$g(\mathrm{Q}) \equiv \frac{D_{\mathrm{w,med}}(\mathrm{Q})}{D_{\mathrm{det}}(\mathrm{Q})}, \tag{3.4}$$

where $D_{\mathrm{w,med}}(\mathrm{Q})$ is the dose to a thin layer of water inside the medium, and $D_{\mathrm{det}}(\mathrm{Q})$ is the dose to the active element of the detector. We calculated this absorbed-dose-to-water energy dependence, $g(\mathrm{Q})$, for the phantom materials studied.

The Monte Carlo simulation work described in this chapter aims to study the influence of plastic phantom materials respect to water on the absorbed-dose energy dependence of the EBT3 radiochromic film, for photons in the energy range from 3 keV to 18 MeV. In addition to monoenergetic photon beams, some theoretical X-ray spectra are used. To validate our choice of simulation parameters, we also calculate $f(\mathrm{Q})$ for older film models, EBT and EBT2, comparing with published results (Sutherland and Rogers, 2010).

Only photons were included in this study as it was already established that the radiochromic films behave very similarly with electrons and photons (Sorriaux et al., 2013; Sipilä et al., 2016).

3.2 Materials and methods

3.2.1 Radiochromic films and phantom materials

Figure 3.1 shows the layer structure of the radiochromic films studied in this chapter. The EBT model has a symmetric 5–layer structure with two active layers 17 μm thick. The EBT2 model has an asymmetric structure with 5 layers, and only one active layer 30 μm thick to increase sensitivity. The EBT3 film model is symmetric, with a single 30 μm thick active layer sandwiched between two 125 μm polyester layers treated with microscopic silica particles to avoid Newton rings. The silica particles were not included in the simulation as their effect on the dose deposition is negligible (Bekerat et al., 2014). Table 3.1 shows the elemental composition by mass percent of the films simulated in this work. It should be emphasized that the formulation for the EBT2 film shown on Table 3.1 is no longer produced, as well as the EBT film. These discontinued formulations were used in our study for validation purposes of the simulation setup allowing comparison with published data (Sutherland and Rogers, 2010). The formulation shown in Table 3.1 for the EBT3 film was the most recent at the time of writing.

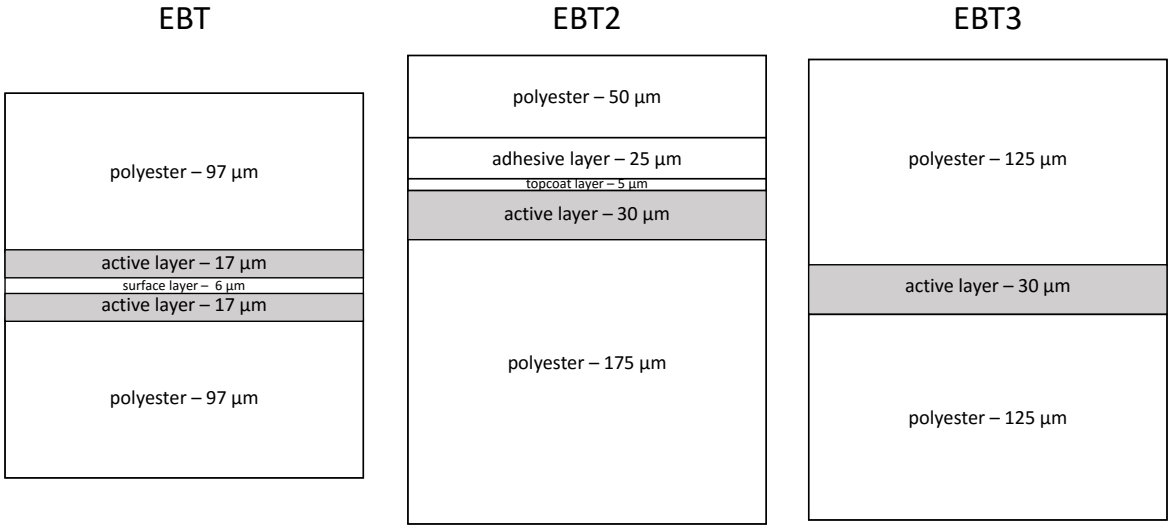

FIGURE 3.1: Layer structure to scale of EBT, EBT2, and EBT3 films.

TABLE 3.1: Atomic composition by mass percent of the EBT [Sutherland and Rogers (2010)], EBT2 [Sutherland and Rogers (2010)], and EBT3 (Ref: manufacturer, private communication) films studied in this work. The composition of the active layers for the EBT2 and the EBT3 has not changed since Oct. 2012 (Bekerat et al., 2014).

Layer	Atomic composition by mass percent											ρ (g/cm^3)	Formulation date
	C	H	O	N	Li	Cl	K	Br	Na	S	Al		
						EBT							Before 2009
Active	57.4	9.4	16.4	13.2	0.8	2.9	-	-	-	-	-	1.10	
Surface	32.3	6.5	20.5	21.6	2.3	16.8	-	-	-	-	-	1.20	
Polyester	62.5	4.2	33.3	-	-	-	-	-	-	-	-	1.35	
						EBT2							Feb. 2009
Active (lot #020609)	57.8	9.6	27.8	0.2	0.9	1.7	0.6	1.3	-	-	-	1.20	
Adhesive	65.6	9.4	24.9	-	-	-	-	-	-	-	-	1.20	
Topcoat	47.2	8.8	38.2	-	1.0	4.9	-	-	-	-	-	1.20	
Polyester	62.5	4.2	33.3	-	-	-	-	-	-	-	-	1.35	
						EBT3							Dec. 2013
Active	57.2	8.6	25.7	0.8	0.6	0.5	-	-	0.4	0.3	5.8	1.35	
Polyester	62.5	4.2	33.3	-	-	-	-	-	-	-	-	1.35	

We tested solid phantom materials commonly used for film dosimetry in the kV and MV energy range: RW1 and RW3 (PTW-Freiburg, Freiburg, Germany), Solid Water (Gammex-RMI, Madison, WI, USA) and polymethylmethacrylate (PMMA). Table 3.2 shows the corresponding composition data.

TABLE 3.2: Atomic composition by mass percent of the phantom materials studied in this work. The water density is stated at 20°C and 101.3 kPa.

	Water	**RW1**	**RW3**	**Solid Water**	**PMMA**
C	-	79.4	90.4	67.2	59.98
H	11.2	13.2	7.6	8.1	8.05
O	88.8	3.8	0.8	19.9	31.96
N	-	-	-	2.4	-
Ti	-	-	1.2	-	-
Mg	-	0.9	-	-	-
Cl	-	2.7	-	0.1	-
Ca	-	-	-	2.3	-
ρ (g/cm^3)	0.998	0.970	1.045	1.036	1.190
Z_{eff}	7.42	7.14	-	7.38	6.47
Ref.	Sutherland and Rogers (2010)	ICRU (1989)	Hill et al. (2008)	ICRU (1989)	Hubbell and Seltzer (1996)

3.2.2 Simulation setup and PENELOPE simulation parameters

Simulations were run with PENELOPE 2011 (Baró et al., 1995; Salvat et al., 2011) using the main program PENEASY (Sempau et al., 2011) (version 2012-06-01). The geometrical model consisted of a cylindrical phantom with a radius of 20 cm and a thickness of 30 cm (Sutherland and Rogers, 2010). Depending on the initial photon energy the film was positioned at different depths taken from the work of Sutherland and Rogers (2010): (i) film laying over the surface of the phantom for $E \leq 10$ keV; (ii) with the upstream surface of the film at a depth of 1 cm into the phantom for 10 keV $< E \leq$ 1.25 MeV; and (iii) with the upstream surface of the film at a depth of 5 cm for E$>$ 1.25 MeV.

Although the film extended over the entire radius of the cylinder, the dose scoring volume consisted of the active layer of the film within a radius of 3 cm. In the simulations run to evaluate the dose to the phantom, $D_{\text{med}}(\text{Q})$, all film layers were replaced with the phantom material, while the scoring volumes remained the same. In the simulations run to evaluate the dose-to-water in the phantom, $D_{\text{w,med}}(\text{Q})$, all film layers were replaced with the phantom material except the active layer which was replaced with water. The scoring volumes remained the same.

We simulated monoenergetic parallel photon beams of 5 cm in diameter with energies in the range 3 keV–18 MeV, and X-ray beams from an RT 100 superficial therapy system (C. H. F. Müller; now Philips GmbH, Hamburg, Germany). The approximate X-ray spectra produced by the RT 100 tube were modeled with the software *SpekCalc* (version 1.1) (Poludniowski et al., 2009) which estimates the spectra emitted from tungsten anode X-ray tubes combining an analytical approach to model Bremsstrahlung production with Monte Carlo estimated

target electron distributions. The simulated beams from the RT 100 had the following peak kilovoltages [mean energies]: 30 kVp [17.6 keV], 45 kVp [24.3 keV], 55 kVp [28.5 keV], 85 kVp [39.2 keV] and 100 kVp [45.0 keV]. The mean energies of the simulated beams were calculated also with *SpekCalc*.

To validate our geometric and material model and to assess the adequacy of the chosen PENELOPE simulation parameters we calculated $f(\mathrm{Q})$ for the EBT and EBT2 film models, comparing our results with those obtained by Sutherland and Rogers (2010) using the EGSnrc Monte Carlo code (Kawrakow et al., 2009).

Simulation transport parameters were adjusted to obtain a nearly detailed simulation in relevant regions and materials, such as the film layers and the phantom layers closer to the film, while the transport parameters employed in the phantom volume far from the film produce a simulation that deviates from a detailed one, to increase its efficiency in that region. More precisely, for the film layers and the phantom layer above the film we set C1 = C2 = 0.02. For the phantom layer downstream from the film up to 10 cm depth we set C1 = C2 = 0.1, and for the phantom layer deeper than 10 cm we set C1 = C2 = 0.15. WCC and WCR were set to 1 keV for all the simulation materials and DSMAX was set to one tenth of the thickness of each layer, following recommendations from the PENELOPE manual (Salvat et al., 2011). For some test cases we verified that the results obtained with the chosen simulation parameters were statistically compatible to those obtained using detailed simulations. In this manner, we reduced the calculation time without compromising the accuracy of the results. For electrons and positrons the absorption energies in the film layers were set to 0.1 keV for initial energies below 3 MeV, and to 1 keV for higher energies. For photons the absorption energies in the film layers were set to 0.1 keV. The standard statistical uncertainty attained was below 0.7% for 75% of the calculated values and never exceeded 1.4%. All statistical uncertainties in this chapter are reported to one standard deviation.

3.3 Results and discussion

3.3.1 Validation of simulation parameters: $f(\mathrm{Q})$ for the EBT and EBT2 films

Our calculated $f(\mathrm{Q})$ values for the EBT and EBT2 films agree within 2% with published data (Sutherland and Rogers, 2010) calculated with the EGSnrc Monte Carlo code (Figure 3.2), except for some data points at photon energies around 10 keV for the EBT2 film. To verify if the different absorption energies used in our work (0.1 keV) and those used in the Sutherland and Rogers paper (1 keV) could be the cause of the discrepancies at energies lower than 10 keV, we ran additional simulations with an absorption energy of 1 keV. We found that the differences in $f(\mathrm{Q})$ were within the statistical uncertainty (below 0.8%). So, the different absorption energies cannot explain the differences found between our work and the work by Sutherland and Rogers (2010) for the EBT2 film at low energies. As the EBT2 film has an asymmetric layer structure, we also studied if the orientation of the film had some influence in the absorbed-dose energy dependence in water. We ran simulations with the film upside down

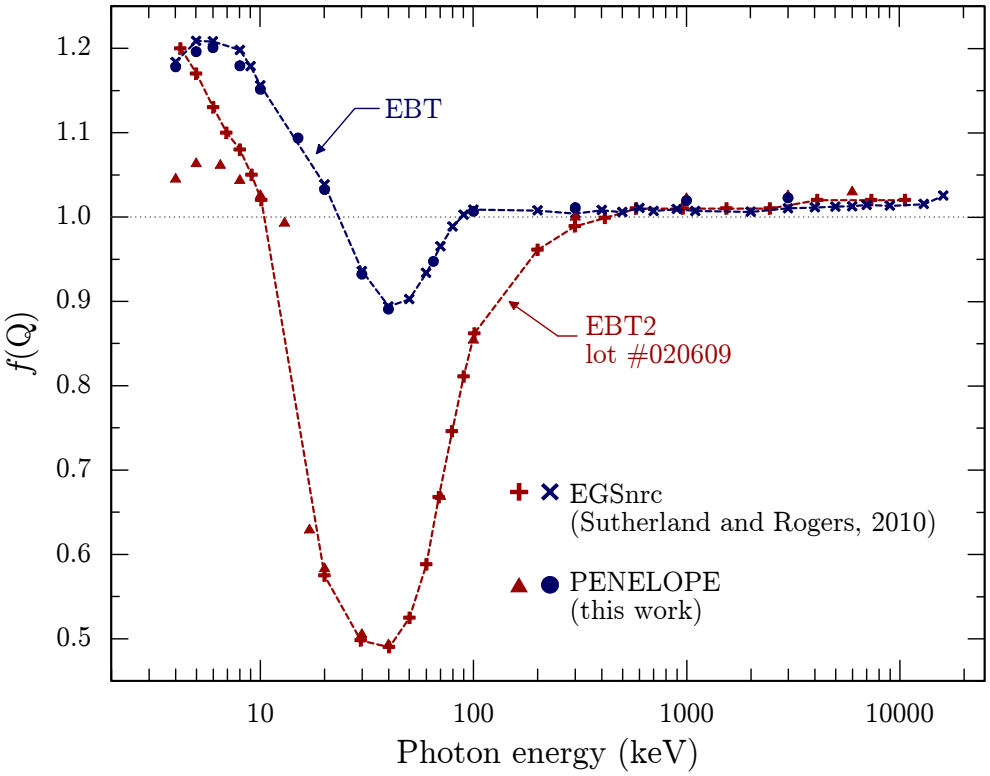

FIGURE 3.2: Calculated absorbed-dose energy dependence $f(Q)$ in water for EBT and EBT2 (lot #020609) films compared to Sutherland and Rogers (2010) results. Lines are a visual aid to connect data points from the work of Sutherland and Rogers. For clarity, the data points from this work are not connected with lines. The standard statistical uncertainty bars are smaller than the symbols size.

and the difference in $f(Q)$ found between both orientations was within the standard statistical uncertainty reached, below 1%, except for the lowest simulated energy (5 keV), where the difference was of -3.5%.

3.3.2 Absorbed-dose-to-water energy dependence $g(Q)$ of EBT3 film: influence of the phantom material

Figure 3.3 shows the calculated $g(Q)$ for the EBT3 film for the phantom materials used. In the photon energy range from 10 keV to 18 MeV, the $f(Q)$ for water was constant within 2.3%, with a standard statistical uncertainty less than 1%. This result represents an improvement of EBT3 film with respect to the older EBT2 film which showed a marked energy dependence (Figure 3.2). If we consider the quantity dose-to-water in the phantom, then the difference in energy dependence for the solid phantoms with respect to water is within 6% for energies above 10 keV. The $g(Q)$ values obtained for the mean energies of the X-ray beams tested are very similar, as expected, to the values found for the corresponding monoenergetic beams, with differences below 2% for Solid Water, RW1, RW3, and PMMA and below 0.7% for water.

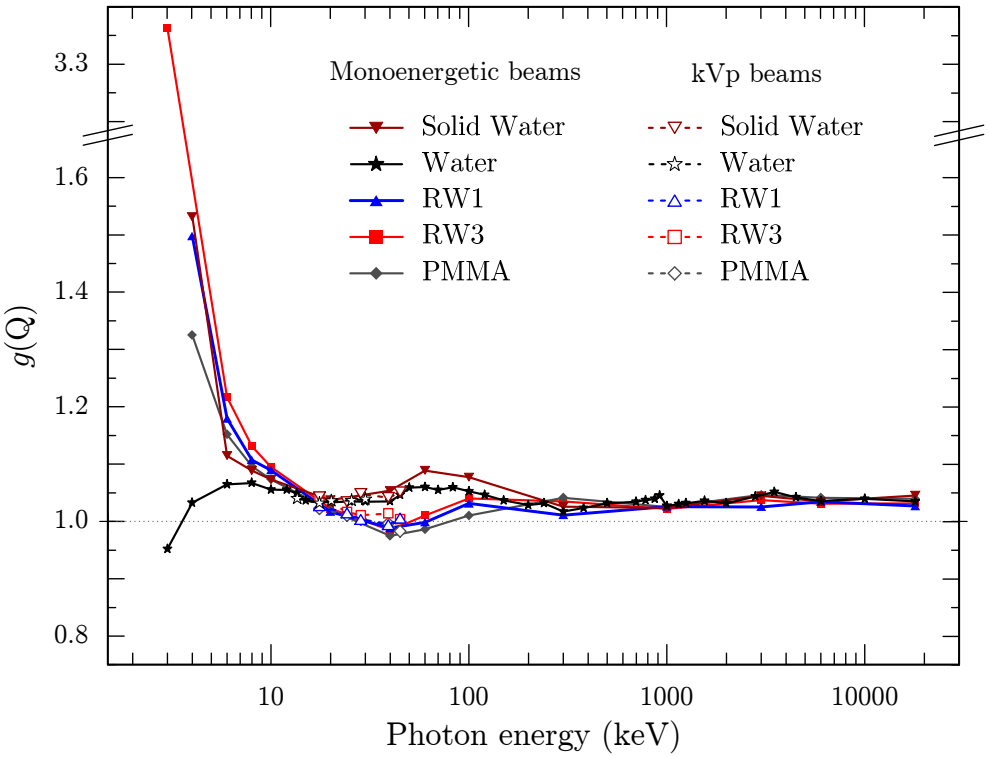

FIGURE 3.3: Calculated EBT3 film absorbed-dose-to-water energy dependence $g(Q)$ as a function of the phantom material used, when considering the quantity dose-to-water in the phantom material. Note that, for water, $g(Q) = f(Q)$, by definition. The X–ray beams (kVp beams) are represented in the graph with their mean energies. The standard statistical uncertainty bars ($k = 1$) are smaller than the symbols size.

3.3.3 Discussion

We calculated the influence of the phantom material in which the film is located on the absorbed dose energy dependence for the EBT3 film, considering the quantity dose-to-water in the phantom, $D_{w,med}(Q)$. As long as we calibrate the film in terms of absorbed-dose-to-water, there is only a small influence of the phantom material on the energy dependence of the film between 10 keV and 200 keV, and practically no influence for energies above 200 keV.

The absorbed-dose energy dependence does not explain all the energy response of the film, as the intrinsic dependence $k_{bq}(Q)$ must also be considered. The intrinsic energy dependence is related to the polymerizing efficiency in the active layers of the film, but it also depends on the post-irradiation handling of the film. Figure 3.4 shows, for the EBT3 film in water, the measured overall energy dependence $S^{-1}_{AD,w}(Q)$ taken from Figure 12 of Bekerat et al. (2014), the absorbed-dose energy dependence $f(Q)$ calculated in this work, and the intrinsic energy dependence $k_{bq}(Q)$ derived using equation (3.3).

We used the latest formulation of the EBT3 film available from the manufacturer in December 2013, with 5.8% Al (see Table 3.1). Bekerat et al. (2014) stated that the studied film contained 7% Al, but they did not state the complete atomic composition. We made additional

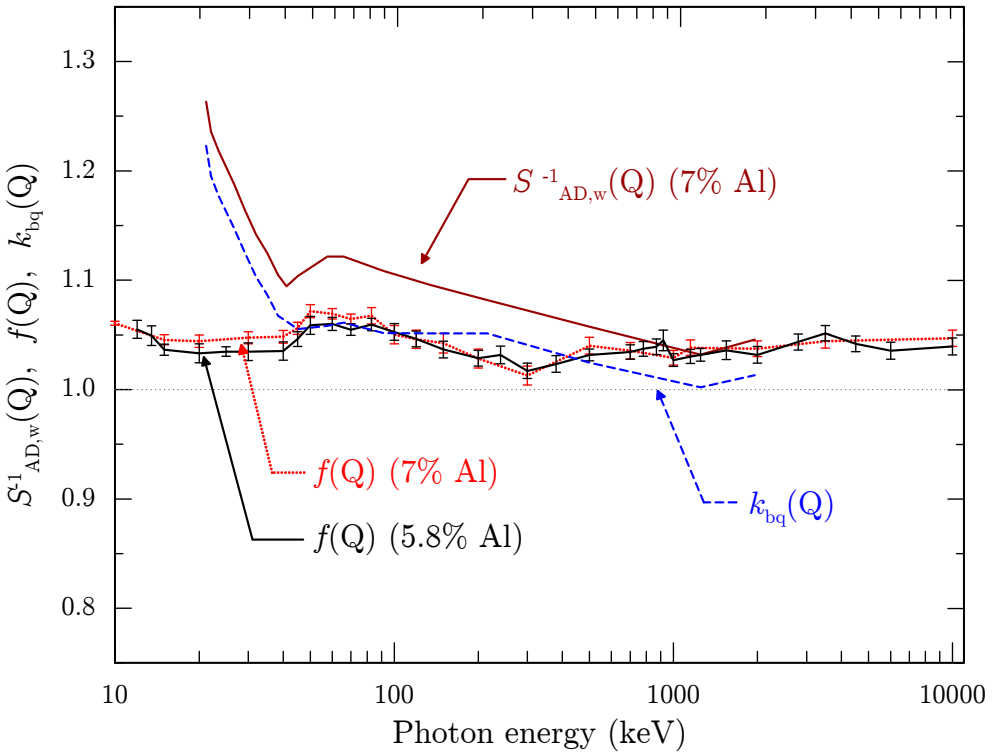

FIGURE 3.4: EBT3 film energy dependence in water: overall energy response $S^{-1}_{AD,w}(Q)$ measured by Bekerat et al. (2014), absorbed-dose energy dependence $f(Q)$ calculated with PENELOPE in this work (using 5.8% and 7% aluminum content), and intrinsic energy dependence $k_{bq}(Q)$ derived from equation (3.3). The uncertainty bars represent the standard statistical uncertainty.

simulations considering an EBT3 film with 7% Al and assuming that the other components of the formulation were reduced proportionally. This means that the 7% Al composition used in this work is not necessarily the same as the 7% Al composition from Bekerat et al. (2014). The standard statistical uncertainty of the results was below 1%. Both curves for the $f(Q)$ (5.8% Al and 7% Al) are compatible, confirming that the small difference in aluminum content between both formulations has a negligible effect on $f(Q)$ at the statistical uncertainty reached.

The comparison of the results of the simulation of monoenergetic beams with measurements obtained with polyenergetic spectra is an approximation. Within this approximation, the reported overall energy response in water of the EBT3 film at low energies turns out to be mainly due to the intrinsic energy dependence.

The EBT3 film shows a reasonably constant absorbed-dose energy dependence when irradiated in water. If we consider the quantity dose-to-water in the phantom, the maximum difference of EBT3 energy dependence with the solid phantoms studied respect to water is about 6%, found at an energy of 50 keV. Moreover, the reported overall energy dependence of the EBT3 film in water at energies below 100 keV is mainly due to the intrinsic energy dependence.

Chapter 4

Measurement of absorbed dose distributions from ^{106}Ru/^{106}Rh plaques with the EBT3 radiochromic film

4.1 Introduction

This chapter presents a practical method developed in this thesis for measuring in water the 2D absorbed dose distributions and the absolute dose rates produced by ^{106}Ru/^{106}Rh ophthalmic plaques. Two plaques of the CCX model (CCX 228 and CCX 250) and one plaque of the CCA model (CCA 1440) were studied, whose physical dosimetry was analyzed in chapter 2. The measurements were made using the EBT3 radiochromic film studied in chapter 3. Two experimental setups were developed to measure the dose distributions with the film and the plaque immersed in water: one to measure the 2D dose distribution at the plane Z=5 mm, perpendicular to the symmetry axis of the plaque, and another to measure the 2D dose distribution in the XZ plane (PDD plane). The main advantage of measuring in water is avoiding the conversion from dose–to–plastic to dose–to–water and the associated uncertainties. At the time of this writing all reported measurements of ^{106}Ru/^{106}Rh plaques with radiochromic film were done using plastic phantoms (ICRU, 2004; Soares et al., 2001; Taccini et al., 1997; Heilemann et al., 2015). Another advantage of the experimental method presented in this chapter is that it uses equipment and tools easily available at any medical physics department from a hospital with external beam radiotherapy facilities.

The following sections explain the experimental setups, film calibration and processing, analysis of the results, and comparison to the Monte Carlo simulation results shown in chapter 2, and with the available results in the literature.

4.2 Materials and methods

4.2.1 Experimental setups

A mold was made for each plaque model to obtain a positioning of the plaque as accurate as possible. Using dummy plaques (plaques with the same geometrical dimensions as the

FIGURE 4.1: Mold made with polymer clay using the dummy plaque (indicated by the small hole) of the CCX model.

clinical plaques, but with no radioisotope layer), the molds were made (Figure 4.1) with a commercially available polymer clay (Sculpey, Polyform Products Company, USA). It has a texture similar to plasteline, and it is hardened in a conventional oven during 15 min at 130°.

Setup for measurements at a plane perpendicular to the symmetry axis

Figure 4.2 shows the setup used to measure the dose distribution at a plane perpendicular to the symmetry axis of the plaque. The measurements were done at 5 mm from the intersection point of the symmetry axis and the inner surface of the plaque. From now on, this distance will be referred to as the 'film–plaque distance'. To achieve an easy centering and alignment the setup was mounted on the treatment couch of a radiotherapy linear accelerator to take profit of the zenithal perpendicular laser beams installed on the ceiling of the treatment room. The set of mold–plaque–film was introduced in a small PMMA tank filled with distilled water. The tank was on a leveling support. An auxiliary plastic box filled with water was used to transport the plaque from/to the measurement tank and the handling area, situated behind a 15 mm PMMA shielding. The plaque was handled with tweezers at all times. The pieces of film used for this setup, of about 50×50 mm^2 were cut with the help of a paper template and fixed with paper tape to the top face of a Roos chamber adapter [Figure 4.2(b)], which was found to have adequate dimensions for these measurements.

The mold with the plaque was introduced in the water tank and aligned with the laser beams. Then, a set of PMMA spacers 8.5 mm thick was located on both sides of the mold and on its caudal side [Figure 4.2(d) and (e)]. The Roos adapter with the film was finally set on the spacers, thus being 5 mm the distance from the plaque's surface to the film. In this setup, the final film positioning was achieved in about 10 s, with measuring times from 60 to 120 min. Hence, the contribution of the positioning to the dose uncertainty is below 0.3%. After measuring, the films were removed, dried, labeled and stored in a black envelope until they were scanned.

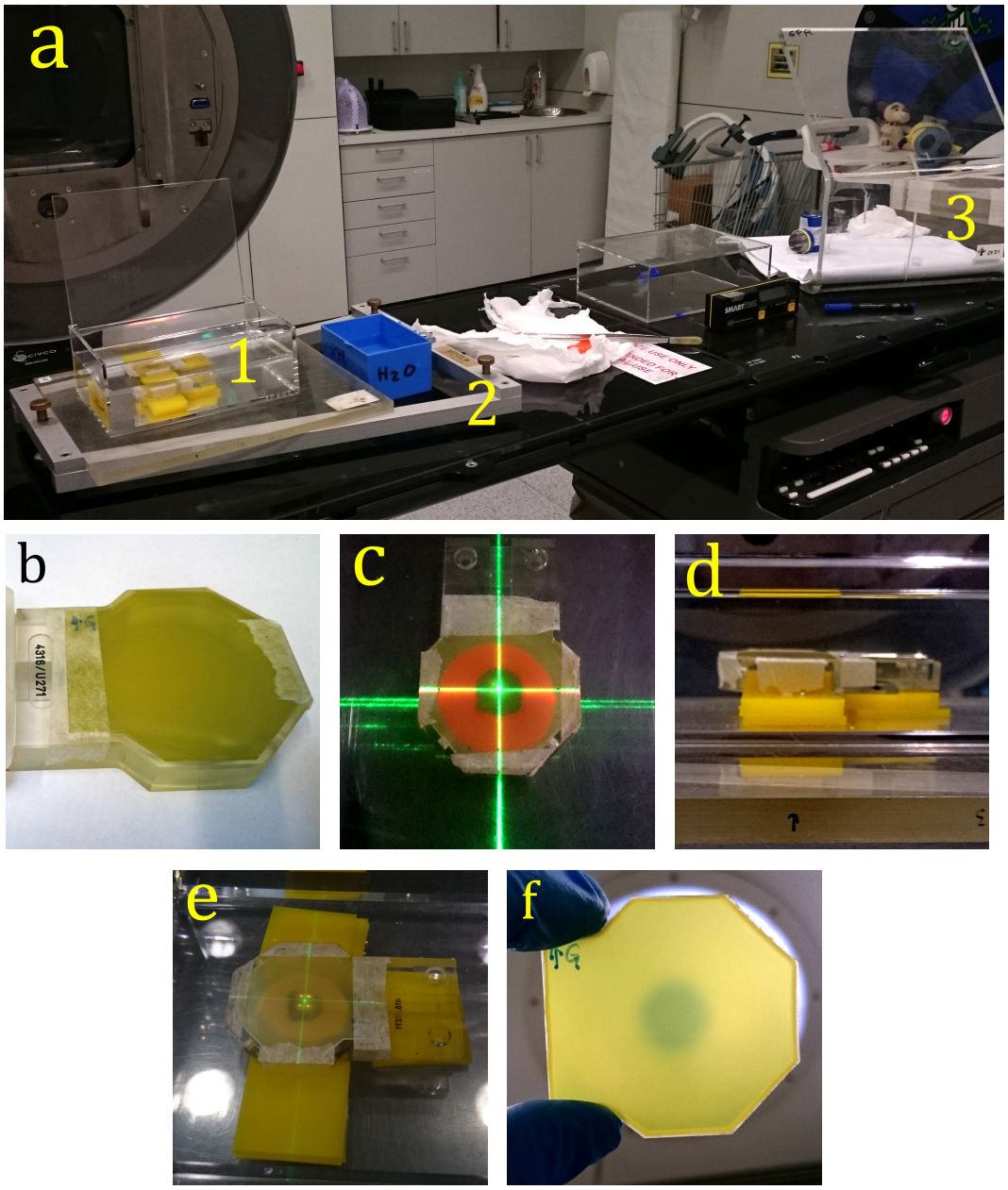

FIGURE 4.2: Experimental setup for measurement of perpendicular dose planes at a film–plaque distance of 5 mm. (a) General view of the setup. 1: Water tank; 2: Leveling platform with circular bubble level included; 3: PMMA shielding for safe handling of the plaque. The blue box, next to the water tank, was filled with water and used for radiation protection purposes, to transport the plaque from/to the measurement tank and the handling area behind the shielding. (b) Film fixed to film support (a Roos chamber adapter). (c) Perpendicular green laser beams installed on the ceiling of the treatment room were used to ensure proper centering and alignment of the plaque (CCA in the picture) and the film. (d) Lateral view of CCX setup, showing the spacers needed to put the film at 5 mm from the surface of the plaque. (e) Detail of the setup for the CCX plaque. Film and plaque alignment checked with the ceiling laser. (f) Sample of film irradiated with this setup. The dark rim (about 2–2.5 mm) near the edge of the film was caused by water penetration, which does not affect the measurement area.

Setup for PDD measurement

Figure 4.3 shows the setup for PDD measurements. A standard water tank (MED–TEC) was used to contain the set of mold–plaque–film immersed in water. Distilled water was used to avoid lime stains on the film due to long measuring times (several hours). A PMMA base was used to support the mold with the plaque. Both the water tank and the PMMA base were leveled before measuring. The mold with the plaque was centered and aligned with the help of a laser level. The pieces of EBT3 film, of about 70×30 mm^2, were cut following the spherical form of the plaque with the help of a paper template. A thin layer of nail polish was applied to the film edges in contact with the plaque to avoid water penetration (Heilemann et al., 2015). With these precautions, only the first 1–1.5 mm from the film edge needed to be discarded from the dosimetric analysis.

The upper part of the film was tightly sandwiched between PMMA plates of $30 \times 30 \times 3$ mm^3. The lateral position of the vertical movement device of the water tank (see Figure 4.3, (a)2), indicated by a scale on the side of the tank, was annotated. The device was then removed from the tank and the sandwiched film was attached to the device with adhesive tape (see Figure 4.3, (a)4, and (b)–(d)). Once the mold with the plaque was correctly centered the device with the attached film was repositioned at the original position in the water tank and the film was vertically moved until the film contacted the inner surface of the plaque. With some practice, this final film positioning can be accurately done in less than a minute, reducing the uncertainty in film dose due to film irradiation during the positioning. As the irradiation time was about 150 min, the uncertainty associated with dose absorbed by the film during positioning is less than 0.7%. At the end of the measurement the films were removed, dried, labeled and stored in a black envelope until they were scanned.

4.2.2 Film calibration and reading

Film calibration and reading was made following the recommendations of the manufacturer and those found in literature (Blackwell et al., 1998; Devic, 2011; Devic et al., 2016). The changes in the film color when irradiated are due to a polymerization process in which needle–like polymers grow preferentially along one direction. Rotation of the irradiated films on the scanner bed can give differences in the measured signal as high as 8% (Devic et al., 2016). Hence, the same orientation of the films was maintained at all steps of the experimental procedure. Films used corresponded to the same lot (#06051403). Films were handled with gloves during film preparation, calibration, measuring and scanning.

For calibration, films were cut into strips of 42×203 mm^2 and irradiated in a 6 MV photon beam from a Clinac 2100 clinical electron linear accelerator (Varian Medical Systems, Palo Alto, CA, USA). The linear accelerator absorbed dose to water in reference conditions was determined according to the International Atomic Energy Agency TRS–398 code of practice (IAEA, 2001). Output calibration was done in a water phantom using a cylindrical ionization chamber type TM30013 and an UNIDOS ^{webline} T10021 electrometer, both manufactured

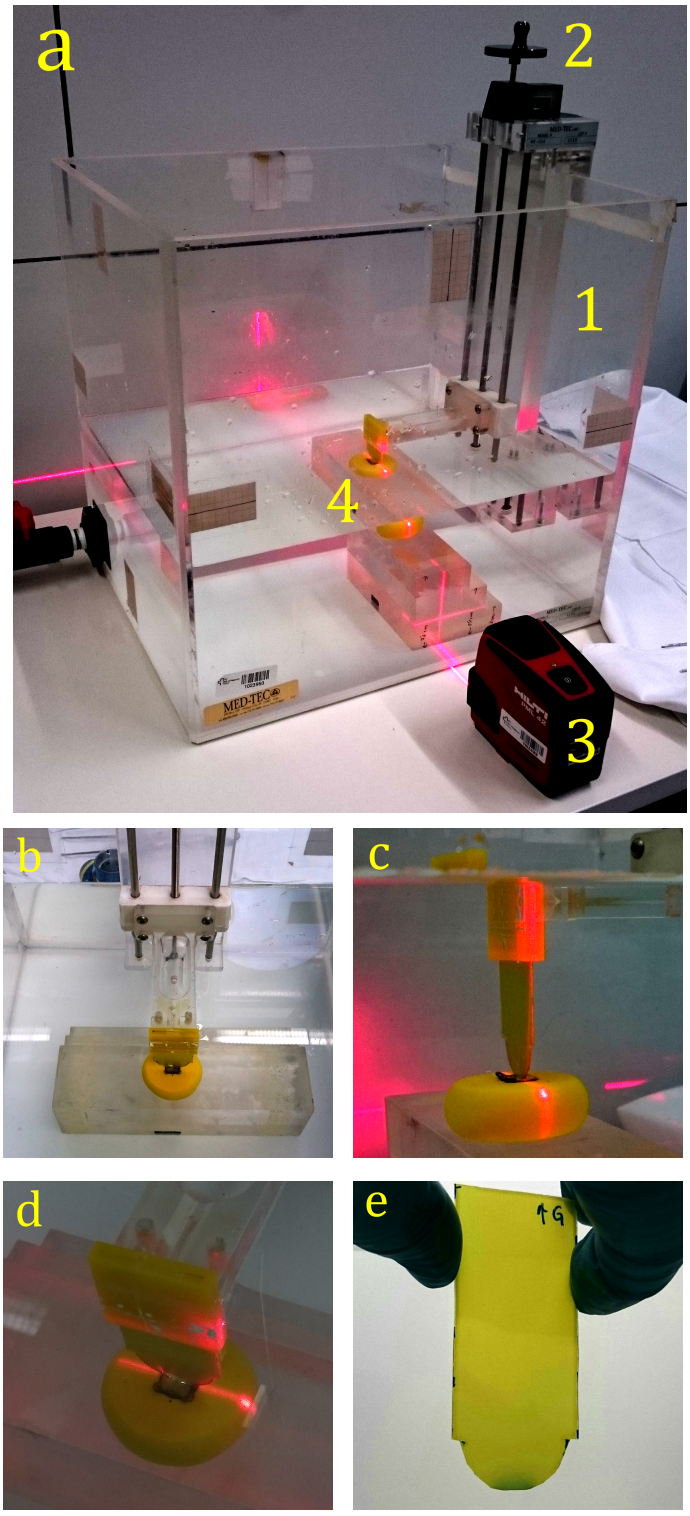

FIGURE 4.3: Experimental setup for measurement at the PDD dose planes. The whole system was leveled before measuring. Water level was about 60 mm above the plaque surface. (a) General view of the setup– 1: Water tank, 2: Screw device that allows to manually move the film support in the vertical axis with precision of 0.1 mm, 3: Laser level to check the alignment of the film and the plaque, 4: Applicator in the mold, and film in measuring position. (b) Sagittal view. (c) Lateral view with vertical laser beam parallel to the film edge. (d) Alignment of the film and the plaque checked with laser level. (e) Sample of film irradiated with this setup.

by PTW (Freiburg, Germany). The chamber–electrometer set was calibrated in absorbed dose to water in 2014 at the PTW secondary laboratory, which is traceable to the Physikalisch–Technische Bundesanstalt. For the absorbed dose measurement in reference conditions, the center of the chamber was located at 100 cm from the radiation source of the accelerator, at a depth of 10 cm in the water phantom. A square radiation field of side 10 cm was used.

Although the measurements of the $^{106}Ru/^{106}Rh$ plaques were carried out in water, for convenience the calibration films were irradiated in a PMMA phantom composed by plates of $300 \times 300 \times 10$ mm^3. The films were set at a depth of 50 mm in the phantom. The distance between the radiation source from the accelerator and the films was 100 cm. The films were irradiated with a square radiation field of side 20 cm. Ten centimeters of PMMA were inserted under the film for backscattering purposes. Nine strips were used. One of the strips was not irradiated and the others were irradiated from 0.2 Gy to 30 Gy. The monitor units needed to give the desired doses to the film were calculated with the Varian Eclipse 11.0 treatment planning system, on a CT scan of the PMMA phantom. The accuracy of the Eclipse calculation was checked by measuring the dose inside the PMMA phantom with the ionization chamber into a PMMA plate. The differences found were within 0.3%. The elapsed time between the irradiation of the first and the last calibration film was 1 h. The films were stored in a black envelope until the scanning process.

The calibration and measurement films were read 19 h after exposure in an Expression 10000XL flatbed scanner (Seiko Epson Corporation, Nagano, Japan). A resolution of 72 dpi (0.353 mm/pixel) and 16 bits per color channel were used, according to the recommendations of the manufacturer. That is, the color level for each channel (red, green and blue) is represented using $2^{16} = 65536$ discrete values. A higher resolution of 150 dpi was tested but it was discarded as the calibration uncertainty increased due to noise in the image. The scanner was warmed up for at least 120 min before the scanning process. The calibration strips were scanned all at once in the same scan to avoid the uncertainty associated with interscan variations. One possible source of uncertainty in film scanning is bending of the film, specially for small pieces. To avoid bending, a glass plate was positioned over the film in the scanner surface, for both the calibration and measurement films.

The usual method for radiochromic film dosimetry has been based on information extracted from a single color channel, assigning a dose to each color level. As a result, any color disturbances on the image, such as those due to film thickness variations or other artifacts, are transformed into dose variations from the true dose value (Devic, 2011). Micke et al. (2011) proposed the first triple–channel method to take profit of the different responses of the film components to irradiation: whereas the red channel response is dominated by the active layer of the film, the blue channel response is dominated by the presence of the yellow marker dye incorporated to the film[11]. They modeled the scanned optical density distribution as a product of two factors: a dose–dependent factor, which is the true dose map, and a

[11] The green channel is also sensitive to irradiation, but it is more sensitive to doses above 10 Gy, whereas the red channel is more sensitive to lower doses such as those used in this work.

dose–independent perturbation. By minimizing the differences in the dose obtained from the different color channels, the dose–independent contribution can be derived. In this way, the method removes the effect of film non–uniformities and thickness variations, scanner artifacts, and other disturbances on the measured dose distributions. This method was implemented by the film manufacturer in the film analysis software FilmQA Pro 2015, which was used to obtain the measured dose distributions presented in this chapter.

The scanned calibration films saved in TIFF format were imported into FilmQA Pro 2015 software. For each calibration strip, a region of interest (ROI) was defined at the central part of the film. The average of the color levels inside the ROI was correlated with the corresponding dose to the film. Then, a fit for the color level X (rescaled to discrete values between 0 and 1) against the dose D (in Gy) was made for each color channel, using rational functions of the form $X(D) = a + b/(D + c)$. This type of rational functions is a convenient choice as they need only three fit parameters, which means that with a small number of calibration films it is possible to obtain an accurate fit valid for a wide dose range. Moreover, rational functions are monotonic, matching the physical response of the film better than polynomials (Micke et al., 2011). Figure 4.4 shows the calibration curve obtained in this work for each color channel, and Table 4.1 shows the fit parameters with the corresponding standard uncertainties. For the range of doses used in this work (below 8 Gy), the red channel shows the most sensitive response. Hence, all dose distributions from the films were obtained using the calibration for the red channel.

TABLE 4.1: Fit parameters with standard uncertainties for the calibration curve of each color channel. The sum of squared residuals (χ^2) shows the goodness of the fits.

	Red	Green	Blue
a	$(45.957 \pm 2.663) \times 10^{-3}$	$(-6.4180 \pm 5.437) \times 10^{-3}$	$(46.845 \pm 5.822) \times 10^{-3}$
b	1.7695 ± 0.0329	3.9848 ± 0.1255	4.1988 ± 0.2392
c	3.0354 ± 0.04927	6.3983 ± 0.1624	12.767 ± 0.5411
χ^2	3.796×10^{-5}	5.886×10^{-5}	2.240×10^{-5}

4.2.3 Evaluation of measured dose distributions

The experimental results were obtained for the 2D dose distributions at the XZ plane, which contains the symmetry axis (Z axis) of the plaque (PDD plane), and for the 2D dose distributions at a plane perpendicular to the symmetry axis at a film–plaque distance of 5 mm. The measured dose distributions were compared to the Monte Carlo simulation results presented in chapter 2. Also, absolute dose rate values were extracted from the measured films and compared to the values stated in the calibration certificates provided by the manufacturer, which are traceable to the NIST.

After the scanned films were processed with the FilmQA software to obtain 2D dose maps, ROIs were selected on relevant areas of the scanned films and the dose matrices were exported

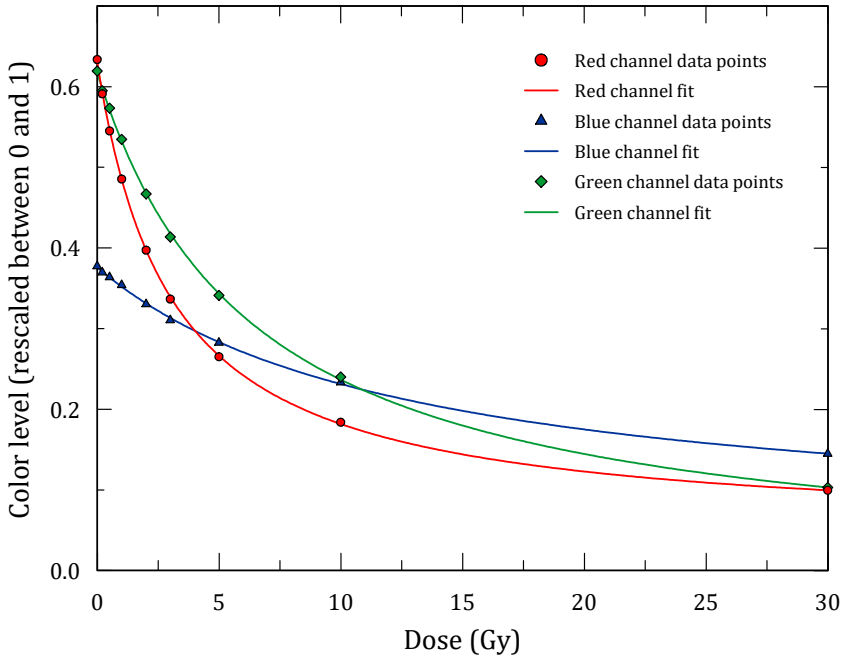

FIGURE 4.4: EBT3 dose calibration functions relating color level (at 16 bits per color channel, that is, the color level is represented using $2^{16} = 65536$ discrete values) and absorbed dose given to calibration film strips. The data points were fit to a rational function $X(D) = a + b/(D + c)$, with X being the color level rescaled to values between 0 and 1, and D the absorbed dose.

to be further analyzed with MATLAB. When comparing 2D dose distributions in this work, the first step was to *register* the dose distributions to be compared. Image registration consists of aligning the same features in images collected in different situations or with different image modalities (Crum et al., 2004). It involves applying geometric transformations to an image to minimize the differences respect to another (reference) image. Only rigid transformations were applied (i.e. shifts and rotations) to correct minor misalignments and rotations occurred during the measurement and the scanning process.

The measured dose distributions were normalized as follows. The PDD dose planes were normalized to the dose of the bin located at 2 mm from the film edge along the symmetry axis of the plaque. For the perpendicular dose planes, the normalization was done respect to the value of the central bin of the dose distribution. The geometrical center of this bin corresponds to the point of intersection between the symmetry axis of the plaque and the film. All comparisons of 2D dose distributions presented in this chapter are made between normalized dose distributions.

The agreement between the 2D dose distributions (measured against measured, and measured against simulated) was assessed through the *gamma index* (Low et al., 1998), commonly used to evaluate dose distributions in radiotherapy. The simplest metric to compare two dose distributions is the dose difference. This is adequate in low dose–gradient regions, but in regions of high dose–gradient, a small spatial error in the calculation or the measurement

may produce a high dose difference. For these high dose–gradient regions, the distance–to–agreement (DTA) is a more adequate metric. The DTA is defined as the distance between a data point from the reference dose distribution and the nearest point in the evaluated dose distribution with the same dose. The gamma index combines the dose difference and the DTA into a single metric. When an evaluated dose distribution $D_e(\vec{r}_e)$ is compared to a reference dose distribution $D_r(\vec{r}_r)$, the dose difference is

$$\delta(\vec{r}_e, \vec{r}_r) = D_e(\vec{r}_e) - D_r(\vec{r}_r), \tag{4.1}$$

and the distance between the point $\vec{r}_e$ in the evaluated distribution and the point $\vec{r}_r$ in the reference distribution is

$$r(\vec{r}_e, \vec{r}_r) = |\vec{r}_e - \vec{r}_r|. \tag{4.2}$$

If ΔD and Δr are the acceptance criteria for the dose difference and the DTA, respectively, the gamma index at the reference point $\vec{r}_r$ is then defined as

$$\gamma(\vec{r}_r) = \min \left\{ \sqrt{\left(\frac{\delta(\vec{r}_e, \vec{r}_r)}{\Delta D} \right)^2 + \left(\frac{r(\vec{r}_e, \vec{r}_r)}{\Delta r} \right)^2} \right\} \quad \forall \{\vec{r}_e\}, \tag{4.3}$$

where the expression in braces is computed for a set of points $\{\vec{r}_e\}$ for each reference point $\vec{r}_r$. In this work, the set of points $\{\vec{r}_e\}$ are those within a distance of three times the DTA criterion (Wendling et al., 2007). The global gamma index was used, that is, the dose difference percentage is referred to the maximum dose of the reference dose distribution. The bins included in the gamma analysis were those with doses greater than 10% of the maximum dose of the reference dose distribution. This percentage is the so–called dose threshold. As commented in chapter 2, in the simulations the bins that cross the interface between the plaque and the water phantom are subject to a partial–volume effect. To avoid a bias in the comparison results due to this effect, the involved bins were not included in the gamma analysis.

For each comparison, the percentage of agreement is reported, which is the percentage of evaluated bins with gamma index less than unity. We consider that an acceptable agreement is obtained for given gamma criteria if the percentage of agreement is above 90%. The statistical fluctuations inherent to simulated dose distributions affect the gamma evaluation, underestimating the average gamma index, and therefore overestimating the percentage of agreement (Graves et al., 2013). The effect reduces if the statistical uncertainty of the simulations is low, such as in the results presented in chapter 2 (with standard statistical uncertainties typically below 0.3%). The MATLAB routine to compute the gamma index was taken from the work of Scherman (2009), with permission from the author.

4.3 Results and discussion

4.3.1 Absolute dose rate

Table 4.2 shows the measured dose rates extracted from the PDD films (at 2 and 5 mm deep) for the CCA 1440 and CCX 228 plaques, and from the perpendicular dose plane at a film–plaque distance of 5 mm for the CCX 250 plaque. The doses reported for the CCA 1440 are the average of two measurements. The doses reported for the CCX 228 and the CCX 250 were obtained from the only available measurement for each plaque. The doses from BEBIG were taken from the calibration certificates provided with the plaques, which report a standard uncertainty of 10%. The measured dose rate agrees with the values stated in the certificates within the experimental uncertainties.

TABLE 4.2: Measured absolute dose rate values compared with the values stated in the calibration certificates of the plaques provided by BEBIG, corrected by decay to the date of measurement. The stated standard uncertainty values are derived from the uncertainty analysis of section 4.3.4.

	CCA 1440 PDD		CCX 228 PDD		CCX 250 axial plane
	z = 2 mm	z = 5 mm	z = 2 mm	z = 5 mm	z = 5 mm
Measured (mGy/min)	20.49±1.52	7.40±0.55	26.64±1.97	7.39±0.55	17.81±0.68
BEBIG (mGy/min)	22.86±2.29	7.73±0.77	26.25±2.63	7.09±0.71	17.08±1.71
Relative difference (meas.–BEBIG)	−11.57%	−4.46%	1.46%	4.06%	4.10%

4.3.2 Dose plane perpendicular to the symmetry axis at a film–plaque distance of 5 mm

To evaluate the setup uncertainty, three independent measurements with the CCA 1440 plaque were done (Figure 4.5). The irradiation time (2 h) was the same for the three films. The arithmetic mean of corresponding bins in the dose matrix of the measured distributions was computed to obtain an average measured dose distribution. Each measured distribution was then compared to this average distribution using the gamma index. For gamma criteria of 3%/0.5 mm (acceptance criterion of 3% for the dose difference, and of 0.5 mm for the DTA), the percentage of agreement was 97.8%. This result suggests that the uncertainty associated to the measurement repeteability is better than 3% and 0.5 mm. The measured distributions showed an inhomogeneity region consistent with the information provided in the calibration certificate of this particular plaque.

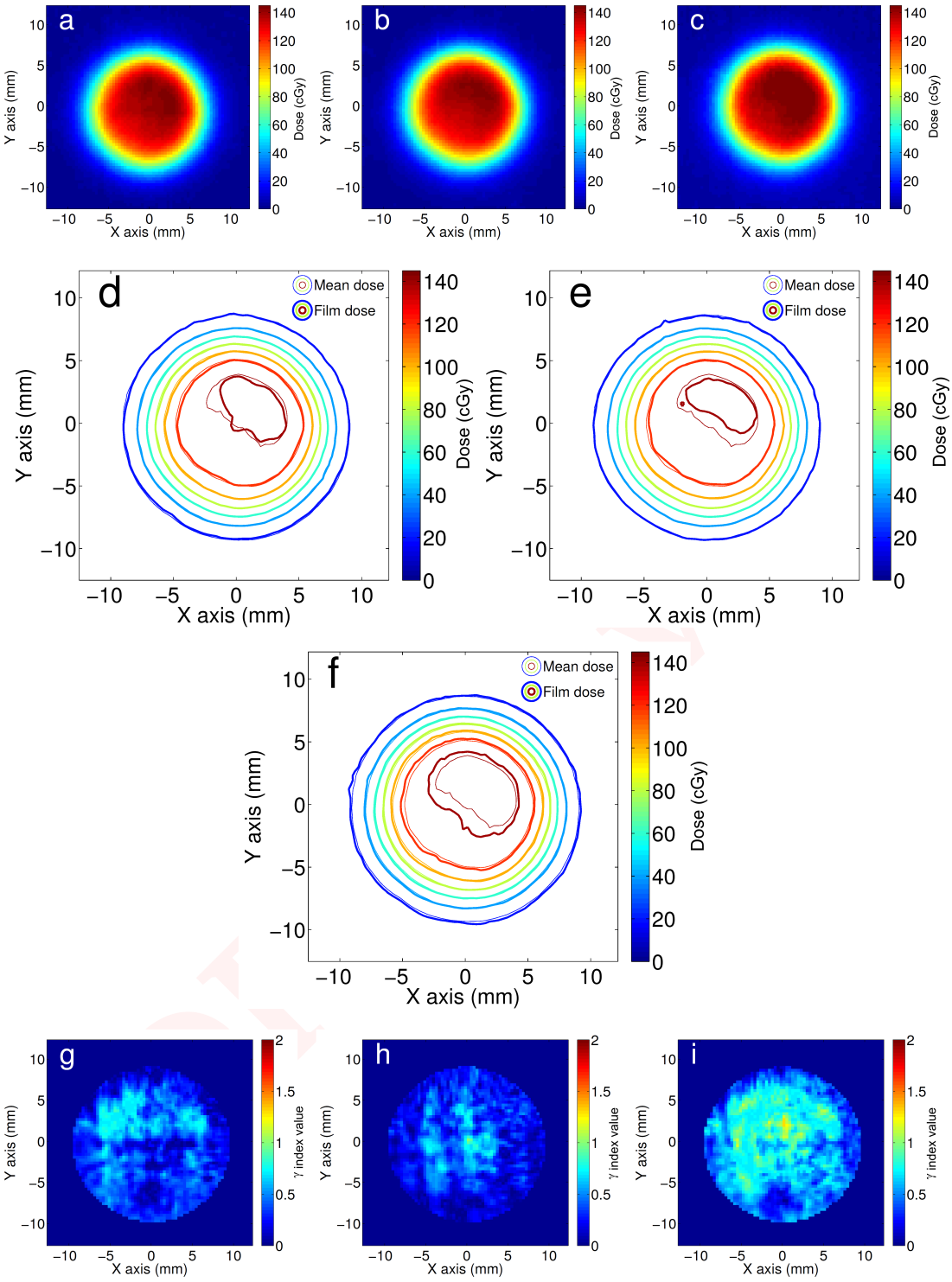

FIGURE 4.5: Repeteability of the setup to measure dose planes perpendicular to the symmetry axis for the CCA 1440 plaque. (a)–(c): Measured absolute dose distributions at an axial plane at a depth of 5 mm from the plaque surface, for three independent measurements of the CCA 1440 plaque. (d)–(f): Comparison of each measured distribution ('Film dose' in the graphs) with the average dose distribution, for registered dose distributions using a rigid transformation (i.e. shifts and rotations). (g)–(i): γ index maps for each measured distribution against the average dose distribution, which was the reference set for the gamma index analysis. The values for the percentage of agreement yielded by the γ index analysis were, from left to right, 100.0%, 100.0% and 97.9%, for γ criteria of 3%/0.5 mm.

Figure 4.6 shows the comparison of the average measured dose distribution for the CCA 1440 plaque against the corresponding results from the Monte Carlo simulation. Both planar distributions were normalized to the value of the central bin, and were registered with a rigid transformation. The disagreement found is consistent with the inhomogeneity of the radioisotope distribution of this particular plaque, as the simulations from this work assumed that the radioisotope was homogeneously distributed on the active layer. With gamma criteria of 3%/0.5 mm the agreement is poor, only 68.3%. To obtain an acceptable agreement (above 90%), the gamma criteria need to be relaxed up to 6%/1 mm.

For the CCX model, two plaques were measured, CCX 228 and CCX 250, to investigate differences in source inhomogeneity among plaques of this model. Figure 4.7 shows the good agreement obtained with percentages of agreement above 99% for gamma criteria of 3%/0.5 mm.

Figure 4.8 shows the comparison of the average measured dose distribution for CCX plaques compared to the simulation results. Although there is a good agreement between measurements and simulation results in the central region, there is a remarkable disagreement at the edges of the dose distribution in the region around the isodose line of 10%, with differences of about 6% relative to the dose maximum, which could be explained by an inhomogeneous distribution of the radioisotope near the edges of the studied CCX plaques. The calibration certificates provided by the manufacturer include measurements made with a plastic scintillator at points located at 1 mm from the plaque's inner surface, and at several positions from the axis to 5 mm beyond the edge of the plaque. Figure 4.9 shows radial averages of these measurements for the plaques studied in this work. The dose at 5 mm outside the edge is about 60% greater for the CCX 228 and the CCX 250 plaques, than for the CCA 1440 plaque. These data are consistent with the measurements from this work.

Dose profiles along the X axis were extracted from the average measured dose distributions for both plaque models and were compared with the corresponding profiles from the Monte Carlo simulations and with the available published data (Figure 4.10). The asymmetry of the measured dose profile for the CCA 1140 plaque is due to an inhomogeneous radioisotope distribution (see Figure 4.5). The discrepancy in measured dose respect to the Monte Carlo curve at points far from the axis is appreciably greater for the CCX than for the CCA plaque: at 10 mm from the axis that difference is 2.2% for the CCA plaque and 6.4% for the CCX plaque. The measurements with radiochromic film by Kirov et al. (2005) for the CCX plaque agree well with the measurements from this work even at distances far from the axis, indicating that an inhomogeneous radioisotope distribution near the edges of the plaque is a feature of the specific CCX plaques studied herein and in the work of Kirov et al. (2005).

4.3.3 Films at a plane containing the symmetry axis (PDD plane)

To study the setup repeteability two films were irradiated using the CCA 1440 plaque. Since the films were irradiated during different time (150 and 130 min), the dose distributions were normalized at a depth of 2 mm (Figure 4.11). The measured distributions were registered

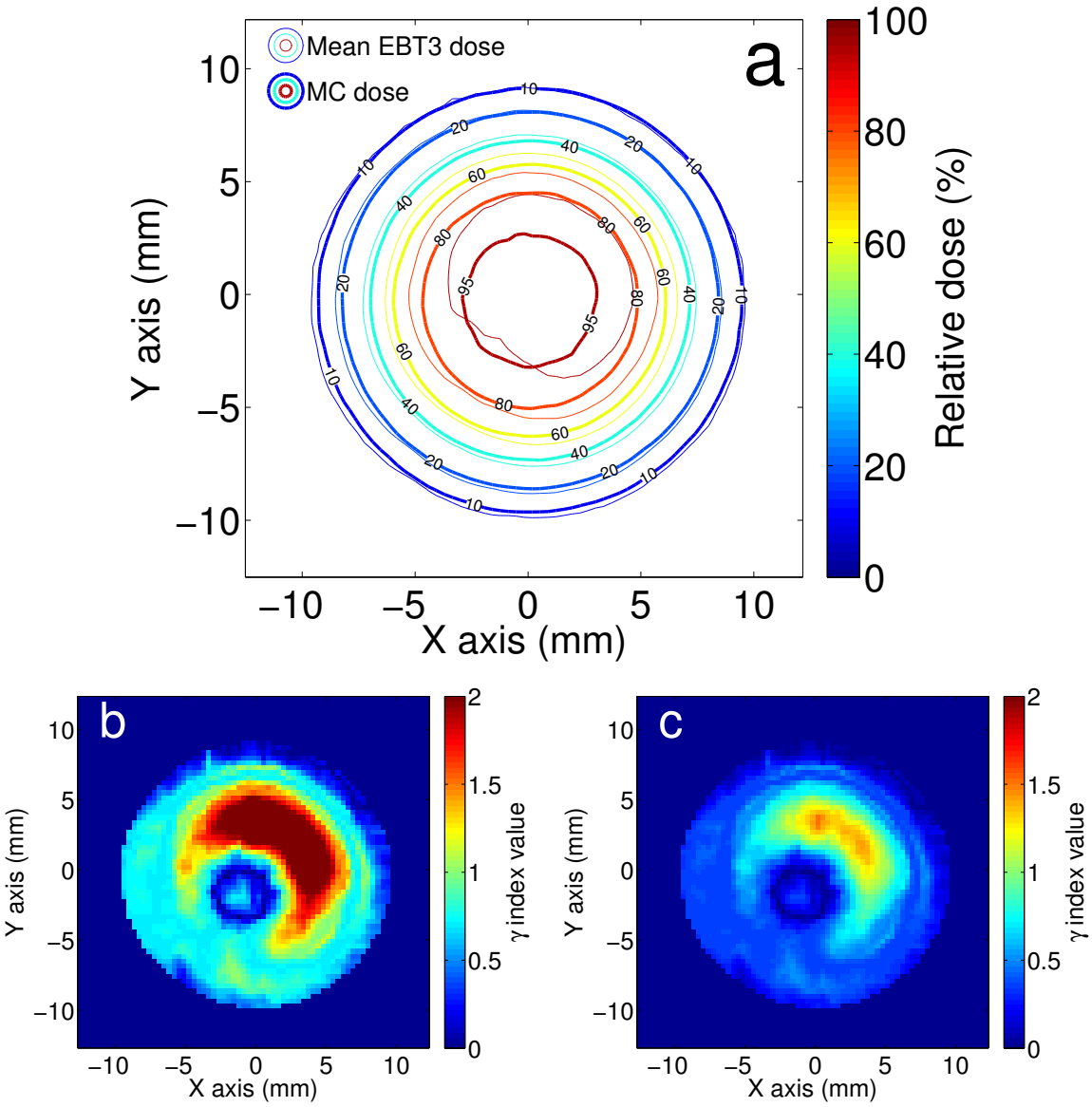

FIGURE 4.6: Measured dose plane perpendicular to symmetry axis for the CCA 1440 plaque compared to Monte Carlo simulation results. (a) Average of measured dose distributions against simulated dose distribution. Both dose distributions were normalized to the value of the corresponding central bins. (b) Gamma index map with criteria of 3%/0.5 mm shows that 68.3% of the analyzed bins have a γ index equal or less than 1. The reference set was the average of measured dose distributions. (c) Same as (b) but with criteria 6%/1 mm increases the agreement to 91.3%.

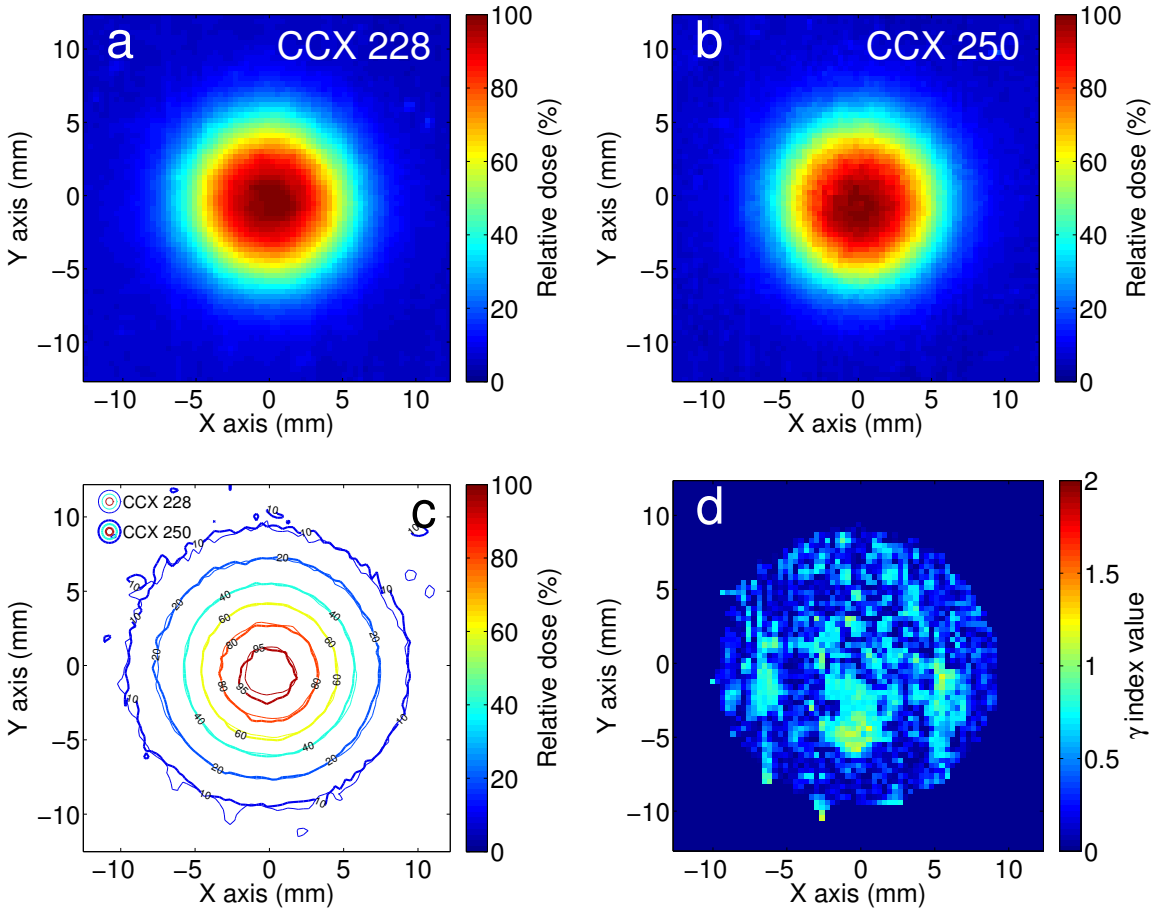

FIGURE 4.7: Measured dose plane perpendicular to symmetry axis for the CCX 228 and the CCX 250 plaques. (a) Normalized measured dose for the CCX 228 plaque. (b) Normalized measured dose for the CCX 250 plaque. (c) Comparison of measured dose maps of the CCX 228 and the CCX 250 plaques. (d) Gamma index map for criteria of 3%/0.5 mm, resulting in a percentage of agreement of 99.1%. The CCX 228 was taken as the reference set, and the CCX 250 was taken as the evaluated set. It was checked that the results are very similar if we exchange the reference and evaluated sets.

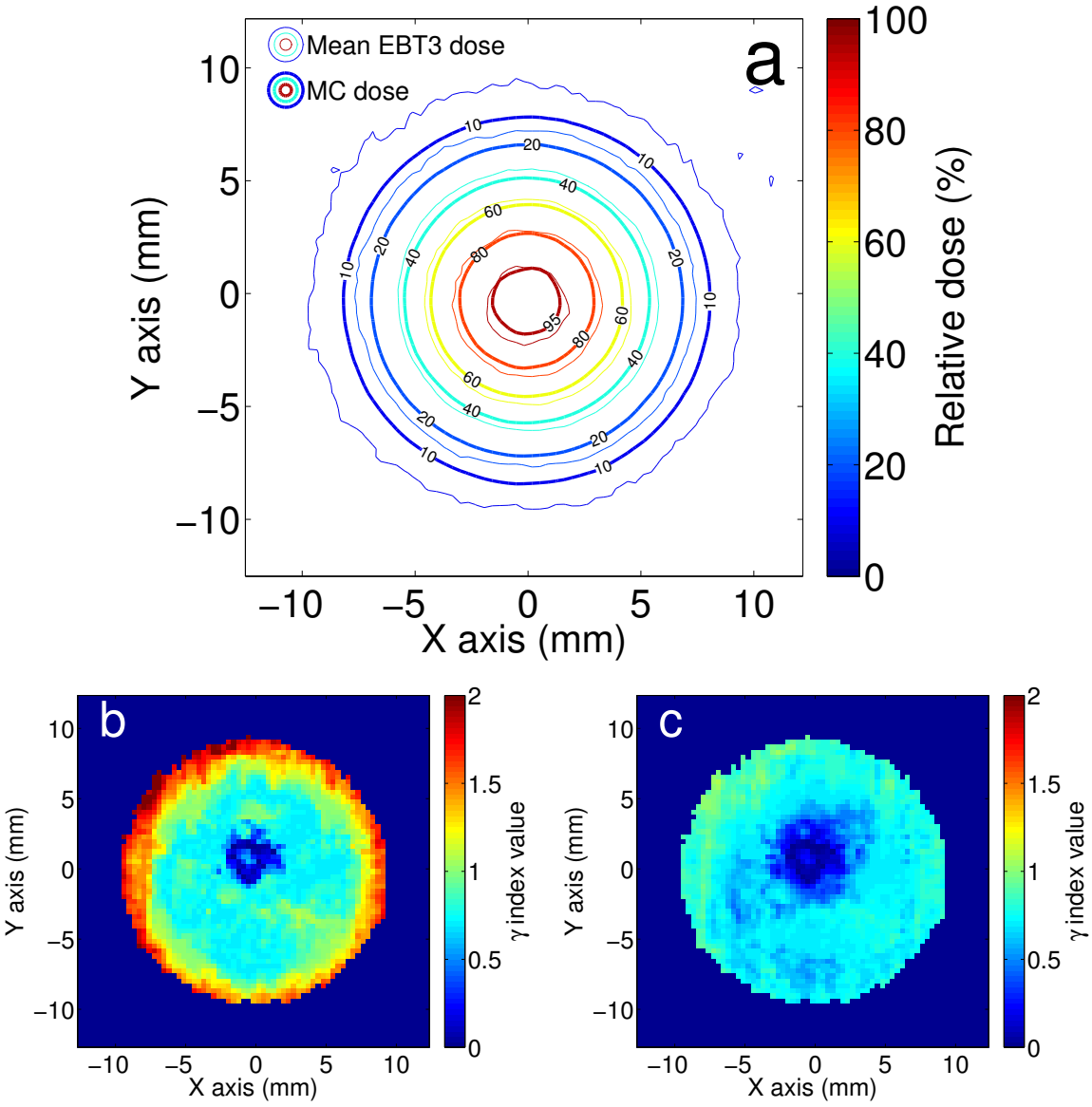

FIGURE 4.8: Measured dose plane perpendicular to symmetry axis for CCX plaques, compared to Monte Carlo simulation results. (a) Average of measured dose distributions against Monte Carlo dose distribution for the CCX 228 and the CCX 250 plaques. Measured and estimated dose distributions are normalized to the value of the central bin of each dose distribution. (b) Gamma index map with criteria of 3%/0.5 mm. The obtained percentage of agreement was 56.9%. (c) Same as (b) but with criteria of 7%/0.5 mm increases the agreement to 99.4%. For the gamma evaluations, the measured dose distribution was used as the reference set.

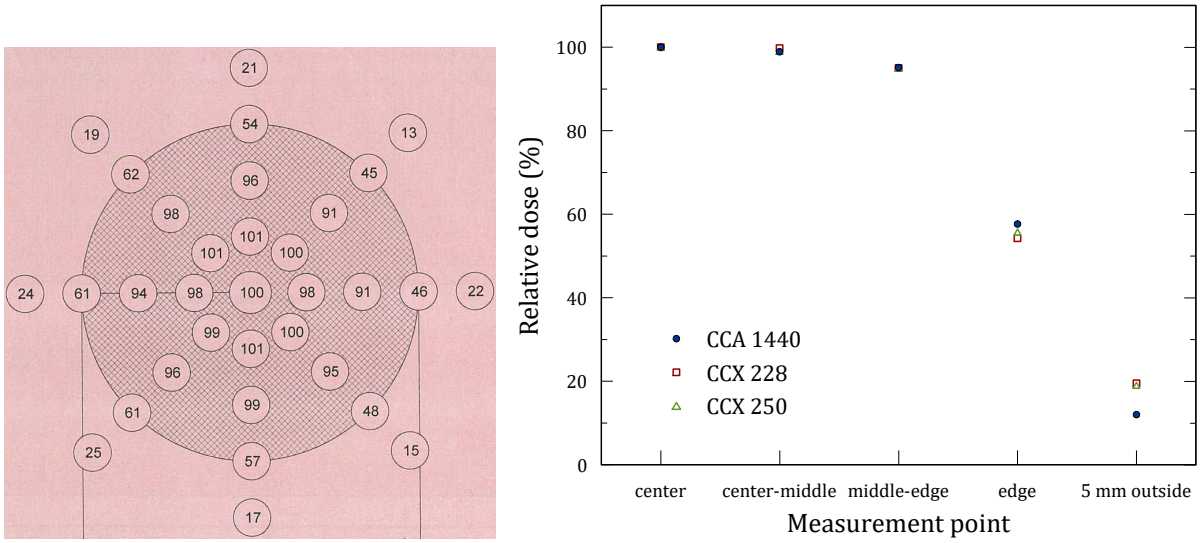

FIGURE 4.9: LEFT: Example of dose values measured by the manufacturer with a plastic scintillator at points located at 1 mm from the plaque's inner surface, as they are printed in the calibration certificate of the plaques. RIGHT: Radial averages of the aforementioned dose values for the plaques studied in this work. The differences between CCX and CCA plaques at the '5 mm outside' position are consistent with the film measurements from this work and with the results from Kirov et al. (2005).

with a rigid transformation to correct minor misalignments and rotations. A gamma index analysis was performed to evaluate the agreement between each measured dose distribution and the bin–by–bin arithmetic mean of the two measured dose distributions. This setup is not as repeatable as the setup to measure perpendicular dose planes, as the gamma criteria needed to obtain acceptable agreements were 7%/0.7 mm, with percentages of agreement of 91.7% and 91.4% for each of the irradiated films. The disagreement occurs mostly at the points near the surface of the plaque.

Figure 4.12 shows the comparison between the average of the measured dose distributions for the CCA 1440 plaque and the simulation results. The agreement for the medium and low isodose lines is good, but differences of up to 25% occur at 1 mm from the plaque surface. These differences are reduced to below 5% at distances greater than 2 mm. This is not surprising as the measurements shown in Figure 4.5 prove that this plaque has an inhomogeneous radioisotope distribution. With gamma criteria of 3%/0.5 mm the agreement is of 83.6%, and with criteria of 7%/0.5 mm the agreement increases to 92.7%. Similar differences near the plaque surface between film measurements and Monte Carlo simulation results were also reported by Heilemann et al. (2015), with differences up to 15% within the first 1.5 mm. A contributing factor to the differences could be the effect of the nail polish applied to the film edges. Hence, we recommend not to use the first 1.0–1.5 mm from the film edge to obtain dosimetric information for the films irradiated with the proposed technique.

For the CCX model only one film was available for analysis, corresponding to the CCX

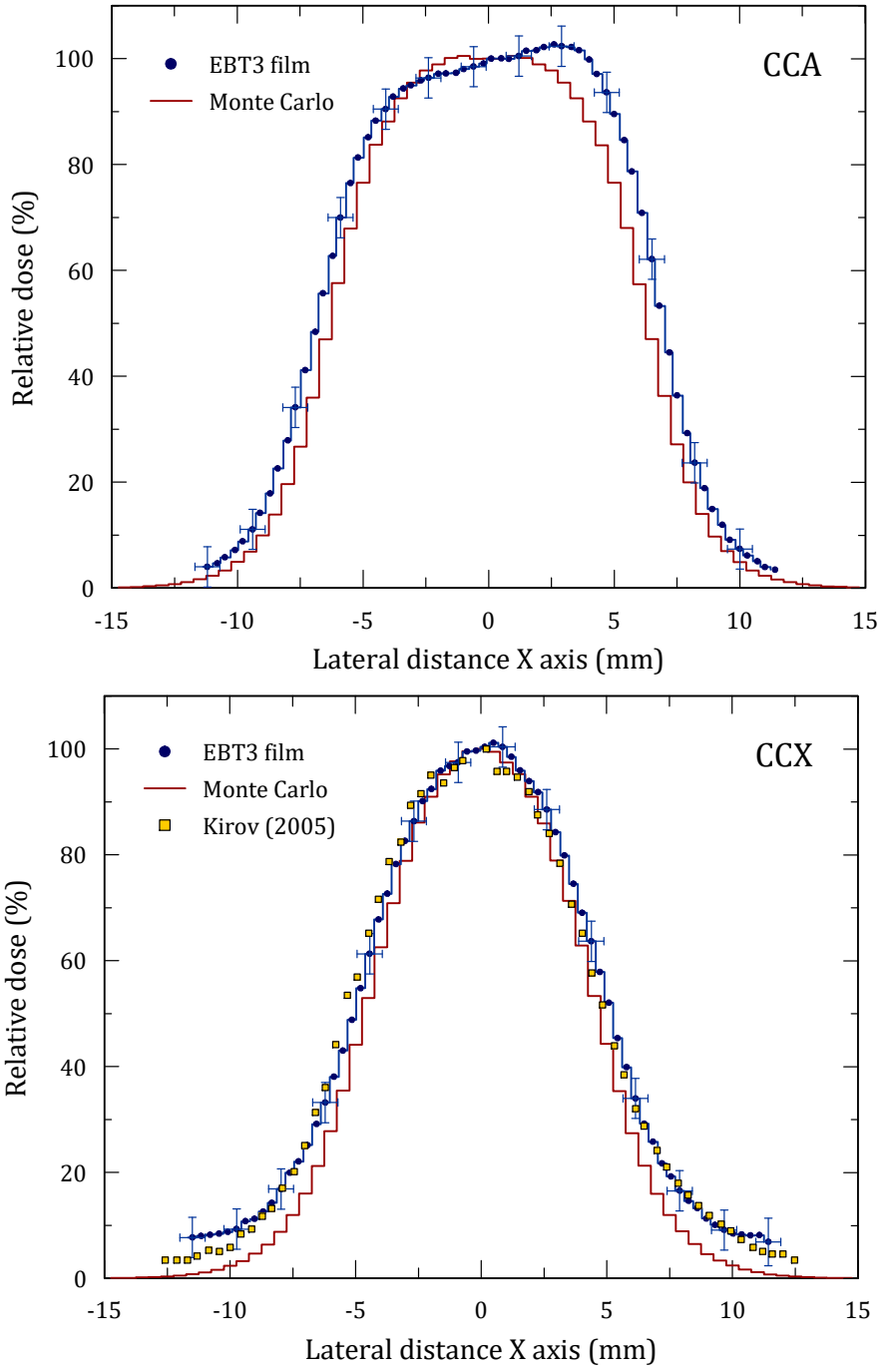

FIGURE 4.10: Profiles along the X axis at a depth of 5 mm extracted from the measured 2D dose distributions. TOP: average of three measurements of the CCA 1440 plaque and Monte Carlo simulation results from this work. BOTTOM: average of two measurements (for the CCX 228 and the CCX 250 plaques), Monte Carlo simulation results, and dose profile measured by Kirov et al. (2005) with radiochromic film. Uncertainty bars (shown each five experimental points) for measured profiles correspond to 3.8% for dose standard uncertainty, and to 0.5 mm for positioning uncertainty. Standard statistical uncertainty for simulated profiles is below 0.3% and uncertainty bars are not shown for clarity.

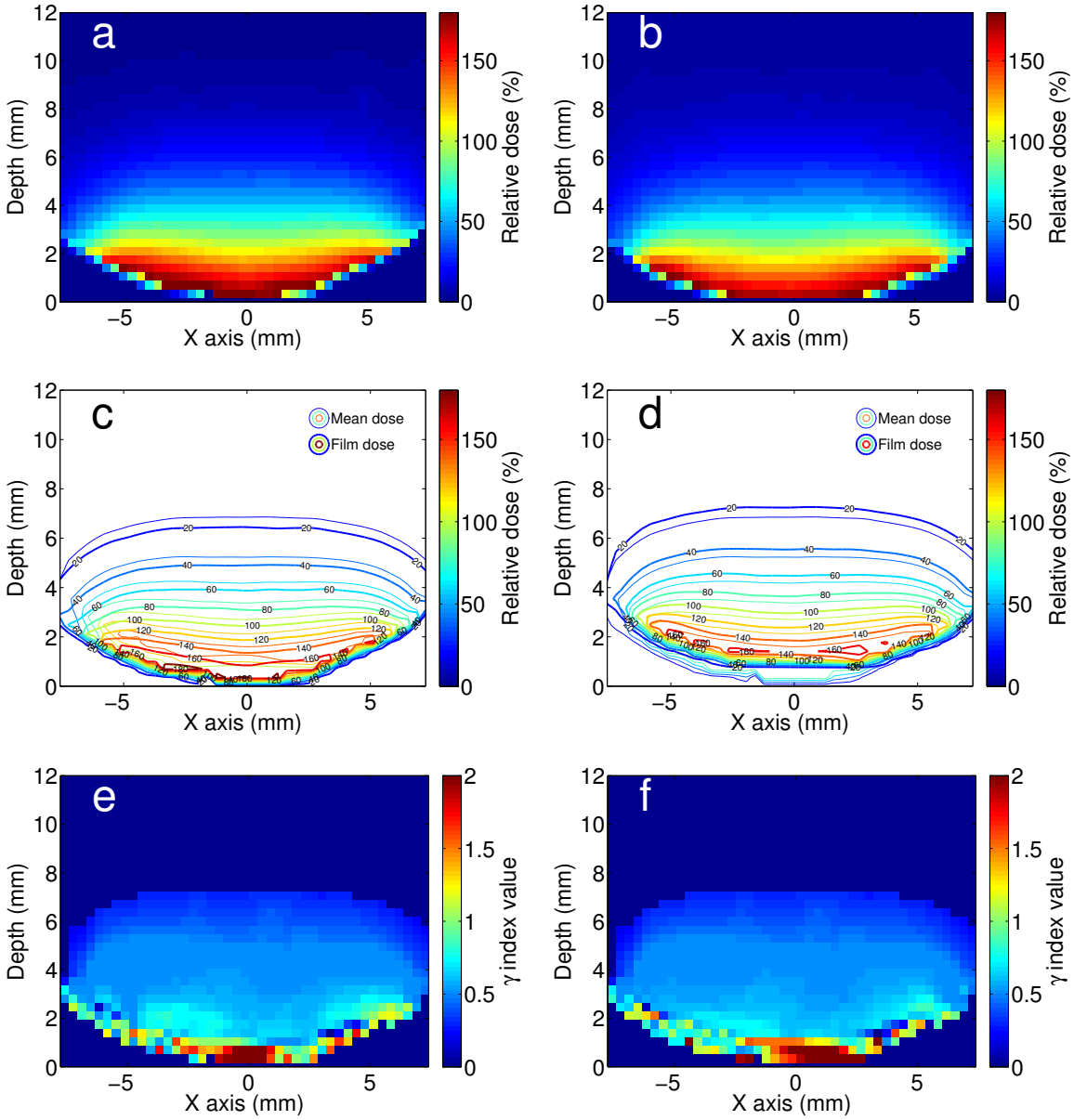

FIGURE 4.11: Measured dose planes containing the symmetry axis of the CCA 1440 plaque. (a) and (b): Dose distributions from two independent measurements normalized at a depth of 2 mm from the film edge along the symmetry axis. (c) and (d): Comparison of isodose lines for each measured distribution respect to the average of both distributions. (e) and (f): Gamma analysis of each measured distribution (evaluation set) respect to the average of both distributions (reference set), with criteria of 7%/0.7 mm. The percentages of agreement were 91.7% (e) and 91.4% (f).

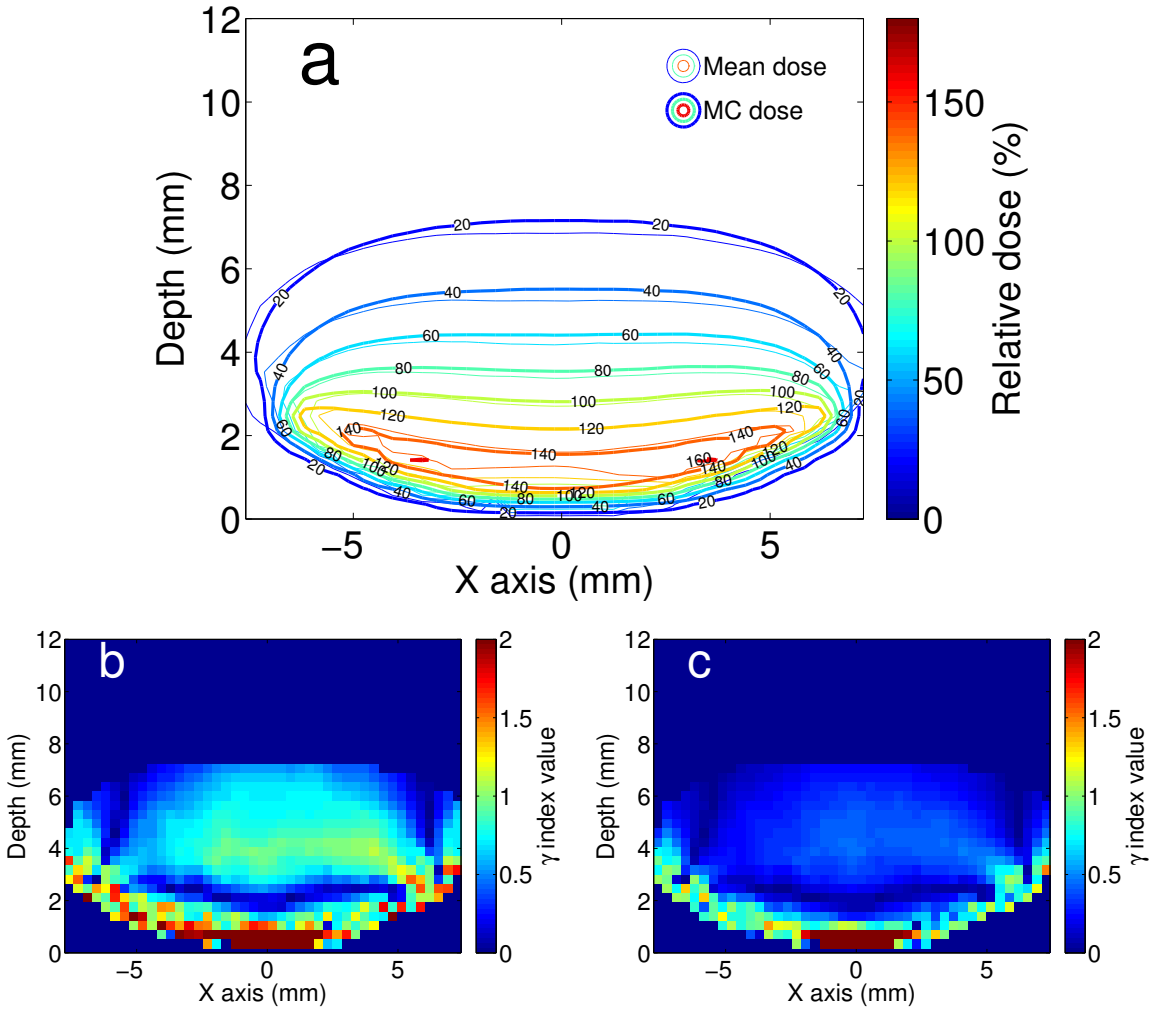

FIGURE 4.12: Average of the measured dose distributions at a plane containing the symmetry axis for the CCA 1440 plaque, compared to the Monte Carlo simulation results obtained in chapter 2. (a) Comparison of isodose contours normalized at a depth of 2 mm from the film edge along the symmetry axis. (b) Gamma index map with criteria of 3%/0.5 mm shows an agreement of 83.6%. (c) Gamma index map with criteria of 7%/0.5 mm increases the percentage of agreement to 92.7%. The average of the dose distributions was used as the reference set for the gamma analysis.

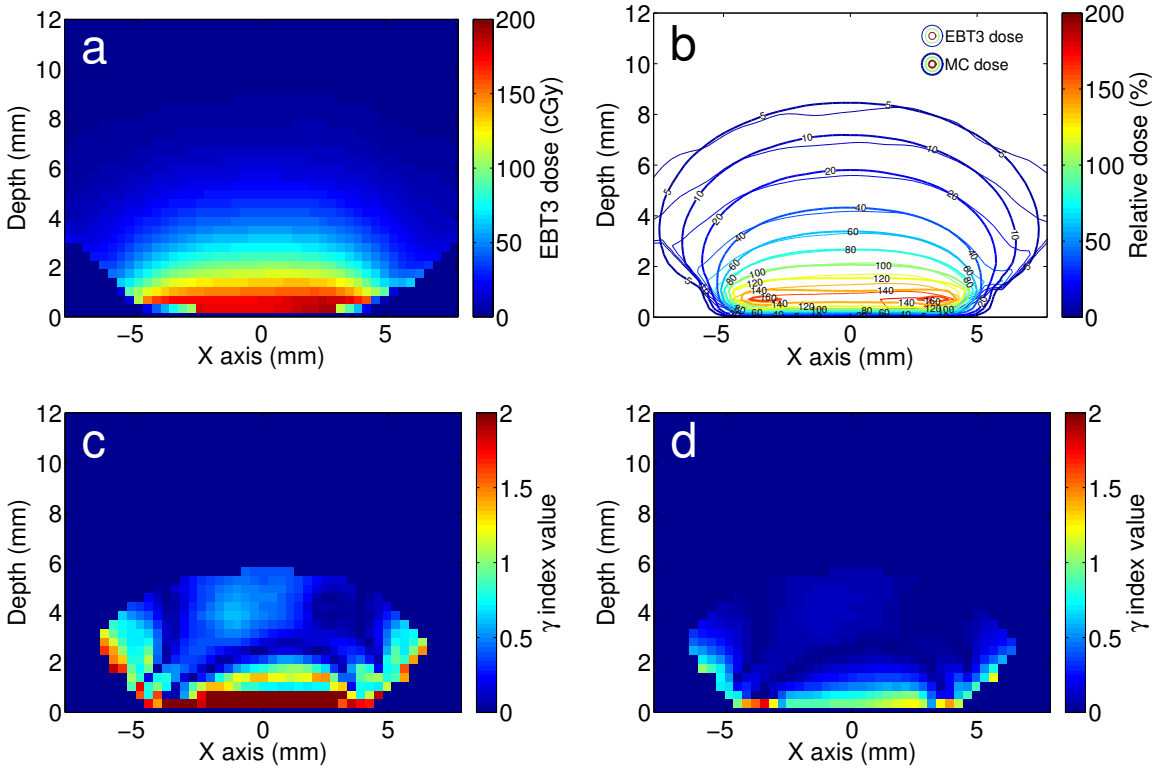

FIGURE 4.13: Measurement of a dose plane containing the symmetry axis for the CCX 228 plaque. (a) Measured dose distribution. (b) Measured dose distribution compared to Monte Carlo simulation results. (c) Gamma index map from the comparison between measured and Monte Carlo dose distributions with γ criteria of 3%/0.5 mm. Poor agreement: 80.9%. (d) Same as (c), but with γ criteria of 15%/0.5 mm increases the agreement to 96.6%.

228 plaque (Figure 4.13). As in the case of the CCA 1140 plaque, the agreement between measurement and simulations is rather good for depths greater than 2 mm (dose differences below 5%), but there is a large disagreement (up to 20% in dose difference) in the first 1.5 mm.

Depth–dose curves were extracted from the measured dose distributions to compare with published results of measurements for the CCA and CCX models (Figures 4.14 and 4.15). These data previously appeared on Figures 2.13 and 2.15. The first 1.5 mm from the film edge were not considered in the comparisons.

The measured data in water from this work for the CCA plaque are in excellent agreement within the experimental uncertainty (differences below 2%) with the measurements by Heilemann et al. (2015), which were carried out in a plastic phantom. Our measurement results also show a better agreement with Monte Carlo simulation results than the measurements of Taccini et al. (1997) using an early model of radiochromic film (Gafchromic types 37–041 and 37–040), which reached differences from 4.6% at 6.0 mm deep to 6.0% at a depth of 3.0 mm. For the CCX 228 plaque, the measurements from this chapter agree well with the Monte Carlo simulation results from chapter 2 and with the measured data stated in the plaque calibration

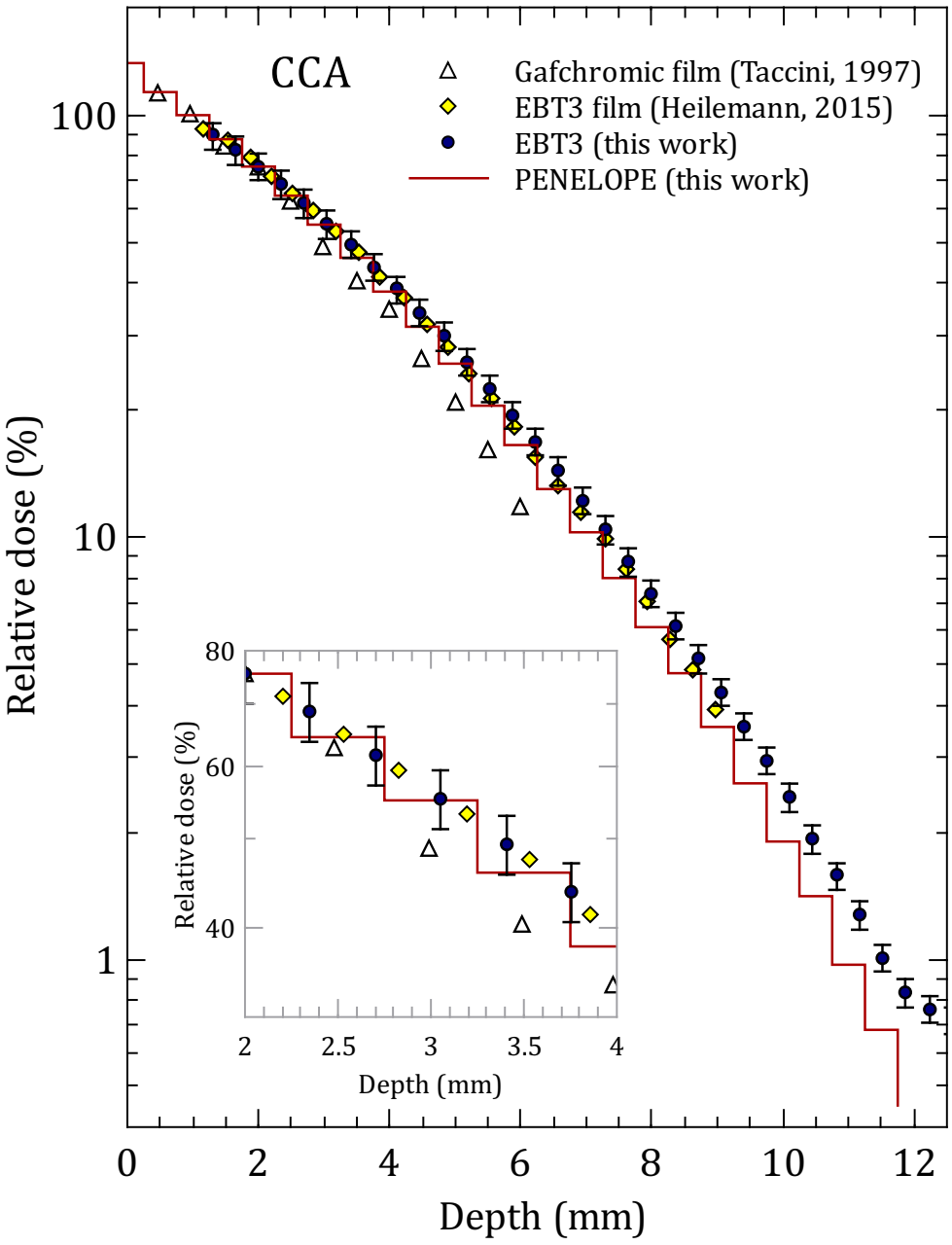

FIGURE 4.14: Relative depth–dose curve for the CCA plaque extracted from the measurements of this work using EBT3 radiochromic film compared with available published experimental results.

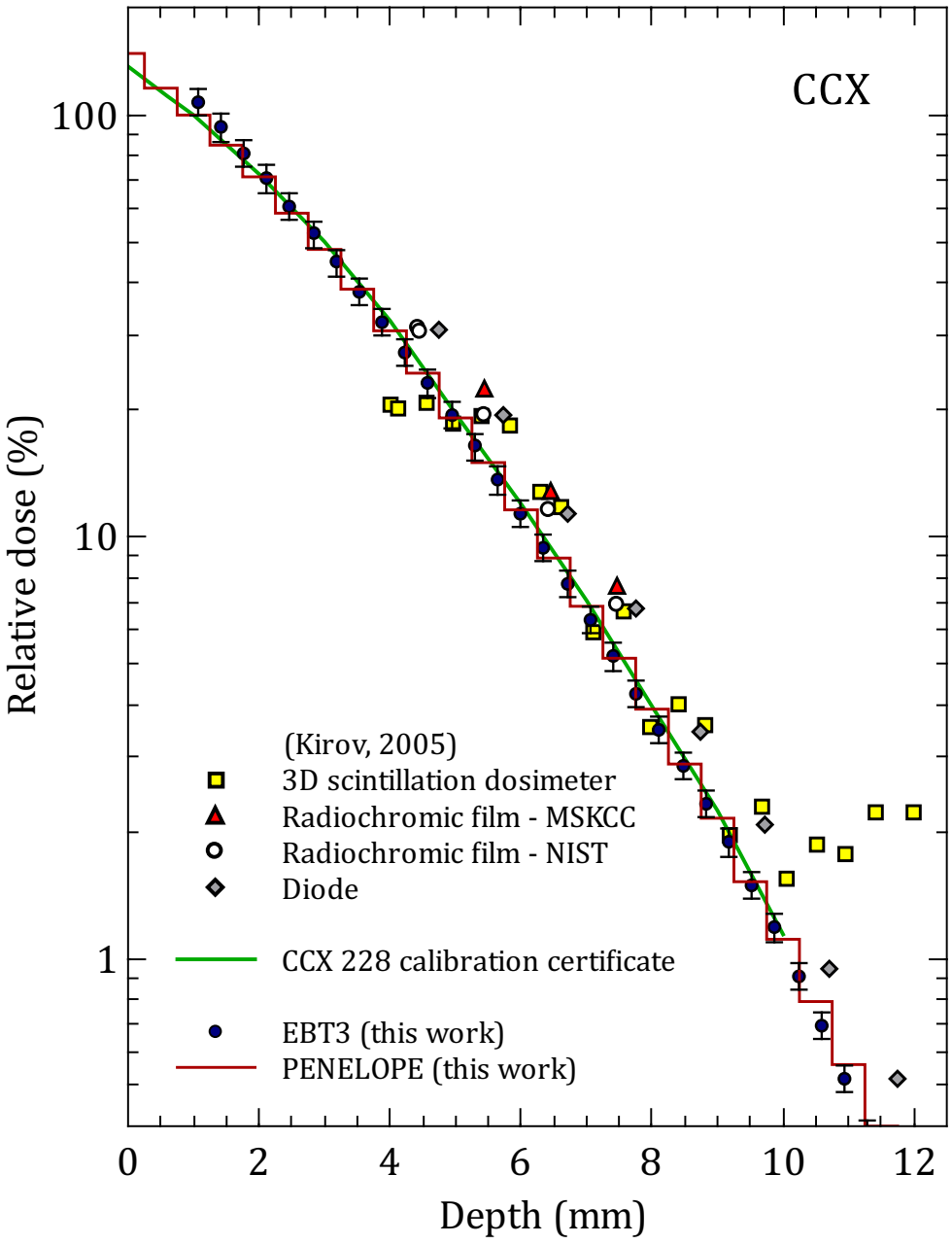

FIGURE 4.15: Relative depth–dose curves for the CCX plaque extracted from the measurements of this work using EBT3 radiochromic film compared with available published experimental results.

certificate, which were obtained by the manufacturer with a scintillation dosimeter.

To conclude, the setup proposed in this chapter to measure depth–dose curves in water for $^{106}Ru/^{106}Rh$ plaques with the EBT3 film provides results of similar or better quality than those published using radiochromic films with plastic phantoms, or with other detectors.

4.3.4 Estimation of measurement uncertainties

To estimate the combined standard uncertainty of the measured dose distributions obtained with the experimental setups proposed in this chapter, the following sources of uncertainty affecting the film calibration and measurement steps were analyzed:

1. Determination of the absorbed dose to water under reference conditions produced by the clinical linear accelerator used in the calibration of the films: this procedure includes uncertainties related to the standard laboratory where the reference ionization chamber is calibrated, as well as uncertainties related to the measurement of the dose at the hospital. According to the TRS–398 dosimetry protocol (IAEA, 2001), for high energy photon beams the combined relative standard uncertainty of this procedure is estimated to be about 1.5% (combination of type A and type B uncertainties).

2. Accuracy of the Eclipse calculation to obtain the monitor units needed to give the desired doses to the film in the PMMA phantom: comparison from the Eclipse calculation and measurements with ionization chamber in the PMMA phantom gives a relative standard uncertainty of 0.3%, determined from repeated measurements (type A uncertainty).

3. Stability of the clinical linear accelerator output: the associated relative standard uncertainty was determined from repeated measurements (type A uncertainty), giving a value of 0.1%.

4. Difference in energy dependence of EBT3 film between water and PMMA: this contribution must be assessed as the calibration was made with the films in a PMMA phantom, whereas the measurements of the dose distributions produced by the $^{106}Ru/^{106}Rh$ plaques were made with the films immersed in water. The mean value of the difference in absorbed–dose–to–water energy dependence $g(Q)$ between water and PMMA in the range 10 keV–6 MeV was 1.7%, according to the results from chapter 3, which were obtained with standard statistical uncertainties below 1%. As no additional information is available, it is recommended to assume a rectangular probability distribution, from which we can derive a value of $1.7\%/\sqrt{3} \simeq 1.0\%$ for this type B standard uncertainty (Bureau International des Poids et Mesures, 2008).

5. Difference in energy dependence of EBT3 for electrons respect to 6 MV photons: Sipilä et al. (2016) studied the dosimetric characteristics of the EBT3 film to use it in electron and photon/electron beams. They found that the dose response of the EBT3 film

was uniform within 1%, with a standard uncertainty about 0.8%. As in the previous paragraph, we assume a rectangular probability distribution, resulting in a value of $1.0\%/\sqrt{3} \simeq 0.6\%$ for this type B standard uncertainty (Bureau International des Poids et Mesures, 2008).

6. The uncertainty associated to the dose calibration process was estimated through the consistency of the calibration. Once the fit was made, the fitted function was applied to the same ROIs used to obtain the fit parameters, and the average dose obtained were compared with the doses assigned to those ROIs in the calibration. The relative consistency was expressed as the difference in percentage between the average doses read on the ROIs and the assigned doses. This relative consistency was taken as the estimated standard uncertainty of the calibration for the films irradiated to doses in the range 0.5–10 Gy, and the obtained value was 1.4%.

7. Interscan uncertainty: determined from repeated scans of the same film (type A uncertainty). The repeated measurements were carried out with the warmed–up scanner. The relative standard uncertainty was taken as the standard deviation of the mean dose in a selected ROI for a series of repeated scans. This value resulted to be 0.3%.

8. Setup repeteability: assessed from the gamma index analysis of repeated measurements for each setup. The dose criterion needed to obtain a satisfactory agreement in the gamma analysis of the available repeated measurements was assumed to be similar to the relative standard dose uncertainty of the setup (type B uncertainty). The values obtained were 3% for the setup to measure dose planes perpendicular to the symmetry axis of the plaques at a film–plaque distance of 5 mm, and 7% for the setup to measure PDD planes. This uncertainty contribution includes the dose uncertainty due to the irradiation of the film during the film positioning which was estimated to be of 0.3% for the perpendicular dose planes, and of 0.7% for the PDD planes. The setup repeteability uncertainty also includes the interscan uncertainty of item 7.

To estimate the total uncertainty of the measured dose distributions, the contributions 1–6 and 8 above were combined in quadrature, giving relative standard uncertainties of 3.8% for absorbed dose distributions measured at planes perpendicular to the symmetry axis of the plaques and at a film–plaque distance of 5 mm, and of 7.4% for PDD dose planes.

Chapter 5

Discussion

The preceding chapters already presented some discussion and conclusions on the specific issues of each chapter. Below a discussion is offered on the limitations of the methods used, the possible influence of the results from this thesis on the clinical practice of ophthalmic brachytherapy with $^{106}Ru/^{106}Rh$ plaques, and suggestions for future research.

5.1 Limitations

The EBT3 film model used in this work was designed to improve the features of the older EBT2 model, specially to reduce the energy dependence at low energies (Bekerat et al., 2014). The study presented in chapter 3 evaluated the absorbed–dose energy dependence of the EBT3 film for photon beams only. The reason was to compare with published results for older film models by Sutherland and Rogers (2010), and with the results by Bekerat et al. (2014), who studied the effect of varying the atomic composition of the active layer on the energy dependence of the EBT3 film. The main objective in chapter 3 was to assess the influence of the phantom material on the EBT3 absorbed–dose energy dependence. This influence was assessed for photons only, as previous publications have shown that the EBT3 film energy response is almost independent of the type of radiation (Sorriaux et al., 2013; Sipilä et al., 2016). An additional evidence proving the equivalent behavior of the EBT3 film with photon and electron beams is shown on Figure 5.1. The figure shows the dose calibration functions for EBT3 films from the same lot irradiated with a 6 MV photon beam and with a 4 MeV electron beam, both from a Varian Clinac 2100 clinical electron linear accelerator. The photon and electron curves are compatible within the experimental uncertainty[12].

The main limitation of the experimental measurements from chapter 4 is the reduced number of measured plaque models (CCA and CCX only). No more plaque models were available. Moreover, due to logistic limitations, a small number of repeated measurements was possible. Although it would be desirable to have more measurements, it is unlikely that the conclusions of this work would be affected in a relevant way. Another limitation of the experimental setup was the manual trial–and–error procedure to make sufficiently accurate molds.

[12] These measurements were performed by Juan Francisco Calvo Ortega, M.Sc. from the Department of Radiation Oncology, Hospital Quirón, Barcelona, Spain.

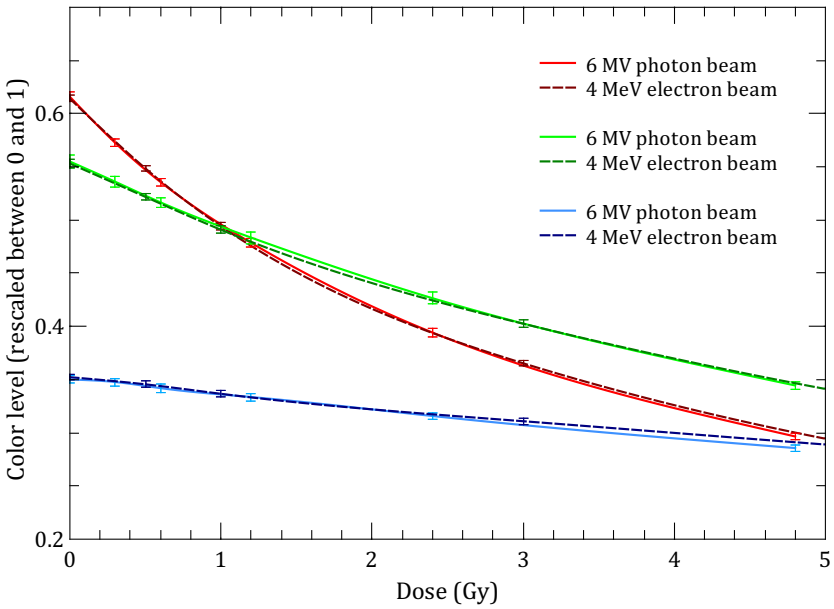

FIGURE 5.1: Dose calibration functions for EBT3 films irradiated with a 6 MV photon beam and with a 4 MeV electron beam, both from a Varian Clinac 2100 clinical electron linear accelerator. The photon and electron curves are compatible within the experimental uncertainty for all color channels. Measurements courtesy of Juan Francisco Calvo Ortega, M.Sc. from the Department of Radiation Oncology, Hospital Quirón, Barcelona, Spain.

5.2 Implications for the clinical practice

The results obtained in this thesis may influence the clinical practice at different levels. The absorbed dose to water distributions obtained from the simulations presented in Tables 2.2–2.4 from chapter 2 can be useful to perform independent checks of treatment planning calculations. As an example, Figure 5.2 shows a comparison between the Monte Carlo simulation results from chapter 2 and calculations made with the Plaque Simulator software (v. 5.3.6), taken from a work that the author of this thesis co–authored with Cano-Herranz et al. (2014).

Nowadays, no commercial device or recommended method are available to perform quality control tests to check the dose distributions and the absolute dose rate of the ^{106}Ru/^{106}Rh plaques used in the clinical practice. Thus, users may be forced to rely only on the calibration certificates provided by the manufacturer. The experimental setups proposed in chapter 4 allow users of ^{106}Ru/^{106}Rh plaques to measure in a practical way the dose distributions in water produced by the specific plaques used for treatments. The materials needed are easily affordable by a medical physics department, without the need of specifically machined solid phantoms (Taccini et al., 1997; Soares et al., 2001; Kovačević et al., 2005; Barbosa et al., 2015; Heilemann et al., 2015).

It is a common practice in brachytherapy that scientific societies propose consensus data for the most used sources, based on meta–analysis of published experimental and simulation

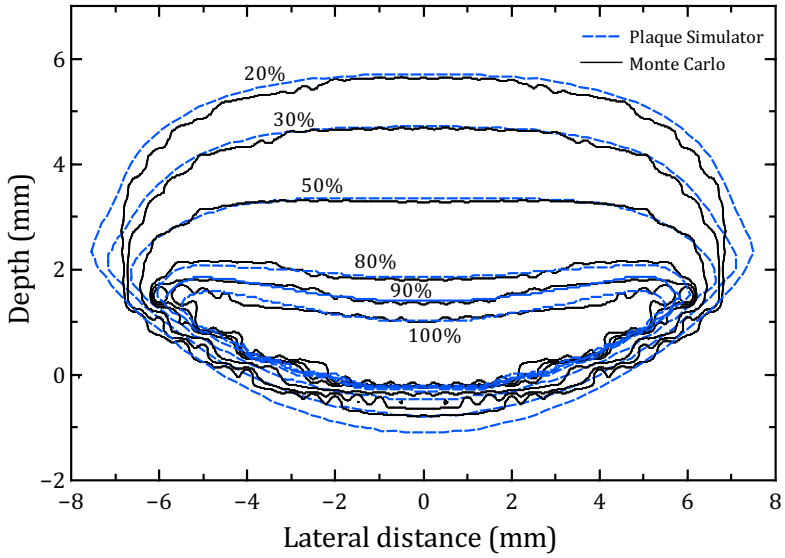

FIGURE 5.2: Comparison of isodose lines at a plane containing the symmetry axis of the CCA plaque, between the Monte Carlo simulation results from chapter 2 and calculations with the Plaque Simulator software, as shown by Cano-Herranz et al. (2014). The depth of normalization is 1 mm from the surface of the plaque.

studies. However, no such consensus data exists for ^{106}Ru/^{106}Rh ophthalmic plaques. A report just published (June 1, 2016) (Nath et al., 2016) by the Task Group 167 of the American Association of Physicists in Medicine stresses the importance of having a good characterization of the dose distribution produced by brachytherapy sources before its clinical use, via Monte Carlo simulations and/or experimental measurements. In the absence of consensus data, the report recommends the medical physicist to use candidate datasets taken from the literature. The simulation results from chapter 2 are in good agreement (about 3%) with the available data in the literature and with the experimental measurements from chapter 4. Moreover, the analysis presented in chapter 2 allowed to identify some shortages on previous publications, and to find out the causes of some discrepancies in the literature. Hence, the data set from the Monte Carlo simulations obtained in this research are the most comprehensive and reliable data available on dose distributions of ^{106}Ru/^{106}Rh plaques and may well constitute the basis for the first consensus dataset for these plaques.

5.3 Future research

Regarding the simulation of the dose distribution produced by the plaques, an improvement could be achieved by considering in the simulation the actual radioisotope distribution, instead of considering an ideal homogeneous distribution. This suggestion poses two major challenges: the measurement of the actual radioisotope surface distribution and the use of an

arbitrary radioisotope surface distribution as a source for Monte Carlo simulations. Eichmann et al. (2009) measured the surface dose rate distribution of ^{106}Ru/^{106}Rh plaques with a plastic scintillator mounted on a system that was capable of guiding the detector across the plaque surface at a constant small separation. From this surface dose rate distribution, it is possible to estimate the actual radioisotope distribution. The use of an arbitrary radioisotope distribution as a source for Monte Carlo simulation represents a non–trivial problem because the available codes do not allow this to be carried out easily. Some preliminary results of simulations using actual emitter distributions, obtained with the device developed by Eichmann et al. (2009), were presented by Brualla et al. (2016) at the 22. Jahrestagung der Deutschen Gesellschaft für Radioonkologie (Mannheim, June 2016). The estimated dose distributions using the actual emitter distribution were compatible with the experimental depth dose profiles measured in water by the manufacturer of the plaques. A topic of research would be to develop an algorithm to derive the actual radioisotope distribution from film measurements perpendicular to the symmetry axis of the plaque as those performed in this thesis.

Another line of research is the development of variance–reduction techniques designed to improve the efficiency of the simulations. The rationale is to simulate the ^{106}Ru/^{106}Rh plaques in clinical conditions, that is, using computed tomography images from real patients as previous works have done (Brualla et al., 2013), while obtaining the calculation results in a time–frame adequate for the routine clinical practice. The results from the simulations in this thesis could be used as a benchmark for those that would be obtained using variance–reduction techniques.

This thesis is framed within a far–reaching project, namely, the development of a Monte Carlo treatment planning system for ophthalmic brachytherapy with ^{106}Ru/^{106}Rh plaques. This system would be inspired on PRIMO[13] (Rodríguez et al., 2013), a user–friendly software that simulates clinical linear accelerators and estimates absorbed dose distributions in water phantoms and computed tomography datasets. PRIMO includes a graphical user interface to perform simulations with the PENELOPE code. We propose the following minimal features for a system devoted to the simulation and planning of treatments with ^{106}Ru/^{106}Rh plaques: (i) the dose calculation engine would be based on Monte Carlo simulation with PENELOPE; (ii) the simulations would be performed on the CT of the actual patients (Brualla et al., 2013), rather than on a model of the eye composed of water as Plaque Simulator does; (iii) the dose dataset obtained in this thesis could be used to obtain a fast dose estimation during the planning process. When a plaque and location were decided, the final dose simulation would be performed using the actual radioisotope distribution for the particular plaque used, as described by Brualla et al. (2016); (iv) the aforementioned variance–reduction techniques could be used to obtain an accurate dose estimation in a short time.

[13] PRIMO is free software that can be downloaded from `http://www.primoproject.net`.

Chapter 6

Conclusions

The research presented in this thesis improved the knowledge on the absorbed–dose to water distributions produced by ^{106}Ru/^{106}Rh ophthalmic plaques. The conclusions are related to the objectives stated in chapter 1 and they are presented in the corresponding order:

1. The Monte Carlo code for radiation transport PENELOPE was used to simulate twelve ^{106}Ru/^{106}Rh plaque models. Absorbed dose distributions in water were obtained. A good agreement was found (generally within 3%) with published measurement data and with measurements performed in this work with the EBT3 radiochromic film. Comparison with the literature allowed to find causes of deficiencies in previous publications. The data set from the Monte Carlo simulations obtained may well constitute the basis for the first consensus dataset for these plaques.

2. A simulation study with PENELOPE was carried out on the influence of the phantom material on the absorbed–dose energy dependence of the EBT3 radiochromic film. Solid phantom materials commonly used in film dosimetry were analyzed and compared to water, the reference material. The results confirmed an improvement in the absorbed-dose energy dependence of the EBT3 film respect to older models when irradiated in water. The maximum difference of the EBT3 energy dependence with the solid phantoms studied respect to water is about 6%, found at an energy of 50 keV. Moreover, the reported overall energy dependence of the EBT3 film in water at energies below 100 keV was found to be due to the intrinsic energy dependence.

3. A practical experimental method was developed for measuring in water the 2D absorbed dose distributions and the absolute dose rates produced by ^{106}Ru/^{106}Rh plaques, using the EBT3 radiochromic film. Experimental results for dose planes containing the symmetry axis of the plaques, and dose planes perpendicular to it were obtained for the CCA and CCX plaque models. The measured absolute dose rates agreed with the values quoted in the calibration certificates of the plaques within the experimental uncertainty, with typical differences below 5%. The relative standard uncertainties obtained were of 3.8% for dose distributions measured at planes perpendicular to the symmetry axis, and of 7.4% for planes containing the symmetry axis (depth–dose planes). These values are comparable to those reported by other authors using plastic phantoms, but avoiding uncertainties associated to the conversion from dose–to–plastic to dose–to–water.

Chapter 7

Abstract

Eye cancer is an uncommon disease. Despite its low incidence, ocular tumors such as uveal melanoma and retinoblastoma can be life–threatening in many cases. For small–to–medium ocular tumors, brachytherapy with radioactive ^{106}Ru/^{106}Rh plaques offers good outcomes in terms of local control and disease–free survival. Although these plaques have been used for decades, the measurement and calculation of the produced dose distributions remain challenging tasks. This thesis aims at improving the current knowledge on the theoretical and experimental dosimetry of ^{106}Ru/^{106}Rh plaques.

First, we used Monte Carlo simulation of radiation transport to estimate accurate absorbed dose to water distributions produced by twelve plaque models. Secondly, we developed a practical experimental technique to measure in water the planar dose distributions produced by the plaques. For this experimental validation the EBT3 radiochromic film model was used which, in turn, required to characterize the absorbed–dose energy dependence of this new film model by means of Monte Carlo simulation. A detailed uncertainty analysis was carried out for simulation and experimental results. Both the simulated and measured absorbed dose distributions were compared with the available literature.

The simulated dose distributions agreed within 3% with published data and with the EBT3 measurement results. Some discrepancies from the literature were also solved. This is the first, and currently unique, comprehensive dosimetry dataset for ^{106}Ru/^{106}Rh plaques. Therefore, it can become the basis for the first consensus dataset available. This dataset could also be useful for quality assurance of treatment planning systems.

The simulation of the EBT3 film confirmed an improvement in the absorbed-dose energy dependence for this film model respect to older models. Applications for this film are found in many areas of medical physics.

The measured dose distributions achieved a good agreement in absolute dosimetry with measurements by the manufacturer, and in relative dosimetry with the simulation results. The proposed method would allow users to check absolute dose distributions close to the plaque surface, and directly in water, thus avoiding the conversion from dose–to–plastic to dose–to–water, as it would occur if solid phantoms were used. With this method, a smaller experimental uncertainty was attained respect to the manufacturer and other authors.

Bibliography

Abouzeid, H., Moeckli, R., Gaillard, M.-C., Beck-Popovic, M., Pica, A., Zografos, L., Balmer, A., Pampallona, S., and Munier, F. L. (2008): (106)Ruthenium brachytherapy for retinoblastoma. Int. J. Radiat. Oncol., Biol., Phys. 71, 821–828.

Almansa, J., Salvat-Pujol, F., Díaz-Londoño, G., Carnicer, A., Lallena, A. M., and Salvat, F. (2016): PENGEOM–A general-purpose geometry package for Monte Carlo simulation of radiation transport in material systems defined by quadric surfaces. Comput. Phys. Commun. 199, 102–113.

Astrahan, M. A. (2003): A patch source model for treatment planning of ruthenium ophthalmic applicators. Med. Phys. 30, 1219–1228.

Astrahan, M. A., Luxton, G., Jozsef, G., Kampp, T. D., Liggett, P. E., Sapozink, M. D., and Petrovich, Z. (1990): An interactive treatment planning system for ophthalmic plaque radiotherapy. Int. J. Radiat. Oncol., Biol., Phys. 18, 679–687.

Badano, A. and Sempau, J. (2006): MANTIS: combined x-ray, electron and optical Monte Carlo simulations of indirect radiation imaging systems. Phys. Med. Biol. 51, 1545–1561.

Barbosa, N., da Rosa, L., and Braz, D. (2015): Development of a phantom for ophthalmic beta source applicator quality control using TL dosimetry. Radiat. Phys. Chem. 116, 287–291.

Barbosa, N. A., da Rosa, L. A. R., Menezes, A. F. D., Reis, J., Facure, A., Braz, D., Antonio, L., Passos, J., and Júnior, R. (2014): Assessment of ocular beta radiation dose distribution due to ^{106}Ru/^{106}Rh brachytherapy applicators using MCNPX Monte Carlo code. Int. J. Cancer Ther. Oncol. 2, 1–11.

Baró, J., Sempau, J., Fernández-Varea, J., and Salvat, F. (1995): PENELOPE: An algorithm for Monte Carlo simulation of the penetration and energy loss of electrons and positrons in matter. Nucl. Instrum. Meth. B 100, 31–46.

Bekerat, H., Devic, S., Deblois, F., Singh, K., Sarfehnia, A., Seuntjens, J., Shih, S., Yu, X., and Lewis, D. (2014): Improving the energy response of external beam therapy (EBT) GafChromic™ dosimetry films at low energies ($\leq$ 100 keV). Med. Phys. 41, 022101–1–14.

Berger, J. M. (1963): Monte Carlo calculation of the penetration and diffusion of fast charged particles. In: Alder, B., Fernbach, S., and Rotenberg, M., eds., Methods in Computational Physics, Vol. 1, 135–215. New York, USA: Academic Press.

Blackwell, C. R., Coursey, B. M., Gall, K. P., Galvin, J. M., Mclaughlin, W. L., Meigooni, A. S., and Soares, C. G. (1998): Radiochromic Film Dosimetry. Med. Phys. 25, 2093–2115.

Brualla, L., Sempau, J., and Sauerwein, W. (2012): Comment on Monte Carlo calculation of the dose distributions of two ^{106}Ru eye applicators [Radiother Oncol 49 (1998) 191-196]. Radiother. Oncol. 104, 267–268.

Brualla, L., Sempau, J., Zaragoza, F. J., Wittig, A., and Sauerwein, W. (2013): Accurate estimation of dose distributions inside an eye irradiated with ^{106}Ru plaques. Strahlenther. Onkol. 189, 68–73.

Brualla, L., Zaragoza, F. J., Eichmann, M., Flühs, D., and Sauerwein, W. (2016): Absorbed dose distributions from inhomogeneous Ru-106 eye plaques using Monte Carlo simulation. Strahlenther. Onkol. 192, 47.

Brualla, L., Zaragoza, F. J., and Sauerwein, W. (2014): Monte Carlo Simulation of the Treatment of Eye Tumors with ^{106}Ru Plaques: A Study on Maximum Tumor Height and Eccentric Placement. Ocul. Oncol. Pathol. 1, 1–11.

Bureau International des Poids et Mesures (2008): Evaluation of measurement data: Guide to the expression of uncertainty in measurement. Technical report.

Butson, M. J., Cheung, T., and Yu, P. K. N. (2006): Weak energy dependence of EBT Gafchromic film dose response in the 50 kVp–10 MVp x-ray range. Appl. Radiat. Isot. 64, 60–62.

Butson, M. J., Yu, P. K., Cheung, T., and Alnawaf, H. (2010): Energy response of the new EBT2 radiochromic film to x–ray radiation. Radiat. Meas. 45, 836–839.

Cano-Herranz, A., Delgado-Soler, C., Anducas-Santiago, N., and Hermida-López, M. (2014): EP-1544: Dose distributions for CCX, CCA and CIA applicators: Plaque Simulator vs. PENELOPE Monte Carlo code. Radiother. Oncol. 111, S181.

Chan, M. F., Fung, A. Y., Hu, Y. C., Chui, C. S., Amols, H., Zaider, M., and Abramson, D. (2001): The measurement of three dimensional dose distribution of a ruthenium-106 ophthalmological applicator using magnetic resonance imaging of BANG polymer gels. J. Appl. Clin. Med. Phys. 2, 85–89.

Chiu-Tsao, S.-T., Ho, Y., Shankar, R., Wang, L., and Harrison, L. B. (2005): Energy dependence of response of new high sensitivity radiochromic films for megavoltage and kilovoltage radiation energies. Med. Phys. 32, 3350–3354.

Cross, W. G., Hokkanen, J., Järvinen, H., Mourtada, F., Sipilä, P., Soares, C. G., and Vynckier, S. (2001): Calculation of beta-ray dose distributions from ophthalmic applicators and comparison with measurements in a model eye. Med. Phys. 28, 1385–1396.

Crum, W. R., Hartkens, T., and Hill, D. L. G. (2004): Non–rigid image registration: theory and practice. Br. J. Radiol. 77, S140–S153.

Damato, B., Patel, I., Campbell, I. R., Mayles, H. M., and Errington, R. D. (2005): Local tumor control after ^{106}Ru brachytherapy of choroidal melanoma. Int. J. Radiat. Oncol., Biol., Phys. 63, 385–391.

Damato, B. E. (2012): Treatment selection for uveal melanoma. In: Jager M.J., Desjardins L., Kivelä T., Damato B., ed., Current concepts in uveal melanoma, volume 49, 16–26. Karger Publishers.

Davelaar, J., Schaling, D., Hennen, L., and Broerse, J. (1992): Dosimetry of ruthenium-106 eye applicators. Med. Phys. 19, 691–694.

Defrenne, D. and Negret, A. (2008): Nuclear Data Sheets for A = 106. Nucl. Data Sheets 109, 943–1102.

Devic, S. (2011): Radiochromic film dosimetry: past, present, and future. Phys. Med. 27, 122–34.

Devic, S., Tomic, N., and Lewis, D. (2016): Reference radiochromic film dosimetry: Review of technical aspects. Phys. Med. In press.

Eichmann, M., Fluhs, D., and Spaan, B. (2009): Development of a high precision dosimetry system for the measurement of surface dose rate distribution for eye applicators. Med. Phys. 36, 4634–4643.

Erazo, F., Brualla, L., and Lallena, A. M. (2014): Electron beam quality k_{Q,Q_0} factors for various ionization chambers: a Monte Carlo investigation with PENELOPE. Phys. Med. Biol. 59, 6673–6691.

España, S., Herraiz, J. L., Vicente, E., Vaquero, J. J., Desco, M., and Udias, J. M. (2009): PeneloPET, a Monte Carlo PET simulation tool based on PENELOPE: features and validation. Phys. Med. Biol. 54, 1723–1742.

Faddegon, B. A., Asai, M., Perl, J., Ross, C., Sempau, J., Tinslay, J., and Salvat, F. (2008): Benchmarking of Monte Carlo simulation of bremsstrahlung from thick targets at radiotherapy energies. Med. Phys. 35, 4308–4317.

Faddegon, B. A., Kawrakow, I., Kubyshin, Y., Perl, J., Sempau, J., and Urban, L. (2009): The accuracy of EGSnrc, Geant4 and PENELOPE Monte Carlo systems for the simulation of electron scatter in external beam radiotherapy. Phys. Med. Biol. 54, 6151–6163.

Fernández-Varea, J., Mayol, R., Baró, J., and Salvat, F. (1993): On the theory and simulation of multiple elastic scattering of electrons. Nucl. Instrum. Meth. B 73, 447–473.

Flühs, D., Flühs, A., Ebenau, M., and Eichmann, M. (2016): Polyethylene Naphthalate Scintillator: A Novel Detector for the Dosimetry of Radioactive Ophthalmic Applicators. Ocul. Oncol. Pathol. 2, 5–12.

Forster, R., Cox, L. J., Barrett, R. F., Booth, T. E., Briesmeister, J. F., Brown, F. B., Bull, J. S., Geisler, G. C., Goorley, J. T., Mosteller, R. D., Post, S. E., Prael, R. E., Selcow, E. C., and Sood, A. (2004): MCNP™ Version 5. Nucl. Instrum. Meth. B 213, 82–86.

Fuss, M. C., Muñoz, A., Oller, J. C., Blanco, F., Williart, A., Limão-Vieira, P., Borge, M. J. G., Tengblad, O., Huerga, C., Téllez, M., and García, G. (2011): Energy deposition by a ^{106}Ru/^{106}Rh eye applicator simulated using LEPTS, a low–energy particle track simulation. Appl. Radiat. Isot. 69, 1198–1204.

Galloway, N. R., Amoaku, W. M. K., Galloway, P. H., and Browning, A. C. (2006): Basic Anatomy and Physiology of the Eye. In: Common eye diseases and their management; S. 7–15. London: Springer.

García-Toraño, E. and Grau-Malonda, A. (1985): EFFY, a new program to compute the counting efficiency of beta particles in liquid scintillators. Comput. Phys. Commun. 36, 307–312.

Graves, Y. J., Jia, X., and Jiang, S. B. (2013): Effect of statistical fluctuation in Monte Carlo based photon beam dose calculation on gamma index evaluation. Phys. Med. Biol. 58, 1839–1853.

Halbleib, J. A., Kensek, R. P., Valdez, G. D., Seltzer, S. M., and Berger, M. J. (1992): ITS: the integrated TIGER series of electron/photon transport codes-Version 3.0. IEEE T. Nucl. Sci. 39, 1025–1030.

Heilemann, G., Nesvacil, N., Blaickner, M., Kostiukhina, N., and Georg, D. (2015): Multidimensional dosimetry of ^{106}Ru eye plaques using EBT3 films and its impact on treatment planning. Med. Phys. 42, 5798–5808.

Hermida-López, M. (2013): Calculation of dose distributions for 12 ^{106}Ru/^{106}Rh ophthalmic applicator models with the PENELOPE Monte Carlo code. Med. Phys. 40, 101705–1–13.

Hermida-López, M. (2016): Erratum: "Calculation of dose distributions for 12 ^{106}Ru/^{106}Rh ophthalmic applicator models with the PENELOPE Monte Carlo code" [Med. Phys. 40, 101705 (13pp.) (2013)]. Med. Phys. 43, 1020.

Hermida-López, M., Lüdemann, L., Flühs, A., and Brualla, L. (2014): Technical Note: Influence of the phantom material on the absorbed–dose energy dependence of the EBT3 radiochromic film for photons in the energy range 3 keV–18 MeV. Med. Phys. 41, 112103–1–6.

Hill, R., Brown, S., and Baldock, C. (2008): Evaluation of the water equivalence of solid phantoms using gamma ray transmission measurements. Radiat. Meas. 43, 1258–1264.

Hokkanen, J., Heikkonen, J., and Holmberg, P. (1997): Theoretical calculations of dose distributions for beta–ray eye applicators. Med. Phys. 24, 211–213.

Hubbell, J. H. and Seltzer, S. M. (1996): Tables of X-Ray Mass Attenuation Coefficients and Mass Energy-Absorption Coefficients from 1 keV to 20 MeV for Elements Z = 1 to 92 and 48 Additional Substances of Dosimetric Interest (version 1.4). [Online] Available: `http://physics.nist.gov/xaamdi` [2016, Jun. 26]. NIST.

IAEA (2001): Absorbed dose determination in external beam radiotherapy: an international code of practice for dosimetry based on standards of absorbed dose to water. IAEA Technical Report Series 398. Vienna: IAEA.

ICRU (1989): Tissue Substitutes in Radiation Dosimetry and Measurement (ICRU Report 44). Washington, D.C.: ICRU.

ICRU (1997): Dosimetry of External Beta Rays for Radiation Protection (ICRU Report 56). Washington, D.C.: ICRU.

ICRU (2004): Dosimetry of Beta Rays and Low-Energy Photons for Brachytherapy With Sealed Sources. J. ICRU 4, 2–2.

Kalos, M. H. and Whitlock, P. A. (2008): Monte Carlo Methods. 2. Ed. Weinheim: Wiley.

Kaulich, T. W., Zurheide, J., Haug, T., Budach, W., Nüsslin, F., and Bamberg, M. (2004): On the actual state of industrial quality assurance procedures with regard to (106)Ru ophthalmic plaques. Strahlenther. Onkol. 180, 358–364.

Kaulich, T. W., Zurheide, J., Haug, T., Nüsslin, F., and Bamberg, M. (2005): Clinical quality assurance for ^{106}Ru ophthalmic applicators. Radiother. Oncol. 76, 86–92.

Kawrakow, I., Mainegra-Hing, E., Tessier, F., and Walters, B. (2009): The EGSnrc C++ class library. Technical Report No. PIRS–898 (rev A). Technical report, National Research Council of Canada, Ottawa, Canada.

Kirov, A. S., Piao, J. Z., Mathur, N. K., Miller, T. R., Devic, S., Trichter, S., Zaider, M., Soares, C. G., and LoSasso, T. (2005): The three–dimensional scintillation dosimetry method: test for a ^{106}Ru eye plaque applicator. Phys. Med. Biol. 50, 3063–3081.

Kovačević, N., Vrtar, M., and Vekić, B. (2005): A simple calibration method for ^{106}Ru/^{106}Rh eye applicators. Radiother. Oncol. 74, 293–299.

Lommatzsch, P. K., Werschnik, C., and Schuster, E. (2000): Long–term follow–up of ^{106}Ru/^{106}Rh brachytherapy for posterior uveal melanoma. Graef. Arch. Clin. Exp. 238, 129–137.

Low, D. A., Harms, W. B., Mutic, S., and Purdy, J. A. (1998): A technique for the quantitative evaluation of dose distributions. Med. Phys. 25, 656–661.

Micke, A., Lewis, D. F., and Yu, X. (2011): Multichannel film dosimetry with nonuniformity correction. Med. Phys. 38, 2523–2534.

Miras, H., Terrón, J. A., and Lallena, A. M. (2013): Monte Carlo simulation of COMS ophthalmic applicators loaded with Bebig I25.S16 seeds and comparison with planning system predictions. Phys. Med. 29, 670–676.

Mourtada, F. (2005): ^{106}Ru/^{106}Rh Plaque and proton radiotherapy for ocular melanoma: a comparative dosimetric study. Radiat. Prot. Dosim. 116, 454–460.

Nag, S., Quivey, J. M., Earle, J. D., Followill, D., Fontanesi, J., and Finger, P. T. (2003): The American Brachytherapy Society recommendations for brachytherapy of uveal melanomas. Int. J. Radiat. Oncol., Biol., Phys. 56, 544–555.

Nath, R., Rivard, M. J., DeWerd, L. A., Dezarn, W. A., Thompson Heaton, H., Ibbott, G. S., Meigooni, A. S., Ouhib, Z., Rusch, T. W., Siebert, F.-A., and Venselaar, J. L. M. (2016): Guidelines by the AAPM and GEC–ESTRO on the use of innovative brachytherapy devices and applications: Report of Task Group 167. Med. Phys. 43, 3178–3205.

Nathan, P., Cohen, V., Coupland, S., Curtis, K., Damato, B., Evans, J., Fenwick, S., Kirkpatrick, L., Li, O., Marshall, E., McGuirk, K., Ottensmeier, C., Pearce, N., Salvi, S., Stedman, B., Szlosarek, P., and Turnbull, N. (2015): Uveal Melanoma UK National Guidelines. Eur. J. Cancer 51, 2404–2412.

Olch, A. J. (2013): Pediatric Radiotherapy. Planning and Treatment. 1. Ed. Boca Raton, London, New York: CRC Press.

Poludniowski, G., Landry, G., DeBlois, F., Evans, P. M., and Verhaegen, F. (2009): SpekCalc : a program to calculate photon spectra from tungsten anode x-ray tubes. Phys. Med. Biol. 54, N433–N438.

Rink, A., Vitkin, I. A., and Jaffray, D. A. (2007): Energy dependence (75 kVp to 18 MV) of radiochromic films assessed using a real–time optical dosimeter. Med. Phys. 34, 458–463.

Rodríguez, M., Sempau, J., and Brualla, L. (2013): PRIMO: A graphical environment for the Monte Carlo simulation of Varian and Elekta linacs. Strahlenther. Onkol. 189, 881–886.

Rodríguez Castillo, M. L. (2015): Automation of the Monte Carlo simulation of medical linear accelerators. Ph.D. thesis, Universidad Politécnica de Cataluña.

Rogers, D. W. O. (2009): General characteristics of radiation dosimeters and a terminology to describe them. In: Rogers, D. and Cygler, J., eds., Clin. Dosim. Meas. Radiother., chapter 4, 137–146. Madison WI: Medical Physics Publishing.

Salvat, F. (2015a): PENELOPE–2014: A code system for Monte Carlo simulation of electron and photon transport. OECD/NEA Data Bank, Issy-les-Moulineaux, France.

Salvat, F. (2015b): The PENELOPE code system. Specific features and recent improvements. Ann. Nucl. Energy 82, 98–109.

Salvat, F., Fernández-Varea, J., and Sempau, J. (2009): PENELOPE–2008: A code system for Monte Carlo simulation of electron and photon transport. OECD/NEA Data Bank, Issy-les-Moulineaux, France.

Salvat, F., Fernández-Varea, J., and Sempau, J. (2011): PENELOPE 2011: A code system for Monte Carlo simulation of electron and photon transport. OECD/NEA Data Bank, Issy-les-Moulineaux, France.

Sánchez-Reyes, A., Tello, J. I., Guix, B., Salvat, F., and Tello, J. J. (1998): Monte Carlo calculation of the dose distributions of two ^{106}Ru eye applicators. Radiother. Oncol. 49, 191–196.

Scherman, J. B. (2009): Development and evaluation of methods for comparison of dose distributions in radiotherapy using calculated, synthetic and simulated measured dose distributions. Ph.D. thesis, Lund University.

Schueler, A. O., Flühs, D., Anastassiou, G., Jurklies, C., Neuhäuser, M., Schilling, H., Bornfeld, N., and Sauerwein, W. (2006): Beta-ray brachytherapy with ^{106}Ru plaques for retinoblastoma. Int. J. Radiat. Oncol., Biol., Phys. 65, 1212–1221.

Sempau, J., Acosta, E., Baro, J., Fernández-Varea, J., and Salvat, F. (1997): An algorithm for Monte Carlo simulation of coupled electron–photon transport. Nucl. Instrum. Meth. B 132, 377–390.

Sempau, J. and Andreo, P. (2006): Configuration of the electron transport algorithm of PENELOPE to simulate ion chambers. Phys. Med. Biol. 51, 3533–3548.

Sempau, J., Badal, A., and Brualla, L. (2011): A PENELOPE–based system for the automated Monte Carlo simulation of clinacs and voxelized geometries—application to far–from–axis fields. Med. Phys. 38, 5887–5895.

Sempau, J., Fernández-Varea, J., Acosta, E., and Salvat, F. (2003): Experimental benchmarks of the Monte Carlo code PENELOPE. Nucl. Instrum. Meth. B 207, 107–123.

Sipilä, P., Ojala, J., Kaijaluoto, S., Jokelainen, I., and Kosunen, A. (2016): Gafchromic EBT3 film dosimetry in electron beams — energy dependence and improved film read–out. J. Appl. Clin. Med. Phys. 17, 360–373.

Soares, C. G., Vynckier, S., Järvinen, H., Cross, W. G., Sipilä, P., Flühs, D., Schaeken, B., Mourtada, F. A., Bass, G. A., and Williams, T. T. (2001): Dosimetry of beta-ray ophthalmic applicators: Comparison of different measurement methods. Med. Phys. 28, 1373–1384.

Sorriaux, J., Kacperek, A., Rossomme, S., Lee, J. A., Bertrand, D., Vynckier, S., and Sterpin, E. (2013): Evaluation of Gafchromic EBT3 films characteristics in therapy photon, electron and proton beams. Phys. Med. 29, 599–606.

Sutherland, J. G. H. and Rogers, D. W. O. (2010): Monte Carlo calculated absorbed–dose energy dependence of EBT and EBT2 film. Med. Phys. 37, 1110–1116.

Taccini, G., Cavagnetto, F., Coscia, G., Garelli, S., and Pilot, A. (1997): The determination of dose characteristics of ruthenium ophthalmic applicators using radiochromic film. Med. Phys. 24, 2034–2037.

Takiar, V., Gombos, D. S., Mourtada, F., Rechner, L. A., Lawyer, A. A., Morrison, W. H., Garden, A. S., and Beadle, B. M. (2014): Disease control and toxicity outcomes using ruthenium eye plaque brachytherapy in the treatment of uveal melanoma. Pract. Radiat. Oncol. 4, e189–e194.

Takiar, V., Voong, K. R., Gombos, D. S., Mourtada, F., Rechner, L. A., Lawyer, A. A., Morrison, W. H., Garden, A. S., and Beadle, B. M. (2015): A choice of radionuclide: Comparative outcomes and toxicity of ruthenium-106 and iodine-125 in the definitive treatment of uveal melanoma. Pract. Radiat. Oncol. 5, e169–e176.

The American Brachytherapy Society – Ophthalmic Oncology Task Force (2014): The American Brachytherapy Society consensus guidelines for plaque brachytherapy of uveal melanoma and retinoblastoma. Brachytherapy 13, 1–14.

The Collaborative Ocular Melanoma Study Group (2006): The COMS Randomized Trial of Iodine 125 Brachytherapy for Choroidal Melanoma. V. Twelve-Year Mortality Rates and Prognostic Factors: COMS Report No. 28. Arch. Ophthalmol. 124, 1693.

Verschueren, K. M. S., Creutzberg, C. L., Schalij-Delfos, N. E., Ketelaars, M., Klijsen, F. L. L., Haeseker, B. I., Ligtenberg, S. M. B., Keunen, J. E. E., and Marijnen, C. A. M. (2010): Long–term outcomes of eye–conserving treatment with Ruthenium(106) brachytherapy for choroidal melanoma. Radiother. Oncol. 95, 332–338.

Villarreal-Barajas, J. E. and Khan, R. F. H. (2014): Energy response of EBT3 radiochromic films: implications for dosimetry in kilovoltage range. J. Appl. Clin. Med. Phys. 15, 331–338.

Wendling, M., Zijp, L. J., McDermott, L. N., Smit, E. J., Sonke, J.-J., Mijnheer, B. J., and van Herk, M. (2007): A fast algorithm for gamma evaluation in 3D. Med. Phys. 34, 1647–1654.

Acknowledgements

First of all, I would like to express my gratitude to my supervisor, Priv.-Doz. Dr. Lorenzo Brualla, for his expertise, support, and infinite patience, which were essential for the success of this work. *¡Gracias, Lorenzo!* I am also deeply grateful to Prof. Dr. med. Wolfgang Sauerwein, leitender Oberarzt of the Strahlenklinik at the Universitätsklinikum Essen, for giving me this opportunity and for his support at all levels. I want to thank also the following people:

Dipl.-Phys. Andrea Flühs, Dr. Dirk Flühs, and Priv.-Doz. Dr. Lutz Lüdemann (Strahlenklinik, Universitätsklinikum Essen), for their support during my research.
Dr. Josep Sempau, from the Universitat Politécnica de Catalunya (Barcelona) for his support and advices on Monte Carlo simulation.
Dr. Miguel Rodríguez, for many interesting discussions on the intricacies of Monte Carlo simulation of radiation transport.
Mr. Josep Pujal and Mr. Michael Nieporte, system administrators of the Argos cluster at the Universitat Politécnica de Catalunya, and of the Contessa cluster at Universitätsklinikum Essen, respectively.
Ms. Ina Grübel and Ms. Gundula Franz, documentalist and administrative staff of the Strahlenklinik at the Universitätsklinikum Essen.
The staff of the Servei d'Oncologia Radioteràpica, and of the Servei de Física i Protecció Radiológica of Hospital Universitari Vall d'Hebron (Barcelona), where I work as medical physicist, and where the measurements presented in this thesis were performed.
Dr. Nora L. Maidana and Prof. Dr. Vito R. Vanin (Instituto de Física, Universidade de São Paulo), for my participation in their research project on HPGe detectors.
Mr. Francisco de los Reyes (Fimecorp S.L.), for the temporary licence of FilmQA software.
Dr. Jonas Scherman (Department of Oncology, Rigshospitalet, Copenhagen) for allowing me to use his Matlab code to calculate the gamma index.
Priv.-Doz. Dr. Theodor W. Kaulich (Tübingen Universitätsklinik für Radioonkologie), for bringing a misprint to my attention (Hermida-López, 2016).
Mr. Johann Kindlein and Ms. Alena Kindlein (MedInEx GmbH, Adendorf), for inviting me to participate as a speaker at the Gafchromic Workshop (Universitätsklinikum Essen, May 2014).
Mr. Juan Francisco Calvo Ortega, medical physicist and friend from the Department of Radiotherapy of Hospital Quirón Barcelona, for his constant support during the thesis journey, and for all the discussions on medical physics and other topics.
My friends and my family.

I am also grateful to the following institutions for supporting my research: Spanish Ministerio de Economía y Competitividad (Project No. FIS2012-38480), Deutsche Forschungsgemeinschaft Project No. BR 4043/3-1, and the IFORES Programm of the Medizinische Fakultät at the Universität Duisburg-Essen.

The CV is not included in the online version for reasons of data protection.